Alma Mater Studiorum – Università di Bologna

DOTTORATO DI RICERCA IN FISICA

Ciclo XXXII

Settore Concorsuale: 02/A2

Settore Scientifico Disciplinare: FIS/02

Quantum simulation and topological phases in Lattice Gauge Theories

Presentata da: Giuseppe Magnifico

Coordinatore Dottorato:
Prof.ssa Silvia Arcelli

Supervisore:
Prof.ssa Elisa Ercolessi

Esame finale anno 2020

Abstract

Simulating quantum mechanical systems is still today a very challenging issue due to the high computational costs. The main reason for this is related to the dimension of the Hilbert space that grows exponentially with the number of degrees of freedom, making an exact implementation impossible even for the most powerful today's supercomputers.
In order to circumvent these difficulties classical approximation methods have been developed over the last fifty years. These methods, however, do not always provide acceptable accuracy for strongly correlated fermionic models in condensed matter physics, and for fermionic quantum field theories in finite-density regimes, especially when the number of degrees of freedom becomes very large.
On this ground it appears clear the need of a new simulation method, i.e. *quantum simulation*. The general idea is very simple: using a controllable quantum system, called *quantum simulator*, to emulate and to analyze another quantum system that usually results less controllable or accessible. Quantum simulation is currently a growing and multidisciplinary physical area that involves theoretical and experimental research. From the theoretical side, the main focus is on the study of simulation-models that create a mapping between the target physics and the simulator.
In the first and in the second part of this thesis, we explore these ideas by studying the ground-state properties and the real-time dynamics of a class of Z_n lattice gauge theories in 1+1 dimensions, in which the gauge fields are coupled to spinless fermionic matter. These models can be considered as quantum simulation-models of lattice 1+1 Quantum Electrodynamics (QED), known in literature as the *Schwinger model*, which is possibly the simplest gauge theory that shows non-trivial phenomena, like confinement, that are also observed in more complicated gauge theories, such as 3+1 Quantum Chromodynamics (QCD).
In the third part of this thesis, we unveil an interesting interplay of symmetry and topology by demonstrating the existence of *symmetry-protected topological* (SPT) phases in the presence of gauge interactions and initiating a systematic study into a wider class of such systems. More specifically, we introduce an alternative discretization of the continuum Schwinger model leading to the *topological Schwinger model*. We use bosonization and Density-Matrix Renormalization Group (DMRG) techniques to analyze the rich phase diagram of the model in great detail, opening an interesting route to study topological phases of matter in the context of gauge theories.

Contents

Introduction

An excellent starting point to approach the concept of *quantum simulation* is represented by these memorable words: *"Nature isn't classical, dammit, and if you want to make a simulation of nature, you'd better make it quantum mechanical, and by golly it's a wonderful problem, because it doesn't look so easy"* (R. P. Feynman, 1982).

More than thirty years later, simulating quantum mechanical systems is still a very challenging issue. The main reason for this is the following: let us consider a generic quantum system with N degrees of freedom (e.g. the number of particles in the system or the system size) and with a Hamiltonian H. It follows from the postulates of quantum mechanics that the dimension of the Hilbert space of the system grows exponentially with the number of degrees of freedom, i.e. $dim\mathcal{H} \propto a^N$. So, in order to perform a numerical analysis of the system on a computer, we must store in memory a vector of length a^N for the quantum state of the system and an $a^N \times a^N$-matrix for each observable. To have a concrete idea of the problem, just think that to store in a memory a single state of a spin-1/2 chain of length $N = 40$, about 4 terabytes are required. This results completely inefficient from a computational point of view and imposes significant limitations even for today's most powerful supercomputers in calculating the static properties or the real-time evolution of realistic systems with many degrees of freedom.

In order to circumvent these difficulties classical stochastic approximation methods, e.g. *Monte Carlo*, have been developed over the last fifty years: these algorithms evaluate the phase space of the system and the integrals defined on it (for instance, mean values of the observables, correlators, partition functions) in a polynomial time with respect to the number of components of the system. However, these methods provide remarkable accuracy only when the functions within integrals vary slowly and do not change sign. In general, this does not occur in many quantum systems, especially for

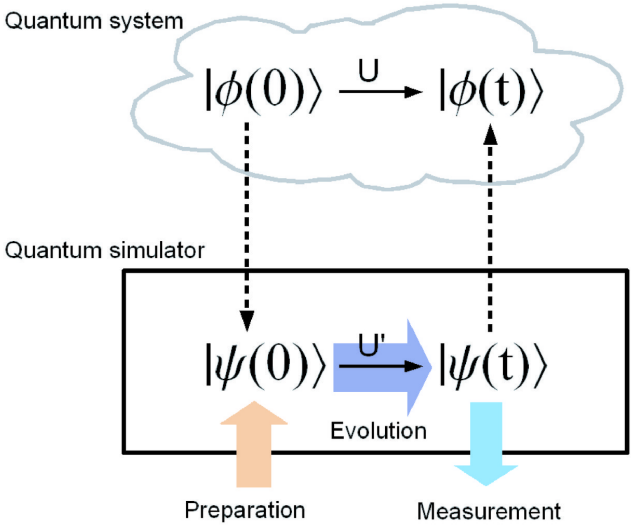

Figure 1: The quantum simulation scheme as explained in [3]: correspondence between the quantum states of the simulator and the simulated system.

strongly correlated fermionic systems in condensed matter physics, e.g. Hubbard model, and for fermionic quantum field theories in finite-density regimes such as quantum chromodynamics. Thus, in this sense, classical simulations are severely limited by this problem, which is known in literature as the *sign problem* [1].

On this ground it appears clear the need of a new simulation method, i.e. *quantum simulation*. As proposed by Feynman [2], the general idea is very simple: using a controllable quantum system, called *quantum simulator*, to emulate and to analyze another quantum system that usually results less controllable or accessible. In this framework, a controllable system is such that the initial state $|\psi(0)\rangle$ can be prepared, the unitary evolution $U' = e^{-iH_{qs}t/\hbar}$, through a suitable Hamiltonian of the simulator H_{qs}, can be engineered, and the final state $|\psi(t)\rangle$ can be measured, as shown in Fig. 1 from [3].

Let us denote with H_s the Hamiltonian of the original quantum system that we want to analyze, with $U = e^{-iH_s t/\hbar}$ its unitary evolution and with $|\phi(0)\rangle$ and $|\phi(t)\rangle$ the states at different times. It is clear that the quantum simulator has to take into account a mapping of the initial system, i.e. $|\phi(0)\rangle \leftrightarrow |\psi(0)\rangle$, $|\phi(t)\rangle \leftrightarrow |\psi(t)\rangle$, $H_s \leftrightarrow H_{qs}$, $U \leftrightarrow U'$, so that a measurement on the simulator provides information about the properties of the simulated system. Compared to classic simulation, the key element here is that the simulator, being intrinsically quantum, has the capacity to contain

an exponentially large amount of information without using an exponentially large amount of physical resources, thus making it a natural tool to perform the simulation of a quantum system even with a large number of degrees of freedom.

Quantum simulation is currently a growing and multidisciplinary physical area that involves theoretical and experimental research. From the theoretical side, the main focus is on the study of simulation-models that create a mapping between the target physics and the simulator: it is very important to analyze these models numerically in order to check their capabilities in reproducing the features of the target system. On the other side, the experimental research focuses on engineering quantum systems with accurate interaction and control at the single quantum level. These systems, which are exploitable as quantum simulators in table-top experiments, usually consist of ultracold atoms in optical lattices [4], trapped ions [5], superconducting circuits [6] or photonic setups [7].

The aim of such quantum simulation models and platforms is to shed light on difficult quantum many-body problems, especially those so complex that they cannot be solved even on most powerful classical supercomputers. In particular, there is the intriguing possibility to explore lattice gauge theories (LGTs) [8, 9], i.e. quantum field theories with local symmetries on a space-time discretized into a lattice. LGTs represent a fundamental tool for the numerical study of gauge models, such as quantum electrodynamics (QED) and quantum chromodynamics (QCD), which are in the core of contemporary particle physics. Thus, the study of such lattice theories is of paramount importance for understanding non-perturbative phenomena of the Standard Model, such as the confinement of quarks or the hadron spectrum, and represents a complex and historical problem, that was investigated by a number of outstanding physicists over the last fifty years. In 1974 Wilson proposed a method to regularize a quantum field theory with gauge symmetries on a discrete lattice [10]. In this formulation the lattice is composed by sites separated by distance a and connected by links: fermion fields are defined at lattice sites while the gauge fields are defined on the links. In 1975 Kogut and Susskind obtained a Hamiltonian formulation of these LGTs preserving the local gauge-invariance on the lattice [11]. These approaches make possible the numerical calculation of many important quantities and phenomena of gauge theories, mainly using *Monte Carlo* classical simulation methods. Such calculations are often extremely computationally intensive, and can require the use of the largest supercomputers especially for extrapolating the continuum limit of the theory. Several and significant results have been obtained from these studies, such as the low-energy spectrum of QCD, some properties of the quark-gluon plasma and the deconfinement phase transition at

finite temperature [12]. Nevertheless, due to the aforementioned sign problem, these classical simulations are severely limited in the regime of finite chemical potential or in calculating the real-time dynamics of the particles and field.

Thus, the possibility of using quantum simulators to tackle these problems has become extremely attractive and has been made possible by recent developments in low-temperature physics and atomic control techniques in optical lattices [14–17]. Many proposals have been put forward in the literature to use ultra-cold atomic optical lattice systems to simulate Abelian and non-Abelian lattice gauge theories [18–26] and in particular quantum electrodynamics in 1+1 dimensions (known in literature as the *Schwinger model*), that appears as a realizable option in the not-too-distant future [27–30]. This model is possibly the simplest gauge theory, based on the Abelian gauge group $U(1)$, that incorporates quantum matter and quantum gauge fields and its lattice formulation shows non-trivial phenomena, like confinement, that are also observed in more complicated gauge theories, such as 3+1 QCD. The peculiarity of 1+1 QED comes from the fact that in one spatial dimension the Coulomb potential between opposite charges increases linearly with their distance and thus prevents them from becoming free. Therefore the Schwinger model is considered a paradigm for the confinement of charges and represents an ideal benchmark model for applying quantum simulation methods to LGTs.

For the latter purpose, the key idea is that cold-atom quantum simulators make possible the implementation of matter fields in presence of artificially designed gauge fields by suitably identifying the gauge degrees of freedom with the internal (for example spin) states of the atom. The first experiments with fermions in presence of such "synthetic" fields have already been proposed and performed, offering very promising perspectives [31–35]. Also, an experiment reproducing 1+1 QED with few qubits has been reported [36]: in this study the experimental setup for the simulation consists of a linear Paul trap, where a string of four 40Ca+ ions is confined. The electronic states of each ion encode a spin up or down state that can be manipulated using laser beams. By using this setup, it was possible to analyze the real-time evolution of the Schwinger mechanism describing the instability of the vacuum due to quantum fluctuations, which manifests itself in the spontaneous creation of electron-positron pairs. This implementation represent the first experimental demonstration of quantum simulation of a lattice gauge theory on a few-qubit trapped-ion quantum simulator and can be considered as a first step towards quantum simulating high-energy theories with atomic physics experiments.

In parallel with experimental efforts, the numerical study of quantum sim-

ulation models of LGTs is of paramount importance to determine their effectiveness in reproducing the main features and phenomenology of the target theory. Novel quantum-inspired numerical techniques, such as DMRG- and MPS-based algorithms [37, 38], fully exploit the entanglement of the states that contribute to the static and dynamical properties of the model, and are able to reduce the computational cost by suitably tailoring the relevant (effective) subspaces in the Hilbert space. From the theoretical point of view, an approach based on quantum simulation models of LGTs paves the way towards a number of problems that were traditionally very difficult to analyze in the context of gauge theories, such as the investigation of possible phase transitions, non-perturbative phenomena and real-time dynamics [22, 39–45].

In first part of this work, we will explore these possibilities by studying the ground-state properties of a class of $\mathbb{Z}_n$ lattice gauge theories in 1+1 dimensions, in which the gauge fields are coupled to spinless fermionic matter. These models, stemming from discrete representations of the Weyl commutator for the $U(1)$ group, preserve the unitary character of the minimal coupling, and have therefore the property of formally approximating lattice QED in one spatial dimension in the large-n limit. In particular, by using a Density-Matrix Renormalization Group (DMRG) algorithm that we developed to incorporate both matter and gauge degrees of freedom, we will unveil the presence of phase transitions. Although the details of these transitions depend on n, their universality class, as well as some of their main features, are n-independent, so that by looking at the large n limit, in which $\mathbb{Z}_n \to U(1)$, one can establish the presence of a phase transition for one-dimensional lattice QED, adding novel rigorous results in the field of quantum simulations of gauge theories.

In the second part of this work, by exploiting the same simulation scheme of the $\mathbb{Z}_n$ models, we will tackle the problem of out-of-equilibrium real-time dynamics of 1+1 dimensional QED. In particular, we will study the stability of the Dirac vacuum with respect to the production of virtual particle/anti-particle pairs induced by quantum fluctuations, and dynamical effects of confinement, such as the string breaking mechanism, which is strictly connected to the question of asymptotic freedom of quarks [46]. We will see that both these phenomena depend on the values of the two parameters of the models, i.e. the fermionic mass and the gauge coupling. In particular we will show that, in the strong coupling regime, the dynamical behaviour of the models strongly deviates from the usual thermalization and relaxation properties [47] which are expected to be found in a many-body non-integrable system, resulting in stable or recurrent evolution of interesting physical quantities. This shows that confinement is not a specific feature of the $U(1)$ Schwinger model, but of the whole class of discrete lattice models we consider, which might be

relevant for the description of future experiments with Rydberg atoms.

It is well known that many efforts in condensed-matter physics are currently devoted to understanding how order can be realized when a very large number of simple and elementary constituents, such as spins, ions, electrons, magnetic moments interact with each other. For a long time, it was thought that all phases of matter were described by Ginzburg-Landau's symmetry-breaking theory, and the transitions between them were described by abrupt changes of the underlying symmetry orders: an ordered state usually appears at low temperature when the system spontaneously loses one of the symmetries present at high temperature (for instance, solid crystals break the translational symmetries of the liquid phases). In this framework, one of the greatest achievements of condensed-matter physics of the last century has been the classification of states of matter by this phenomenon of spontaneous symmetry breaking [48]. This has lead to a universal description of a wide variety of quantum states of matter, and phase transitions thereof, through the identification of effective field theories involving local order parameters, e.g. the magnetization order parameter in a Ising-like system. These order parameters characterize the order (or its absence) in a wide variety of phases of matter and are crucial for understanding the emergence of a rich array of collective phenomena originating from any given microscopic model [49].

However, after the discovery of integer Quantum Hall States (QHS) [52, 53], in which electrons confined to a plane in a strong magnetic field show different quantized plateaus in the *Hall conductance*, it was soon realized that important quantum phases that are not contained in the Ginzburg-Landau symmetry breaking paradigm can exist. In particular, the description of these new states of matter requires the introduction of non-local order parameters, and the interplay of certain mathematical tools of topology, such as topological invariants, with global protecting symmetries of the microscopic models. Two states that show different topological invariants cannot be adiabatically connected (i.e. it is not possible to deform one state into the other by varying the parameters in the Hamiltonian, without going through some singular point), even if they share the same symmetry. Instead, quantum phase transitions induced by symmetry-preserving couplings can occur, which cannot be accounted for by the symmetry-breaking principle. These so-called *symmetry-protected topological* (SPT) phases display an interesting bulk-edge correspondence, since a non-vanishing bulk topological invariant is associated to the presence of edge states that are localized at the boundary of the system, and are responsible for a low-energy response (e.g. conduction) that is robust against symmetry-preserving perturbations. Two condensed-matter models play an important role in the field: the Haldane model [50]

on the honeycomb lattice is the first example of systems including topological phases of matter without external fields. This model shows that the key element to obtain a quantized Hall conductance, as observed in QHS, is the breaking of the so called *time-reversal symmetry*, i.e. symmetry under the inversion of the arrow of time. The second model of inetrest is the Kane-Mele model [51], which shows that the introduction of the spin-orbit coupling may lead to non-trivial topological phases of matter that keep intact the time-reversal symmetry, showing an insulating behavior in the bulk and robust, conducting, gapless edge states on the boundaries.

Since these pioneering works, a variety of SPT phases beyond the integer quantum Hall effect have been identified in different symmetry classes and dimensionalities, such as the so-called topological insulators and superconductors [54, 55], several of which have already been experimentally realized [56].

In analogy to the integer quantum Hall effect, where the introduction of inter-particle interactions leads to strongly-correlated phases with exotic properties, e.g. excitations with fractional statistics [57, 58], a problem of current and active interest in the community is to understand the fate of this variety of SPT phases in the presence of interactions [59]. So far, the typical models considered have focused on instantaneous interactions involving action at a distance (e.g. screened Coulomb interactions and truncated versions thereof yielding Hubbard-type couplings). The more fundamental situation of strongly-correlated SPT phases where interactions are carried by bosons, and dictated by local gauge symmetries, remains largely unexplored.

From a fundamental perspective, studying a gauge field theory that incorporates SPT phases would extend the interest of SPT phases towards the high-energy physics domain, possibly giving rise to a rich playground where topological effects coexist with interesting high-energy physics phenomena such as confinement and charge shielding, string breaking, quantum anomalies, or chiral symmetry breaking.

In the last part of this work, in connection with the $\mathbb{Z}_n$ lattice gauge theories we have previously considered, we will unveil an interesting interplay of symmetry and topology by demonstrating the existence of SPT phases in the presence of gauge interactions and initiating a systematic study into a wider class of such systems. More specifically, we will introduce an alternative discretization of the continuum Schwinger model leading to the *topological Schwinger model*: an Abelian gauge theory that regularizes quantum electrodynamics in (1+1) dimensions and describes the coupling of the electric field to a fermionic SPT matter sector. In contrast to the standard discretization of the massive Dirac fields, where one explicitly breaks translational invariance by using a staggered mass [11], we will chose to break the symmetry

by a dimerized tunnelling. In the continuum limit, such a tunnelling leads to Dirac fermions with a topological mass, and a matter sector that can be described as a fermionic SPT phase with a non-vanishing topological invariant and localised edge states. In particular, we will show that the underlying topology promotes the so-called vacuum θ angle, a constant parameter in the standard Schwinger model that plays an important role also in the context of QCD [60], into a dynamical quantum-mechanical operator with its own dynamics depending on the density of the topological edge states. We will use bosonization [61] and DMRG techniques to study the rich phase diagram of the model in great detail, opening an interesting route to study topological phases of matter in the context of gauge theories.

The results of this thesis have been collected in four papers and have been published during the PhD. The first part (Chapter 1) can be found in

- E. Ercolessi, P. Facchi, G. Magnifico, S. Pascazio, F. V. Pepe, *Phase transitions in $\mathbb{Z}_n$ gauge models: Towards quantum simulations of the Schwinger-Weyl QED*, Phys. Rev. D **98**, 074503 (2018).

The second part (Chapter 2) can be found in

- G. Magnifico, P. Facchi, S. Pascazio, F. V. Pepe, E. Ercolessi, *Real Time Dynamics and Confinement in the Z_n Schwinger-Weyl lattice model for 1+1 QED*, arXiv:1909.04821 (in publication on Quantum Journal).

The third part (Chapter 3) can be found in

- G. Magnifico, D. Vodola, E. Ercolessi, S. P. Kumar, M. Müller, and A. Bermudez, *Symmetry-protected topological phases in lattice gauge theories: Topological QED_2*, Phys. Rev. D **99**, 014503 (2019).

- G. Magnifico, D. Vodola, E. Ercolessi, S. P. Kumar, M. Müller, and A. Bermudez, *$\mathbb{Z}_N$ gauge theories coupled to topological fermions: QED_2 with a quantum-mechanical θ angle*, Phys. Rev. B **100**, 115152 (2019).

In addition to the previous papers which represent the core of this PhD thesis, other results have been obtained in the context of quantum many-body systems, entanglement and topological phases of matter. They can be found in

- G. Giudici, A. Angelone, G. Magnifico, Z. Zeng, G. Giudice, T. Mendes-Santos, and M. Dalmonte, *Diagnosing Potts criticality and two-stage melting in one-dimensional hard-core boson models*, Phys. Rev. B **99**, 094434 (2019).

- G. Ghelli, G. Magnifico, C. Degli Esposti Boschi, E. Ercolessi, *Topological phases in two-legged Heisenberg ladders with alternated interactions*, arXiv:1908.08440.

- P. Fromholz, G. Magnifico, V. Vitale, T. Mendes-Santos, M. Dalmonte, *Entanglement topological invariants for one-dimensional topological superconductors*, arXiv:1909.04035.

Chapter 1

Phase Transitions in $\mathbb{Z}_n$ Gauge Models: Towards Quantum Simulations of the Schwinger-Weyl QED

This chapter is organized as follows. In Section 1.1, we introduce the massive Schwinger model in $1+1$ dimensions and discuss the paths to discretization of space and gauge degrees of freedom. Section 1.2 includes the definition of $\mathbb{Z}_n$ gauge models and the presentation of their general features and scaling properties. In Section 1.4 we study in detail the case $n = 3$, characterizing its ground state properties and the quantum phase transition at a negative critical mass, in absence of background field. Section 1.5 is devoted to a presentation of the results obtained in all cases $n = 2 \div 8$, $n \neq 3$, focusing on the different phenomenology of the even and odd cases, while the details of the numerical results of all these cases are given in the Appendix A. In Section 1.6 we summarize our results and recover the $U(1)$ model in the limit of large n. In section 1.7, we comment on a possible implementation of the proposed class of models in a cold atomic platform. We finally draw our conclusions in Section 1.8.

1.1 Discretization of one-dimensional QED

Quantum Electrodynamics in one spatial dimension is a $U(1)$ gauge theory, describing the interaction of a charged particle ("electron"), represented by a spinor field $\psi(t, x)$, and the electromagnetic field $F_{\mu\nu} = \partial_\mu A_\nu - \partial_\nu A_\mu$, associated to the potential A_μ, with $\mu, \nu = 0, 1$. The classical Lagrangian

density is determined by the minimal coupling prescription:

$$\mathcal{L} = \psi^\dagger \gamma^0 \left[\gamma^\mu (\mathrm{i}\partial_\mu + gA_\mu) - m\right] \psi - \frac{1}{4} F_{\mu\nu} F^{\mu\nu}, \tag{1.1}$$

where m and g are the electron mass and charge, respectively, and $\{\gamma^\mu, \gamma^\nu\} = 2\eta^{\mu\nu}$ with $\eta = \mathrm{diag}(1, -1)$. The properties of the theory are strongly characterized by the absence of transverse degrees of freedom: the electron, described by a two-component spinor, is spinless, and the only independent component of the electromagnetic tensor is the electric field $E = F_{01}$. While quantization of the spinor field is determined by the canonical equal-time anticommutators

$$\{\psi(t, x), \psi(t, x')\} = 0, \tag{1.2}$$

$$\{\psi(t, x), \psi^\dagger(t, x')\} = \delta(x - x'), \tag{1.3}$$

a gauge choice is necessary to quantize the electromagnetic potential. In the canonical gauge, the temporal component A_0 is set to zero, while the spatial component $A := A_1$ is taken as the conjugate variable to E:

$$[E(t, x), A(t, x')] = \mathrm{i}\delta(x - x'). \tag{1.4}$$

This choice, leading to the Hamiltonian

$$H = \int \mathrm{d}x \left\{ \psi^\dagger \gamma^0 \left[-\gamma^1 (\mathrm{i}\partial_1 + gA) + m\right] \psi + \frac{E^2}{2} \right\}, \tag{1.5}$$

does not allow one to enforce Gauss' law $G(x) = 0$, with

$$G(x) = \partial_1 E(x) - g\psi^\dagger(x)\psi(x), \tag{1.6}$$

as an operator constraint. However, since $[G(x), G(x')] = 0$ and $[G(x), H] = 0$ due to (1.4), it is possible to select the physical subspace of states $|\psi\rangle$ for which $G(x)|\psi\rangle = 0$, which will be denoted by

$$G(x) \approx 0, \tag{1.7}$$

at all space points.

In the following, we will consider two kinds of discretization, towards classical and quantum simulations of the model. The first one is spatial discretization: the continuum model will be replaced by an approximation on a linear lattice of points with spacing a, making the continuous space variable $x \in \mathbb{R}$ discrete: $x \in \mathbb{Z}$. The second one is the approximation of the gauge group $U(1)$ with a finite group, which is essential if one wants to work

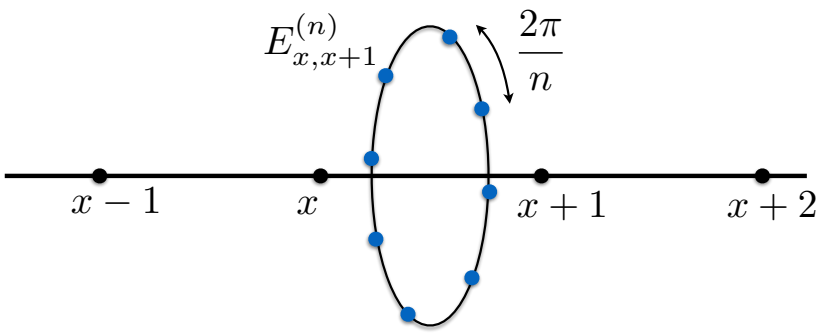

Figure 1.1: Discretization of the Schwinger model. Fermionic matter lives on sites $x \in \mathbb{Z}$. Electric field $E^{(n)}_{x,x+1}$ lives on links between adjacent sites and takes discrete values, $e_k = \sqrt{\frac{2\pi}{n}}(k - \frac{n-1}{2})$, with $k \in \mathbb{Z}_n = \{0, 1, \cdots, n-1\}$.

with a finite number of local degrees of freedom in the gauge variables (i.e. a finite number of electric field states). This can be done essentially in two ways, based on the generalization of the commutation relation $[E, U] = \eta U$, where E and A are two conjugated operators ($[E, A] = \mathrm{i}$), $U = \mathrm{e}^{-\mathrm{i}\eta A}$ is the gauge comparator and $\eta \in \mathbb{R}$ is a constant with the same dimensions as E. One option is to focus on the preservation of the above commutator. This is the approach taken, for example, in quantum link models [62–65], in which the operators E and U are replaced with spin variables: in this case one obtains a finite dimensional (but nonunitary) representations of the canonical commutation relations. Another option is to require that the *group* commutator $\mathrm{e}^{\mathrm{i}\xi E}\mathrm{e}^{-\mathrm{i}\eta A} = \mathrm{e}^{\mathrm{i}\eta\xi}\mathrm{e}^{-\mathrm{i}\eta A}\mathrm{e}^{\mathrm{i}\xi E}$, which is equivalent to the previous one in the $U(1)$ case, be satisfied by unitary operators for discrete values of η and ξ [29]. We will follow the latter strategy, that entails the reduction of gauge invariance to a finite group $\mathbb{Z}_n$. A pictorial representation of the gauge degrees of freedom is shown in Fig. 1.1.

In this way, we obtain an *exact* finite implementation of the gauge group commutator at the Hamiltonian level.

1.2 Lattice Z_n-QED model

The Schwinger model (1.5) described in the previous section can be discretized on a one-dimensional lattice. For convenience, we shall first redefine, the vector potential $A \to A/g$ and the electric field $E \to gE$. With this transformation, that leaves the commutation relation (1.4) unchanged, the charge is absorbed in the minimal coupling, to reappear in the energy density of the free electric field. Correspondingly, we redefine the parameters

in the one parameters groups $U(\eta), V(\xi)$ by $\eta \to \eta/g, \xi \to g\xi$.

The lattice Hamiltonian reads [9, 65, 66]

$$H = -\frac{1}{2a}\sum_x \left(\psi_x^\dagger U_{x,x+1}\psi_{x+1} + \text{H.c.}\right) + m\sum_x (-1)^x \psi_x^\dagger \psi_x + \frac{g^2 a}{2}\sum_x E_{x,x+1}^2, \tag{1.8}$$

with x labelling the sites of a one-dimensional lattice of spacing a. Here:
i) fermionic matter is represented by one-component creation/annihilation spinor operators $\psi_x^\dagger, \psi_x$, defined on each site x, so that $\sum_x \psi_x^\dagger \psi_x$ represents the total number of fermions in the system;
ii) a staggered mass $(-1)^x m$ is introduced, so that the positive- and negative-mass components of the Dirac spinor live respectively at even and odd lattice sites, avoiding in this way the fermion-doubling problem [8, 9, 11, 13];
iii) gauge fields are defined on the links $(x, x+1)$ of the lattice through the pair of variables $E_{x,x+1}$ (electric field) and $A_{x,x+1}$ (vector potential) or equivalently the comparators $U_{x,x+1}(\eta) = \mathrm{e}^{-\mathrm{i}\eta A_{x,x+1}}$ and $V_{x,x+1}(\xi) = \mathrm{e}^{+\mathrm{i}\xi E_{x,x+1}}$, commuting at different sites, and satisfying the group canonical commutation relations:

$$V_{x,x+1}(\xi)\, U_{x,x+1}(\eta) = \mathrm{e}^{\mathrm{i}\eta\xi} U_{x,x+1}(\eta)\; V_{x,x+1}(\xi), \tag{1.9}$$

for $\xi, \eta \in \mathbb{R}$, which are equivalent exponentiated versions of the (algebra) canonical commutation relations $[E_{x,x+1}, A_{x,x+1}] = \mathrm{i}$.
Notice that in (1.8), the coupling constants m and g are the same as in the continuum, both with the dimensions of energy, while all the field operators are dimensionless.

In analogy to what is done in fermionic lattice models that are usually used to describe condensed matter systems and for reasons that will become clear in the next section, in the following we will actually use a slightly modified Hamiltonian by introducing an additional dimensionless parameters t in front of the first, kinetic, term so to write the dimensionless Hamiltonian

$$h_t = \frac{2}{g^2 a} H_t = -\frac{t}{g^2 a^2}\sum_x \left(\psi_x^\dagger U_{x,x+1}\psi_{x+1} + \text{H.c.}\right) + \frac{2m}{g^2 a}\sum_x (-1)^x \psi_x^\dagger \psi_x + \sum_x E_{x,x+1}^2\,, \tag{1.10}$$

proportional to the Hamiltonian density. We can also see from this expression that the coefficient $g^2 a/2$ fixes the scale of the mass, while the coefficient $g^2 a^2$ the one of the parameter t. Thus, the numerical simulations described

in Sections 1.4 and 1.5 will be performed by setting $g^2a/2 = 1$ and $g^2a^2 = 1$. The standard lattice Schwinger model is then recovered for $t = 1$.

In addition, the theory must respect Gauss' law, encoding the $U(1)$ gauge symmetry of the model, that reads

$$G_x \equiv \psi_x^\dagger \psi_x + \frac{1}{2}[(-1)^x - 1] - (E_{x,x+1} - E_{x-1,x}) \approx 0. \tag{1.11}$$

The Hamiltonian (1.8) is invariant under C and P symmetries that for staggered fermions read (assuming an infinite lattice or setting $-x \equiv 2L - x$ for a finite lattice with an even number $N = 2L$ of sites, labeled from 0 to $2L-1$):

$$P : \begin{cases} \psi_x \to \psi_{-x}, & \psi_x^\dagger \to \psi_{-x}^\dagger, \\ E_{x,x+1} \to E_{-(x+1),-x}, & U_{x,x+1} \to U_{-(x+1),-x}^\dagger, \end{cases} \tag{1.12}$$

$$C : \begin{cases} \psi_x \to (-1)^{x+1} \psi_{x+1}^\dagger, & \psi_x^\dagger \to (-1)^{x+1} \psi_{x+1}, \\ E_{x,x+1} \to -E_{x+1,x+2}, & U_{x,x+1} \to U_{x+1,x+2}^\dagger. \end{cases} \tag{1.13}$$

The Hamiltonian (1.8) can be approximated via a discrete Abelian $\mathbb{Z}_n$-gauge model [29], that can be obtained from a *finite dimensional* representation of the two-parameter projective unitary Weyl [67] group $\left\{ \mathrm{e}^{\mathrm{i}(\xi E_{x,x+1} - \eta A_{x,x+1})} \right\}_{\xi,\eta \in \mathbb{R}}$. For the two particular cases $(\xi, \eta) = (0, \sqrt{2\pi/n})$ and $(\xi, \eta) = (\sqrt{2\pi/n}, 0)$ one gets the two operators $U_{x,x+1} = \mathrm{e}^{-\mathrm{i}\sqrt{\frac{2\pi}{n}} A_{x,x+1}}$ and $V_{x,x+1} = \mathrm{e}^{\mathrm{i}\sqrt{\frac{2\pi}{n}} E_{x,x+1}}$, that satisfy the commutation relations

$$U_{x,x+1}^\ell V_{x,x+1}^k = \mathrm{e}^{\mathrm{i}\frac{2\pi}{n} k\ell} V_{x,x+1}^k U_{x,x+1}^\ell \quad \text{with } k, \ell \in \mathbb{Z}_n. \tag{1.14}$$

which is a discrete $\mathbb{Z}_n$ version of (1.9). This representation can be implemented by considering an n-dimensional Hilbert space $\mathcal{H}_n$ defined on each link, and choosing an orthonormal basis $\{|v_k\rangle\}_{0 \le k \le n-1}$. Dropping the link index, we consider the diagonal operator V acting as

$$V|v_k\rangle = \mathrm{e}^{-\mathrm{i}2\pi k/n} |v_k\rangle. \tag{1.15}$$

The operator U is instead defined as that operator that performs a cyclic permutation of the basis states:

$$U|v_k\rangle = |v_{k+1}\rangle \quad \text{for } k < n-1, \quad U|v_{n-1}\rangle = |v_0\rangle. \tag{1.16}$$

Some simple algebra shows that these operators do indeed satisfy the Schwinger-Weyl commutation relations (1.14). Let us remark that this representation exactly implements the unitarity of both operators.

Thus the dynamics of the $\mathbb{Z}_n$-model is determined by the Hamiltonian (1.8), where the discrete version of the electric field $E_{x,x+1}$ is given by the Hermitian operator that is diagonal in the $\{|v_k\rangle\}$ basis, with eigenvalues

$$e_k = \sqrt{\frac{2\pi}{n}} \left(k - \frac{n-1}{2} + \phi \right) . \tag{1.17}$$

In all cases, the eigenvalues of the electric field are symmetric around zero, with a maximum value $E_{\max} = \sqrt{2\pi/n}(n-1+\phi)/2$. We notice that, for $\phi = 0$, it is possible to have zero electric field only if n is odd. A value $\phi \neq 0$ corresponds to adding a background field that can be obtained by placing charges at the boundaries of the chain, thus yielding different charge sectors, that are known to be super-selected. It is indeed known that this model displays θ-vacua [68] , which can be related to the axial anomaly [69] via the spectral flow of the Hamiltonian operator (when imposing periodic boundary conditions) or to unusual twisted boundary conditions for the fermionic field [70]. In this case the P and C symmetries are explicitly broken. In the case of even n, the minimum eigenvalues (1.17) are doubly degenerate for $\phi = 0$. As a consequence, in the strong-coupling limit, in which the U-dependent terms in (1.8) are neglected, the energetic cost of creating a fermion-antifermion pair from the vacuum vanishes: this feature is typical of theories with $\theta = \pi$ [68].

1.3 Scaling properties of the Hamiltonian

Before starting to numerically investigate the Hamiltonian, some comments are in order to establish the correctness of Eq. (1.10) to suitability represent a quantum simulator for one-dimensional QED. Being in particular interested in its critical properties, our analysis needs to contain a careful check of the scaling properties of the discretized Hamiltonian as we change the different parameters that appear in it, including the $a \to 0$ limit (continuum limit), the $N \to \infty$ limit (infinite volume limit), the $n \to \infty$ limit ($U(1)$-limit). Close to a critical point, at which physical constants and observables are functionally related by universal laws, it is very hard to control these different cases independently, both from an analytical and a numerical point of view. However, we can resort to well-known techniques based on a finite-size scaling analysis guided by universal scaling properties. We have chosen to perform this study in two steps: first, we consider a particular $\mathbb{Z}_n$-model, by keeping n fixed, and perform a finite-size scaling in the dimension of the spatial lattice; second, we let n increase and analyze the large-n limit.

To this end, we first notice that the parameter t can be used to understand critical properties of the model. Let us suppose that the system undergoes a phase transition for a critical value of the mass, $m_c(t)$, which may depend on t. At this particular point the dimensonless Hamiltonian (1.10) should be scale invariant. The coefficient t can be absorbed in a re-scaling of the lattice spacing, $a \to \tilde{a} = a/\sqrt{t}$, and:

$$\begin{aligned} h_c = &- \frac{1}{g^2 \tilde{a}^2} \sum_x \left(\psi_x^\dagger U_{x,x+1} \psi_{x+1} + \text{H.c.}\right) \\ &+ \frac{2m_c(t)}{\sqrt{t}\, g^2 \tilde{a}} \sum_x (-1)^x \psi_x^\dagger \psi_x + \sum_x E_{x,x+1}^2 \,, \end{aligned} \tag{1.18}$$

In a mean-field approach, in which possible anomalous dimensions of the field are neglected, the coefficient in front of the second addend must be independent of t. In other words, the critical value of the mass scales like

$$m_c(t) = \alpha \sqrt{t}, \tag{1.19}$$

where $\alpha \equiv m_c(t = 1)$. We will examine accurately how the critical value of the mass depends on t in the numerical simulations of the next sections, where we will see that its behaviour does not significantly deviates from the one predicted here. Therefore we will obtain the continuum limit critical mass m_c by setting: $m_c = m_c(t = 1) = \alpha$.

Incidentally, let us remark that the limit $t \to \infty$ is not equivalent to the limit $a \to 0$, since the coefficient t weights the kinetic term differently with respect to the mass and the electric energy terms; in particular, in the $t = 0$ case we recover a classical limit which can be exactly solved, while in the large $t \to \infty$ limit we deal with a pure kinetic Hamiltonian which cannot display any phase transition.

Second, we want to study the large-n limit. It is important to notice that, as shown in [29], the scaling of the eigenvalues of the electric field with n as given in Eq. (1.17) is fixed by requiring that the $U(1)$-limit is recovered when $n \to +\infty$. Also, recalling that two consecutive values of the electric field differ by $\sqrt{2\pi/n}$, it is convenient to collect such a factor and work with the dimensionless Hamiltonian

$$\begin{aligned} h_t^{(n)} = &\frac{2}{g_n^2 a} H_t^{(n)} = - \frac{t}{g_n^2 a^2} \sum_x \left(\psi_x^\dagger U_{x,x+1} \psi_{x+1} + \text{H.c.}\right) \\ &+ \frac{2m}{g_n^2 a} \sum_x (-1)^x \psi_x^\dagger \psi_x + \sum_x \tilde{E}_{x,x+1}^2 \,, \end{aligned} \tag{1.20}$$

where now $\tilde{E}_{x,x+1}$ has eigenvalues $(k-(n-1)/2+\phi)$ with unit spacing (hence, independent of n), and

$$g_n = g\sqrt{2\pi/n}. \tag{1.21}$$

In the same spirit as before, we can conclude that now (with a slight abuse of notation)

$$m_c(t) = \alpha_n \sqrt{t}. \tag{1.22}$$

Comparing the Hamiltonian density (1.20) to (1.18) in the limit $n \to \infty$, we can conclude that the asymptotic value of $\alpha_n g/g_n$ must approach the coefficient α appearing in Eq. (1.19), namely

$$\alpha = \lim_{n\to\infty} \alpha_n \sqrt{n/2\pi}. \tag{1.23}$$

In the following, to perform numerical calculations, we will consider the Hamiltonian (1.20) defined on a lattice of size $N = 2L$ with open boundary conditions. We will work in the sector with one fermion for each "physical site", i.e. with $N_{\text{part}} = N/2 = L$ particles. Also, as explained above, we will set $g^2a/2 = 1$ (which sets the units of energy) and $g^2a^2 = 1$ (which sets the units of t).

We will first present the $\mathbb{Z}_3$-model, in order to illustrate all the details of our treatment. We will then discuss the general $\mathbb{Z}_n$-model, for both odd and even n. As we will see, these two cases need to be considered separately.

1.4 Lattice $\mathbb{Z}_3$-QED model

1.4.1 Hilbert space and gauge-invariant subspace

As mentioned in Sec. 1.2, in the Schwinger model each "physical fermion" is represented by a pair of staggered fermions sitting in nearby sites, with even/odd sites occupied by positive/negative mass particles. Thus the vacuum state (Dirac sea) is obtained by leaving the even sites empty and occupying the odd ones. The presence/absence of a fermion in an even/odd site is interpreted as the presence of a quark/anti-quark, while a meson is a configuration made up of a quark and an anti-quark. This is shown in Fig. 1.2(a). On each link $(x, x+1)$, the electric field can only assume one of the three values $E = \sqrt{2\pi/3}(k-1)$, with $k \in \mathbb{Z}_3 = \{0, 1, 2\}$, which will be represented as an arrow pointing left, an un-oriented segment, and an arrow pointing left, respectively, as shown in Fig. 1.2(b).

Thus the total Hilbert space associated with an even site, together with its two adjacent links, is $2 \times 3 \times 3 = 18$ dimensional. But Gauss' law forces

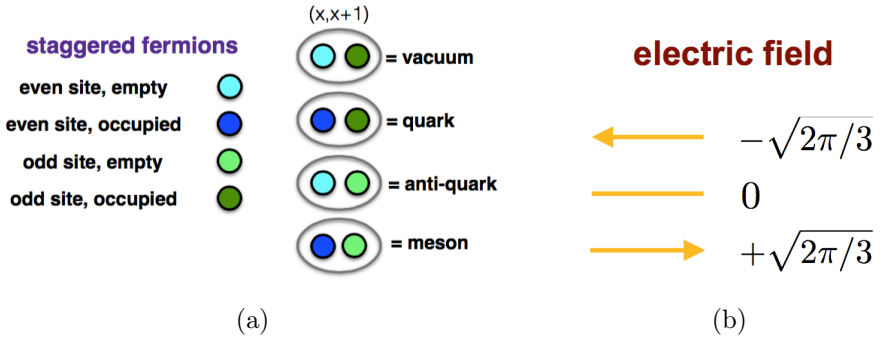

(a) (b)

Figure 1.2: $\mathbb{Z}_3$-model. Local Hilbert space for (a) staggered fermions; (b) electric field.

the physical states to belong to an invariant subspace which is constructed out of those states for which the value of the electric field k_r at the right link is either $k_r = k_l$, if the site is empty, or $k_r = k_l + 1 (\mathrm{mod}\, 3)$ if the site between links is occupied by a (positive mass) fermion. The situation is similar for odd sites, for which Gauss' law constrains physical states to have either $k_r = k_l - 1 (\mathrm{mod}\, 3)$, if the site between links is empty, or $k_r = k_l$ if the site is occupied by a (negative mass) fermion. This is displayed in Fig. 1.3(a). Notice that we have $2 \times 3 = 6$ independent configurations for each site. The gauge invariant states of a "physical site" are obtained by gluing together an even and an odd site that share a common value for the electric field in the link between them, obtaining $2 \times 6 = 12$ possible configurations, as shown in Fig. 1.3(b).

It is easy to see that, for a chain with N sites (with open boundary conditions), the dimension of the gauge-invariant subspace is $2^N \times 3$. Some notable examples of gauge-invariant states in a chain are shown in Fig. 1.4.

The ground state of the Hamiltonian (1.8) will be given by the completely filled Dirac sea (see Fig. 1.5(a)) for large positive m, while for large negative m the system will tend to choose between the two states shown in Fig. 1.5(b), where mesons/antimesons have formed. Notice that the Dirac sea is invariant under both parity and charge conjugation, while P and C map the mesonic and antimesonic states into each other. These two cases are clearly distinguished by the mean value of the electric field operator

$$\Sigma = \frac{1}{N} \sum_x \langle E_{x,x+1} \rangle \tag{1.24}$$

that we will use as a kind of order parameter, since it vanishes for the Dirac sea and takes the values $\pm\pi/3$ for the mesonic/antimesonic states. An abrupt

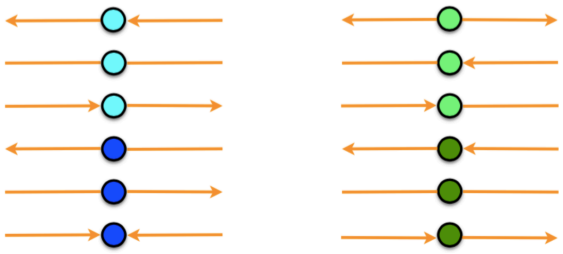

(a)

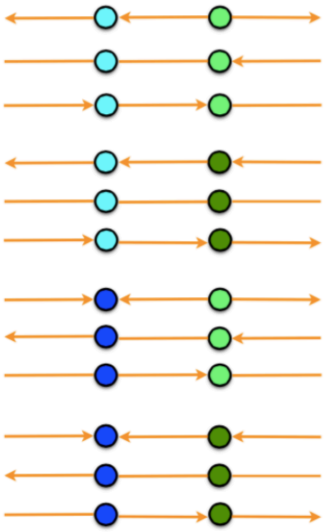

(b)

Figure 1.3: $\mathbb{Z}_3$-model. (a) Gauge-invariant Hilbert space associated with even/odd sites; (b) Gauge-invariant Hilbert space associated with a pair of even/odd sites, i.e. a "physical site".

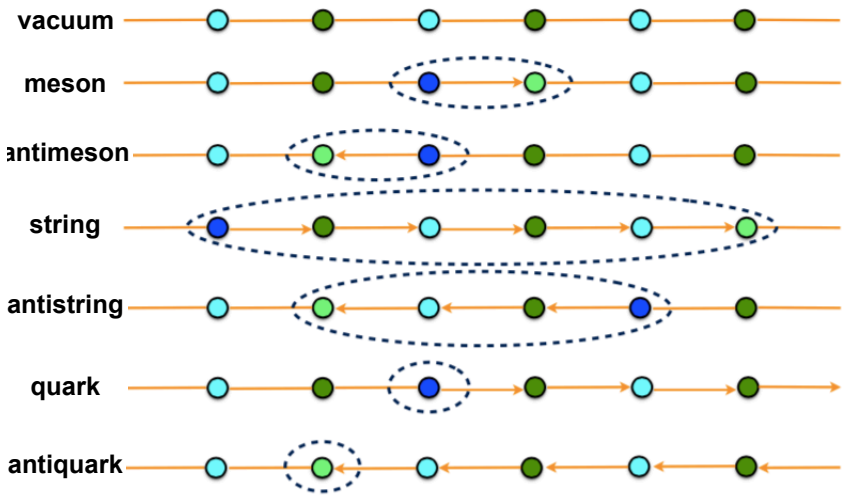

Figure 1.4: $\mathbb{Z}_3$-model. Some notable gauge invariant configurations.

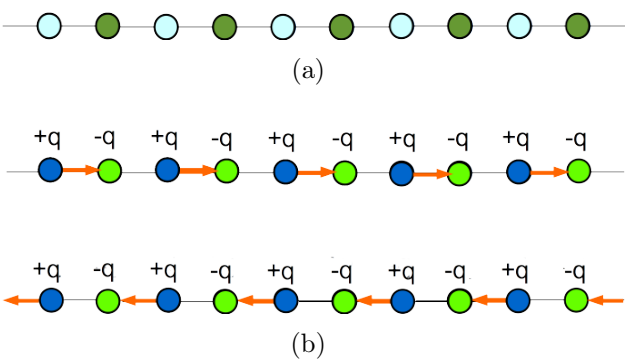

Figure 1.5: $\mathbb{Z}_3$-model. (a) Dirac sea; (b) Mesonic (top) and antimesonic (bottom) states.

change of this quantity signals the existence of a possible phase transition, whose existence has to be confirmed by looking at the appropriate scaling of observables and thermodynamical quantities.

1.4.2 Numerical investigation of the critical point with no background field

We perform numerical calculations by means of a finite-size DMRG code [71] in which gauge invariance is exactly enforced. This is obtained by using a unit cell given by a pair of nearby (even and odd) sites, whose local Hilbert space is the span of the 12 gauge-invariant states described in Fig. 1.3. This is implemented at each step of the algorithm, with a twofold advantage: decreasing the computing time by working in a restricted space, and avoiding transitions out of the gauge-invariant subspace. We work with up to $N = 80$ sites ($L = 40$ pairs), while keeping 1000 DMRG states at most. These values are large enough to ensure stability of our findings and small errors.

We first numerically study the Hamiltonian (1.20) at the CP-invariant point, i.e. in absence of a background field: $\tilde{E}_{x,x+1} \in \{-1, 0, +1\}$. We start by choosing $t = 2\pi/3$ so as to work with the operator

$$h^{(3)}_{t=\frac{2\pi}{3}} = -\sum_x \left(\psi^\dagger_x U_{x,x+1}\psi_{x+1} + \text{H.c.}\right) + \frac{3}{2\pi} m \sum_x (-1)^x \psi^\dagger_x \psi_x + \sum_x \tilde{E}^2_{x,x+1}. \tag{1.25}$$

Notice that, here and in the following sections, mass is expressed in units of $g^2 a/2$. The behavior of the observable Σ as a function of m is displayed in Fig. 1.6(a) for different system sizes, ranging from $L = 12$ to $L = 40$. We see that, as expected, Σ essentially vanishes at large positive m and tends to the value $\sqrt{2\pi/3}/2 \simeq 0.724$ for large negative m.

In Fig. 1.6(b) we zoom on the central region, showing a steeper transition as the system size increases. This strongly suggests that we are in presence of a phase transition, at a critical value of the mass which corresponds to the point where all curves intersect. We can estimate this value if we make a hypothesis about the nature of the phase transition: indeed, if we know the critical exponents, we can calculate m_c by using the fact that Σ should scale with the system size N according to the finite-size scaling formula [72]

$$\Sigma = N^{-\frac{\beta}{\nu}} \lambda\left(N^{\frac{1}{\nu}}(m - m_c)\right) \tag{1.26}$$

where λ is a universal function. By taking into account suggestions from the continuum limit [68] and the symmetries of the model, we anticipate that the

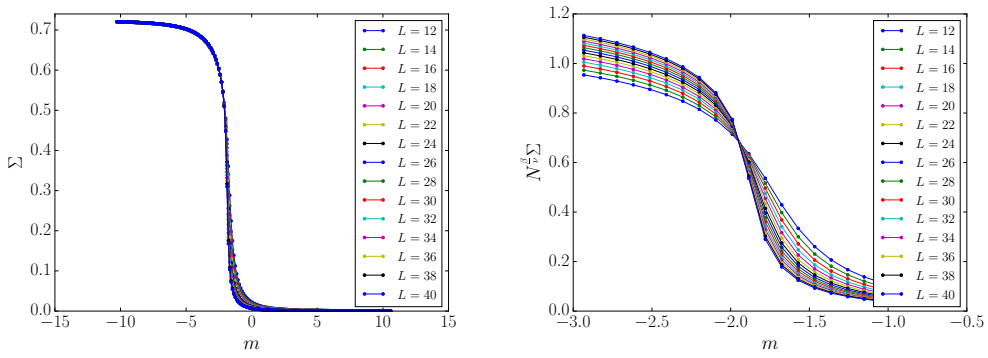

(a) (b)

Figure 1.6: $\mathbb{Z}_3$-model. (a) Order parameter Σ as a function of m, for different system size L; (b) Same plot as in (a), in the vicinity of the phase transition.

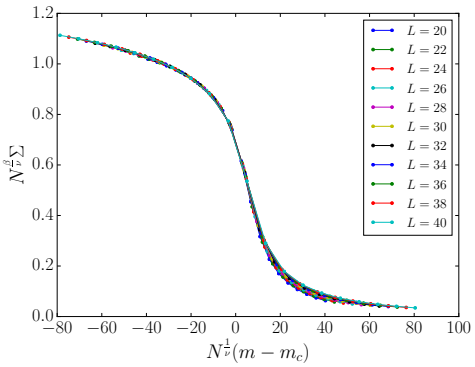

Figure 1.7: $\mathbb{Z}_3$-model. Scaling of $\lambda(x)$ for different system size L.

phase transition is of the Ising-type, so that $\beta = 1/8$ and $\nu = 1$. A fit of the data yields then $m_c = -1.948 \pm 0.025$, where the error has been estimated as the semi-interval between the numerical points. We now have to look at the numerical curves given by $N^{\frac{\beta}{\nu}}\Sigma$ versus $N^{\frac{1}{\nu}}(m - m_c)$, for different N, which should all collapse onto the same universal curve $\lambda(x)$. This behaviour is clearly seen in Fig. 1.7.

Once we have an estimate for the critical mass, we can confirm the validity of our hypothesis by calculating other quantities. Figure 1.8 displays the entanglement entropy of a subsystem of size $L/2$ at the critical point, which—according to conformal field theory [73]—should scale logarithmically with

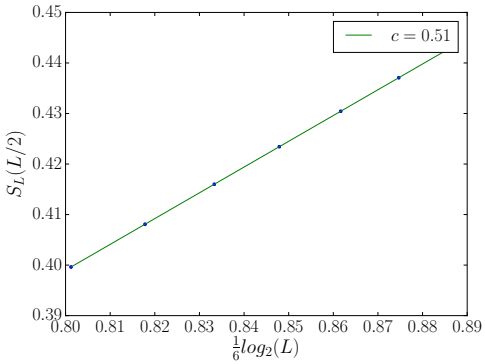

Figure 1.8: $\mathbb{Z}_3$-model. Entanglement entropy $S_L(L/2)$ versus system size L.

the system size according to the law

$$S_L\left(\frac{L}{2}\right) = \frac{c}{6}\log_2(L) + s_0, \tag{1.27}$$

where s_0 is a constant (which can depend on the boundary conditions and other details of the model) while c is the central charge. The fit yields $c = 0.51 \pm 0.01$, in perfect agreement with the central charge of the Ising model, $c = 1/2$.

Additional information can be obtained by looking at the scaling of excited states with the size of the system: Figures 1.9(a) and 1.9(b) display the behaviour of the gaps Δ and Γ of the first two excited states, which—again according to conformal field theory [74]—should obey

$$\Delta = \varepsilon_1(N) - \varepsilon_0 = \tfrac{\pi v_s x_s}{N^2}, \tag{1.28}$$

$$\Gamma = \varepsilon_2(N) - \varepsilon_0 = \tfrac{\pi v_s (x_s+1)}{N^2}, \tag{1.29}$$

ε_0 being the ground state energy density, v_s a speed, and x_s the surface critical exponent, which is equal to 2 for the Ising model with open boundary conditions. We numerically find

$$\frac{\Delta}{\Gamma} = \frac{x_s}{x_s+1} = 0.6671 \pm 0.0008 \Rightarrow x_s = 2.004 \pm 0.007. \tag{1.30}$$

Plugging this result back into Eq. (1.28) we can also estimate the speed v_s, obtaining

$$v_s = 1.56 \pm 0.08 \tag{1.31}$$

(a number very close to $\pi/2$). We remark that surface exponents are found for states that can be obtained from the ground state by changing from periodic

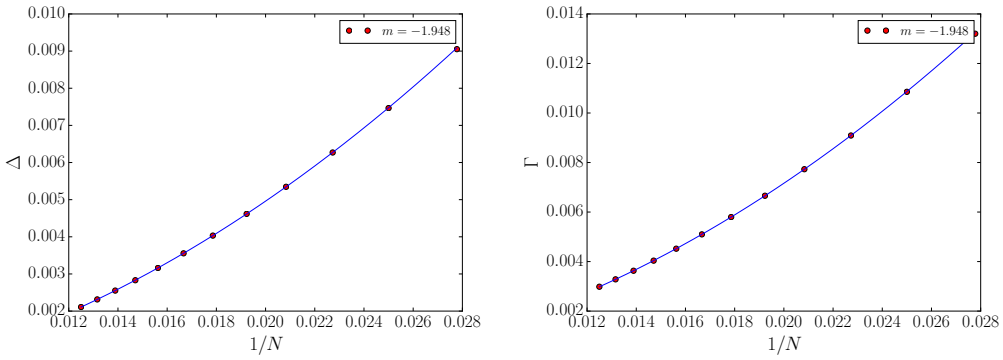

(a) (b)

Figure 1.9: $\mathbb{Z}_3$-model. (a) Gap Δ of the first excited state versus system size $N = 2L$; fit according to Eq. (1.28). (b) Gap Γ of the second excited state versus system size $N = 2L$; fit according to Eq. (1.29).

to anti-periodic boundary conditions. The system here shows spontaneous symmetry breaking to one of the two degenerate polarized states and thus the first excited state can be represented as a kink-like solution which interpolates between these two degenerate polarized minima, in agreement with what is found in the continuum [68]. These results are also fully compatible with recent [45, 75] and less recent [76] numerical results. Interestingly, similar conclusions hold also at finite temperature [77].

For $t = 0$, the system undergoes a (first order) phase transition between the Dirac sea, depicted in Fig. 1.5(a), with an energy per pair $E_{\text{Dirac}}/L = -m$, and the mesonic state in Fig. 1.5(b), with energy per pair $E_{\text{meson}}/L = m + 2\pi/3$. The critical value of the mass $m_0^{(3)} = -\pi/3 \simeq -1.047$ is obtained at $E_{\text{meson}} = E_{\text{Dirac}}$.

In order to test the validity of Eq. (1.23), we have repeated this procedure for several values of t, checking that the Ising transition is always present and calculating numerically $m_c(t)$. Our numerical findings for $m_c(t)$ as a function of t, as well as other useful information, are given in Appendix A.

A numerical fit of the form

$$m_c(t) = m_0^{(n)} + \alpha_n \sqrt{t} + \beta_n t \tag{1.32}$$

yields the values

$$m_0^{(3)} = -1.0472 \pm 0.0001, \tag{1.33}$$

$$\alpha_3 = -0.603 \pm 0.001, \tag{1.34}$$

$$\beta_3 = -0.02 \pm 0.01. \tag{1.35}$$

Let us notice that, as expected from the predicted behaviour (1.23), the coefficient of the linear term is much smaller than the one of the square-root term, thus yielding a negligible correction, at least for not too large values of t. This will also be apparent in Fig. 1.15 (green points and green fitting curve).

1.4.3 Numerical investigation of the critical point in presence of a background field

It is known [68] that the Schwinger model should exhibit a phase transition only at the CP-invariant point. In order to check if this is the case also in our model, we have scrutinized the effects of a constant background field. We present here just one representative example, by considering an electric field

$$\tilde{E}_{x,x+1} = k + 1/3, \qquad k \in \{-1, 0, +1\} \tag{1.36}$$

in the Hamiltonian (1.25).

As shown in Fig. 1.10(a), the observable Σ still shows a very sharp transition between a negative and a positive value. But we are now in presence of a cross-over, rather than a phase transition, as it can be inferred by performing a scaling analysis. Indeed, the function λ in Eq. (1.26) changes for different system size N and does not have a universal character, as one can infer from Fig. 1.10(b). Also, the entanglement entropy $S_L(l)$ does not scale with the size l of the interval, as predicted by conformal field theory [73], but is rather constant, except for some small edge effects, also at the crossing point $m^* = -0.325$ (see Fig. 1.11(a)). These results suggest that, in presence of a background field, the gap never closes, as the numerics confirms (see Fig. 1.11(b), red dots).

Finally, we also checked the case of a background electric field which is halfway between two integer values:

$$\tilde{E}_{x,x+1} = k + 1/2, \qquad k \in \{-1, 0, +1\}. \tag{1.37}$$

Also in this case the model is gapped for any value of the mass, as shown in Fig. 1.11(b) (green dots). At a first sight, this situations looks very similar to the case of even n with no background field, when the possible spectrum of the electric field does not include zero, being still invariant under a sign change. However, the two cases are very different, since, as we will discuss in the next section, the $\mathbb{Z}_n$-model with even n and no background field, which is CP-invariant, still exhibits a phase transition.

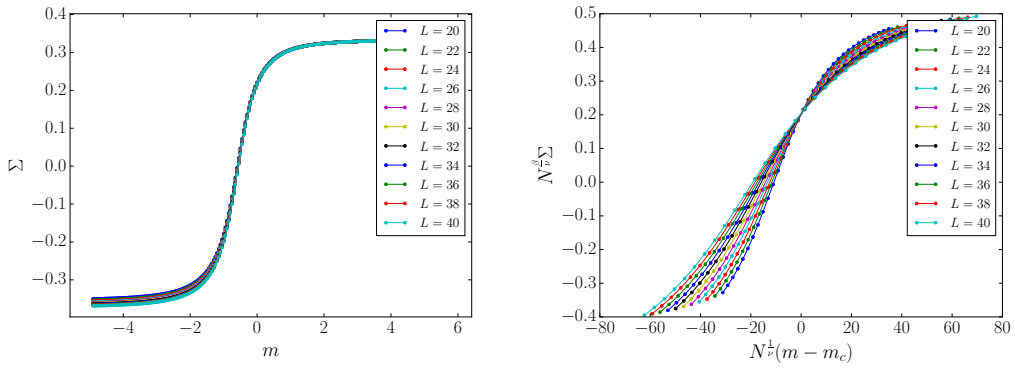

(a) (b)

Figure 1.10: $\mathbb{Z}_3$-model. (a) Observable Σ as a function of m in presence of a background electric field; (b) Non-universal scaling of the function $\lambda(x)$.

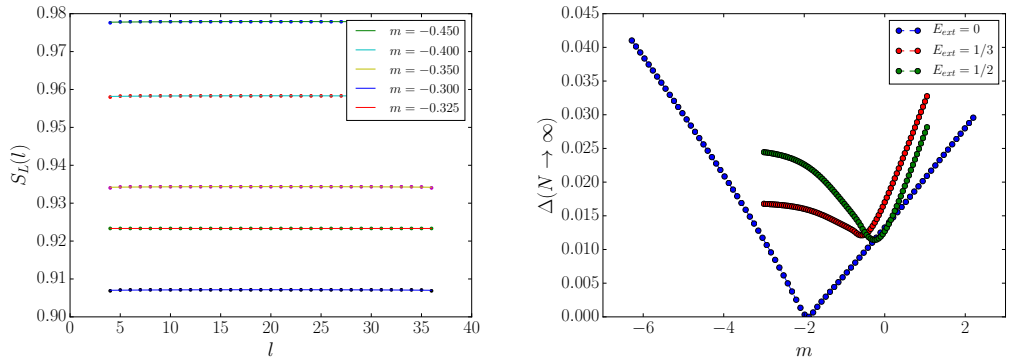

(a) (b)

Figure 1.11: $\mathbb{Z}_3$-model. (a) Entanglement entropy $S_L(l)$ of an interval of size l, in presence of a background electric field; (b) Gap Δ with (red and green dots) and without background field (blue dots).

1.5 Lattice $\mathbb{Z}_n$-QED model for other values of n

The analysis performed in the previous section for the $\mathbb{Z}_3$-model can be repeated for all values of n. In the following we will consider only the case with no background field. The dimension of the gauge-invariant Hilbert subspace for a chain with N sites is $2^N \times n$, increasing only linearly with n, since the electric field can now take the n values $-\sqrt{\frac{2\pi}{n}}\frac{n-1}{2}, \cdots, +\sqrt{\frac{2\pi}{n}}\frac{n-1}{2}$. Similarly to what was done for the $\mathbb{Z}_3$ case, we rescale the electric field as: $E_{x,x+1} = \sqrt{2\pi/n}\tilde{E}_{x,x+1}$ and study the Hamiltonian (1.20), with $g^2a^2 = g^2a/2 = 1$. One must consider odd and even n separately.

1.5.1 Odd n

As for the case $n = 3$ presented in the previous section, if n is odd we anticipate a phase transition from a phase where the ground state is the Dirac sea for large positive m, to a phase in which the ground state is a meson/antimeson state for large negative m. At $t = 0$, there is a first-order phase transition between these two states, at a critical mass $m_0^{(n)}$ that can be easily found by comparing the energy of these two states, given respectivley by $E_{\text{Dirac}}/L = -m$ and $E_{\text{meson}}/L = m + 2\pi/n$, thus yielding the critical value

$$m_0^{(n)} = -\pi/n. \tag{1.38}$$

Fot $t \neq 0$ we must resort to our DMRG code and perform an analysis identical to the one presented for the $\mathbb{Z}_3$-model, assuming again that the phase transition falls in the Ising universality class. As an example, in Fig. 1.12 we show the behaviour of the function λ of Eq. (1.26) for different system size in the $\mathbb{Z}_5$-model and for $t = 2\pi/5$, proving its universality in this case as well. We have performed an exhaustive analysis of the $\mathbb{Z}_5$- and $\mathbb{Z}_7$-models, obtaining the value of $m_c(t)$ as function of t in both cases, as summarized in the Appendix A and in Fig. 1.15.

We can now fit these data with the formula (1.32) to get an estimate of the coefficients α_n, β_n with $n = 5$ and 7. The numerical results are summarized in Table 1.1 and show an excellent agreement with the theoretically predicted value $m_0^{(n)} = -\pi/n$. Also, as for the $n = 3$ case, the coefficient of the linear term is much smaller than the one of the square-root term.

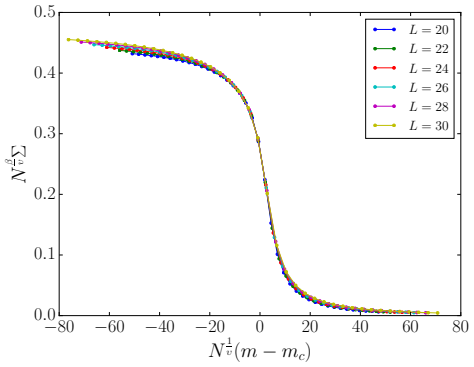

Figure 1.12: $\mathbb{Z}_5$-model. Universal scaling function $\lambda(x)$ close to the transition point ($t = 2\pi/5$).

1.5.2 Even n

Even-n models are different from odd-n ones since the electric field cannot take the value zero, still being CP-invariant. This means that we are working in a different super-selection sector corresponding to a different total charge at the boundary.

Let us first consider the case $n = 2$. This is a very small (in fact, the smallest non-trivial) value, and one may expect some peculiarities, due to the fact that the scaling arguments in Eqs. (1.18)-(1.19) do not apply. Actually, since the electric field Hamiltonian becomes trivial for $\phi = 0$, the presence of a phase transition only depends on the ratio of the coefficients of the hopping term and the mass term. Hence, the critical mass would be linear in t. The gauge-invariant Hilbert subspace for a pair of sites is 8-dimensional and a basis is shown in Fig. 1.13(a). The electric field can assume the two values $-\sqrt{\pi}/2, +\sqrt{\pi}/2$. The transition is from a phase where the ground state is the uniformly polarized vacuum, for large positive m, to a ground state in which the electric field has alternating signs on links, for large negative m. These states are shown in Fig. 1.13(b).

For $t = 0$ the energy per pair of these two states can be calculated exactly:

$$\frac{E_{\text{polarized}}}{L} = m + 2\left(\frac{\pi}{4}\right), \tag{1.39}$$

while

$$\frac{E_{\text{alternating}}}{L} = -m + 2\left(\frac{\pi}{2}\right). \tag{1.40}$$

Thus a first order phase transitions occurs at $m_0^{(2)} = 0$. For $t \neq 0$ we look for the phase transition by numerically calculating the observable Σ as

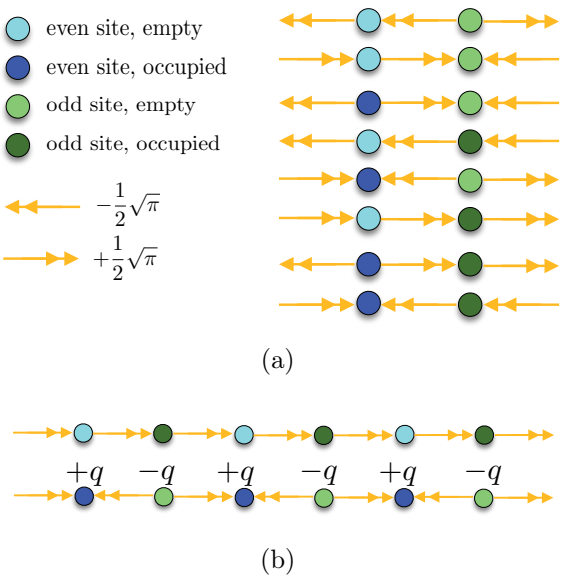

Figure 1.13: $\mathbb{Z}_2$-model. (a) Basis of the gauge-invariant Hilbert subspace; (b) ground states for large positive/negative m.

function of m and performing a finite-size scaling of the universal function that describes the order parameter. Fig. 1.14(a) displays Σ for $t = 2\pi/2 = \pi$, from which we can calculate the critical value $m_c = 0.016 \pm 0.025$, while Fig. 1.14(b) shows the corresponding universal function.

As for the odd-n case, we can numerically evaluate the critical value of the mass for different values of t and get the fit of the function $m_c(t)$ according to Eq. (1.32)

$$m_0^{(2)} = 0.004 \pm 0.001, \tag{1.41}$$
$$\alpha_2 = (8 \pm 5) \cdot 10^{-6}, \tag{1.42}$$
$$\beta_2 = 0.0149 \pm 0.0003. \tag{1.43}$$

From these values, we can see that *both* coefficients are very small, the dominant one being associated with the linear term. This is indeed one issue of the $\mathbb{Z}_2$-model that, as we will presently see, is not shared by higher n-models.

Taking into account this peculiarity and considering that we want to perform a large-n limit by using at least three different values of n both in the even and odd case, we have performed a similar analysis for the $\mathbb{Z}_4$, $\mathbb{Z}_6$ and $\mathbb{Z}_8$-models, whose results are summarized in the Appendix A. By fitting these data, we obtain the coefficients $m_0^{(n)}$, α_n and β_n of Eq. (1.32) as given in Table 1.1. As for the odd case, we find an excellent agreement of the

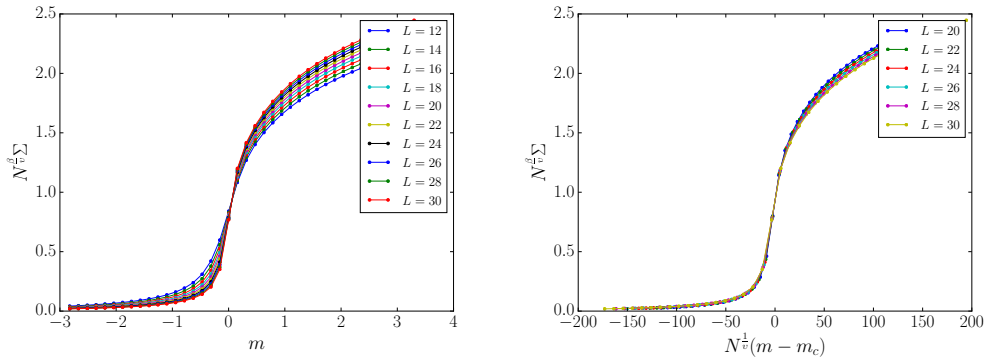

(a) (b)

Figure 1.14: $\mathbb{Z}_2$-model. (a) Order parameter Σ as function of m, for different L; (b) Scaling of $\lambda(x)$ close to the transition point.

n	$m_0^{(n)}$	α_n	β_n
2	0.004 ± 0.001	$(8 \pm 5) \cdot 10^{-6}$	0.0149 ± 0.0003
3	-1.0472 ± 0.0001	-0.603 ± 0.001	-0.02 ± 0.01
4	$(-3 \pm 1) \cdot 10^{-7}$	0.626 ± 0.005	0.0290 ± 0.0006
5	-0.628 ± 0.001	-0.494 ± 0.004	-0.015 ± 0.001
6	$(-7.2 \pm 0.1) \cdot 10^{-6}$	0.543 ± 0.005	0.026 ± 0.001
7	-0.448 ± 0.001	-0.435 ± 0.003	0.004 ± 0.001
8	$(1.8 \pm 0.1) \cdot 10^{-7}$	0.503 ± 0.004	0.022 ± 0.001

Table 1.1: Parameters of the numerical fit of the critical mass as a function of t, according to the formula $m_c(t) = m_0 + \alpha\sqrt{t} + \beta\, t$, for the various $\mathbb{Z}_n$-models with $n = 2 \div 8$.

numerical value for $m_0^{(n)}$ with the theoretically predicted value, $m_0 = 0$, and confirm that the dominant term is the one containing $\sqrt{t}$, as expected from Eq. (1.19).

1.6 Large-n limit

The values of $m_c(t)$ for $n = 2 \div 8$, are summarized in Table 1.1 and plotted in Fig. 1.15. Leaving aside the peculiar $n = 2$ case, these data clearly show that the critical mass actually shows a square-root dependence on t

$$m_c(t) = m_0^{(n)} + \alpha_n \sqrt{t}, \tag{1.44}$$

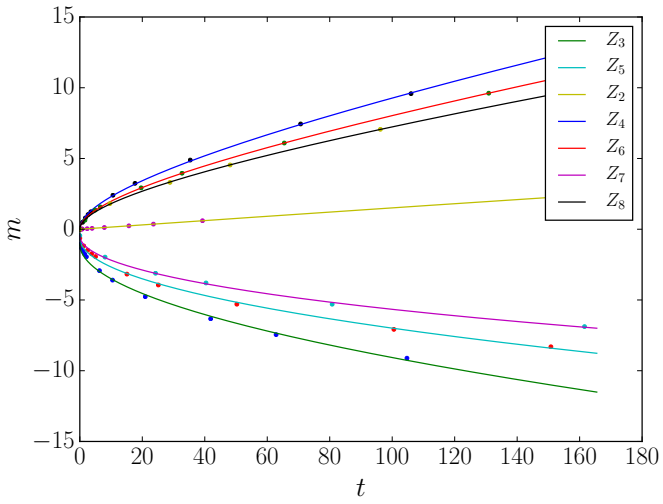

Figure 1.15: Plot of $m_c(t)$ for the various $\mathbb{Z}_n$-models. The points are the numerical data of Table 1.1 while the fits (continuous lines) yield $m_c(t) = m_0^{(n)} + \alpha_n \sqrt{t}$.

where, for any n, the critical mass at $t = 0$ can be calculated analytically (with $g^2 a = 2$) according to the formula

$$m_0^{(n)} = \begin{cases} -\frac{\pi}{n} & n \text{ odd} \\ 0 & n \text{ even} \end{cases}, \tag{1.45}$$

and vanishes in the large-n limit. The coefficients α_n can be read from the third column of Table 1.1. As we can see from Fig. 1.16, they obey the scaling

$$\alpha_n \simeq b + d/\sqrt{n}, \tag{1.46}$$

$$d = \begin{cases} -0.83 \pm 0.10 & n \text{ odd} \\ +0.84 \pm 0.17 & n \text{ even} \end{cases} \tag{1.47}$$

and $b = 0$ within numerical error in both cases. Except for the different sign, which is due to the fact that the even n-models do not admit a zero electric field, these two values are the same.

Thus, combining (1.23) and (1.46), we conclude that the continuous $U(1)$ theory exhibits a phase transition at the critical mass ($t = 1$)

$$m_c = \alpha = \lim_{n\to\infty} \alpha_n \sqrt{\frac{n}{2\pi}} = \frac{d}{\sqrt{2\pi}} \simeq \pm 0.33, \tag{1.48}$$

with the sign depending on the charge sector. This value is in very good agreement with the estimates $m_c/g = 0.33(2)$, obtained by using a lattice

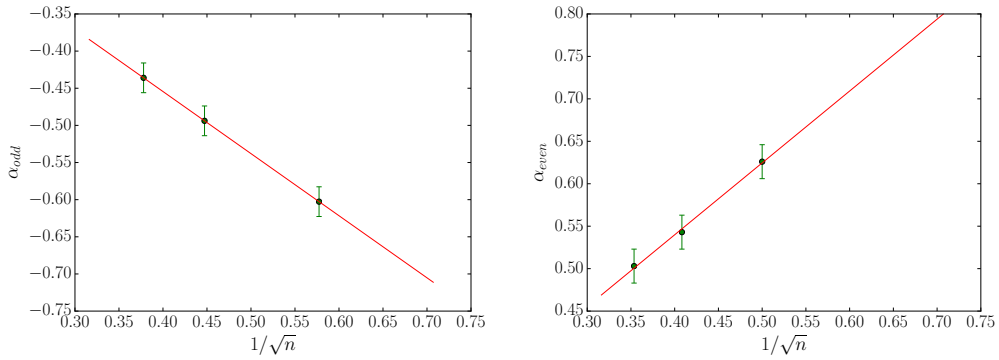

(a) (b)

Figure 1.16: Scaling with $1/\sqrt{n}$ of the coefficient α_n, for (a) $n = 3, 5, 7$ and (b) $n = 4, 6, 8$.

Hamiltonian approach [78], and $m_c/g = 0.3335(2)$, obtained by studying the truncated $\mathbb{Z}$-model (at most at the first five loop levels) [76].

1.7 Cold-atom simulator

The experimental implementation of the $\mathbb{Z}_n$ models is complicated by the presence of the correlated hopping terms, related to elementary processes in which the hopping of a fermion to a nearest-neighboring site is always associated to an action on the link between the sites, which amounts at increasing the electric field in the case of hopping to the left, and decreasing it if the fermion hops to the right. The accuracy of correlated hopping terms is vital for any cold-atomic simulator of the described theories, since it guarantees that, once the system starts in the physical subspace, in which Gauss' law is satisfied, it will not leave this subspace during the evolution. However, in a quantum simulation, in which matter and gauge fields are encoded in the external and (possibly) internal degrees of freedom of cold atoms, Gauss' law does not emerge as a natural property. Implementation of correlated hopping and enforcement of Gauss' law are therefore still open problems. We can identify two possible ways to simulate the gauge variables with cold atoms:

- Gauge variables can be encoded in the internal degrees of freedom of single atoms trapped at intermediate positions between each couple of adjacent sites. Hopping of a fermion induces transition towards different states according to the hopping direction. This realization require

a fine tuning of atomic transitions, as care must be taken in ensuring that all the allowed transition amplitudes between states with given fermion occupation numbers and electric field are equal. Moreover, the pure-gauge term requires that the energy levels of the intermediate atoms at $a \to \infty$ are quadratically spaced.

- Gauge variables can be encoded in an external, transverse degree of freedom. A possible interesting implementation arises from the possibility of trapping cold atoms in circular lattices, obtained by interaction with Laguerre-Gauss laser modes [79]. The scheme is represented in Figure 1.17, where the red spots represent the bottoms of potential wells in which the fermions are trapped, while the blue ones host one particle per link (statistics is immaterial), which can hop through neighboring sites of each circle (identified with eigenstates of the electric field), but cannot hop towards other links due to a large energy barrier. The equal amplitude of hopping between sites on the circle arises from a natural circular symmetry, and the pure-gauge term can be implemented by adding an external potential that properly varies along one of the transverse directions.

In both cases, the Gauss law could be implemented either by tailoring the transition amplitudes in order to enhance correlated hopping and suppress the forbidden terms, or by adding an energy or noise penalty to the states that violate Gauss' law [25, 39]. In the latter case, the desired interaction Hamiltonian can emerge as a higher-order effective dynamics [29].

1.8 Conclusions

We have investigated discrete $\mathbb{Z}_n$ models, that approximate QED in one dimension (Schwinger model). In these models the electric field can take a finite number of values, and one important common feature is the preservation of the unitarity of the comparator. Thus, we have put the large-n limit on a firm mathematical ground, adding novel rigorous results in the field of quantum simulations of gauge fields, that may soon find experimental verifications in cold-atomic systems.

In particular, we have unveiled the presence of phase transitions, whose features depend in an interesting way on whether n is even or odd. Although the details of these transitions depend on n, their universality class, as well as some of their main features, are n-independent, so that by looking at the large n limit, in which $\mathbb{Z}_n \to U(1)$, one can establish the presence of a phase transition for one-dimensional lattice QED, and extract crucial information.

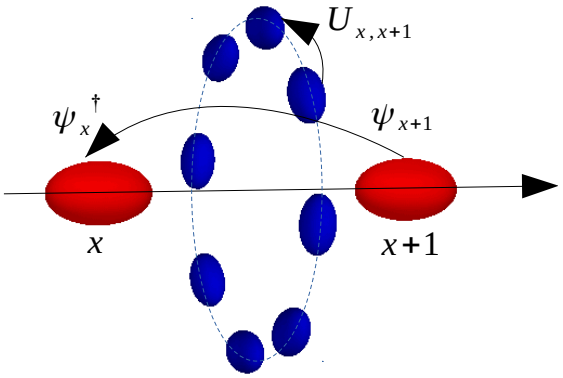

Figure 1.17: Scheme of the physical system on which the $\mathbb{Z}_n$ models can be implemented. Between each pair of neighboring fermion sites (red spots), a single particle is bound to hop on a circlular lattice. In order to reproduce the gauge Hamiltonian (1.5), hopping of fermions and of the particle on the link must be correlated.

A possible implementation of $\mathbb{Z}_n$ models on a cold-atom simulator, discussed in Section 1.7, relies on the identification of the discrete values taken by the electric field with some suitable additional degrees of freedom of the simulator [79]. A realization appears realistic and would be important to elucidate some important features of one-dimensional QED. Clearly, $1+1$-dimensional models have to be considered as toy-models with respect to the more realistic $3+1$-dimensional ones, but the possibility of using quantum simulators for the investigation of collective and non-perturbative features of gauge theories would enable us to shed new light on old problems, and provide new insights on crucial but still unsolved questions.

Chapter 2

Real Time Dynamics and Confinement in the $\mathbb{Z}_n$ Schwinger-Weyl QED

This chapter is organized as follows. In Sec. 2.1, we review the discretized version of the Schwinger model for 1+1 dimensional QED, that is accommodated on a one-dimensional lattice and endowed with a $\mathbb{Z}_n$ symmetry. As we showed in Chapter 1, this model exhibits a quantum phase transition at $m_c = -0.33$, belonging the Ising universality class. For $m > m_c$ the ground state of the model is in a confined phase, in which elementary excitations above the Dirac sea vacuum are of mesonic type. In Sec. 2.2, we set up the quench protocol to simulate spontaneous pair production, occurring in absence of an external electric field. We analyze this phenomenon by looking at the dynamical evolution of several physical quantities of interest, such as particle density, entanglement entropy, density correlation functions. We will see that, contrary to what is found in many other integrable and non-integrable models, the production of correlated particle/antiparticle pairs is strongly suppressed when we consider system parameters deep in the confined phase. In Sec. 2.3, we examine the phenomenon of pair production induced by the presence of an external electric field, finding an agreement between our simulations and old predictions by Schwinger [93] for the rate of pair production. Also, by examining the time evolution of entanglement, we conclude that the formation of mesonic excitations is stimulated by a dynamical effect due to the presence of the external field, of a different nature from the one emerging in the spontaneous case, examined in the Sec. 2.2. Finally, in Sec. 2.4, we will consider the real time evolution of a string excitation. We observe that the string breaks into mesons, thus giving rise to the so-called string-breaking mechanism, only when interactions are sufficiently weak. Vice versa, deep in the confined regime, the strings remain localized

and are apparently stable. We finally draw our conclusions in Section 2.5.

2.1 Brief review of the model

As we described in Sec. 1.1 and Sec. 1.2, the discretized Hamiltonian for the $\mathbb{Z}_n$ Schwinger-Weyl lattice model for 1+1 QED reads:

$$\begin{aligned} H &= -\sum_x (\psi^\dagger_{x+1} U_{x,x+1} \psi_x + h.c.) \\ &\quad + m \sum_x (-1)^x \psi^\dagger_x \psi_x + \frac{g^2}{2} \sum_x E^2_{x,x+1}, \end{aligned} \tag{2.1}$$

with x labelling the sites of a one-dimensional lattice of spacing $a = 1$, $1 \leq x \leq N$. Here, the one-component spinor is represented by the creation/annihilation operators $\psi^\dagger_x, \psi_x$, defined on each site x and with a staggered mass $(-1)^x m$, while the gauge fields are defined on the links $(x, x+1)$ of the lattice through the couple of operators, $E_{x,x+1}$ and the unitary comparator $U_{x,x+1}(\eta) = \mathrm{e}^{-\mathrm{i}\sqrt{2\pi/n} A_{x,x+1}}$ satisfying the commutation relations

$$[E_{x,x+1}, U_{y,y+1}] = \sqrt{2\pi/n}\, \delta_{xy}\,. \tag{2.2}$$

They act on a finite dimensional Hilbert space $\mathcal{H}_n$ defined on each link, which is generated by the orthonormal basis $\{|v_k\rangle\}_{0\leq k\leq n-1}$ on which the electric field operator is diagonal, with eigenvalues:

$$e_k = \sqrt{\frac{2\pi}{n}} \left(k - \frac{n-1}{2} + \phi \right) \ , \ 0 \leq k \leq n-1. \tag{2.3}$$

Here a non-zero value of the angle ϕ corresponds to adding a constant background field, which in turn corresponds to placing a charge at the boundary of the chain. The comparator operator U, instead, acts as a cyclic ladder operator:

$$U|v_k\rangle = |v_{k+1}\rangle \quad \text{for } k < n-1, \quad U|v_{n-1}\rangle = |v_0\rangle. \tag{2.4}$$

Also, Gauss law is implemented by requiring that the physical states belong to the subspace on which the following operator is zero:

$$G_x \equiv \psi^\dagger_x \psi_x + \frac{1}{2}[(-1)^x - 1] - (E_{x,x+1} - E_{x-1,x}) \approx 0. \tag{2.5}$$

Let us remark that, in one spatial dimension, Gauss law is a local constraint, whose implementation implies that the fermionic density is completely fixed (up to a contant) by the electric field, or viceversa. Thus, one

can proceed to integrate out the gauge field in order to write down a Hamiltonian $H_{\rm eff}$ only in terms of fermionic degrees of freedom. In doing so, one obtains a spin 1/2 model with long-range interactions [80]. On the contrary, one can eliminate the fermionic field and write down an effective Hamiltonian $H_{\rm eff}$ that contains only the variables $E_{x,x+1}$ and their conjugate ones $U_{x,x+1}$ [81, 82].

In Sec. 1.5, we analyzed the phase diagram of the discretized Hamiltonian (2.1) showing that, for any n, it exhibits a phase transition at a critical value of the mass m_c between a confined phase for $m > m_c$, in which the ground state is given by standard Dirac sea vacuum, and a deconfined one for $m < m_c$, in which the ground state is built up of meson/antimeson pairs.

In our representation, the Dirac sea vacuum is obtained by filling up all odd sites (negative mass fermions) and leaving the even ones (positive mass fermions) empty, as shown in the first line of Fig. 1.4. In this case, Gauss law (2.5) is satisfied if the electric field is zero on any link, a fact that we represent in the figure with an un-oriented link. A meson (antimeson) is obtained by acting on the Dirac sea by moving one fermion on an odd site to the right (to the left), as shown in the second (third) line of Fig. 1.4. Now Gauss law requires that the electric field on the connecting link is different from zero, and specifically equal to $+\sqrt{2\pi/n}$ $(-\sqrt{2\pi/n})$, a fact that we represent with an oriented link in the picture. In the fourth line of Fig. 1.4 we also show another gauge invariant configuration, representing a so-called string, in which the particle/antiparticle excitations building a meson have been moved further away from each other, with an electric field between them which is necessarily different from zero on all links.

The phase transition always belongs to the Ising universality class, with the confined/deconfined cases corresponding respectively to the paramagnetic/ferromagnetic phase of the Ising model in a transverse field. Here the quantum phase transition is driven by changing the value of the fermionic mass (instead of the external transverse magnetic field) and the role of the order parameter (the magnetization in the Ising case) is played by the mean value of the electric field operator:

$$\Sigma = \frac{1}{N} \sum_x \langle E_{x,x+1} \rangle \tag{2.6}$$

or equivalently by the mean fermionic density:

$$\rho = \frac{1}{N} \sum_x \langle \frac{1}{2} \left[1 - (-1)^x \right] + (-1)^x \psi_x^\dagger \psi_x \rangle \tag{2.7}$$

which, in the thermodynamic limit, are different from zero only in the deconfined phase. As we have shown in Sec. 1.6, the actual value of m_c depends

on the value of n that has been used to discretized the $U(1)$ gauge group but in the large-n limit it tends to $m_c \simeq -0.33$. In addition, as expected in the Ising model, close to the transition point the first excitation has conformal dimension $d = 2$, corresponding to a kink-like (or domain wall) solution.

Let us remark that while the Ising model in a transverse field is integrable for any value of the magnetic field, our model is more complicated and never integrable (except for the trivial case $g = 0$), because of the gauge coupling between fermionic matter and electric field. In the Ising case, integrability is lost and effective interactions between domain-wall excitations are present only if one adds the coupling with an external uniform longitudinal field [83], that we can also mimic in our model by introducing a background constant electric field.
The effects of such gauge-mediated interactions might be quite strong and will be studied by looking at real-time dynamical properties of our model in the next sections. The analysis will be performed by numerically studying the Hamiltonian (2.1) with a time-Dependent Density-Matrix Renormalization group (t-DMRG) algorithm, whose dynamical evolution is implemented through the Runge-Kutta method. More details about the precision of our algorithm are given in the Appendix B.

2.2 Pair production in absence of external field

In this section, we will examine the phenomenon of spontaneous pair production in the Schwinger model for $1 + 1$-dimensional QED, by simulating with our model the real-time dynamics of the Dirac sea vacuum, in absence of an external electric field. This effect has also been considered in other approaches [42–45] and it has also been experimentally analyzed in a small system (4 qubits) of trapped ions [36].

In order to test the stability of the Dirac vacuum with respect to spontaneous pair production, we prepare the system in the in the Dirac sea vacuum ground state and then study its evolution under the action of the Hamiltonian with different values of the coupling constants m, g, with either $m/g > m_c/g$ and $m/g < m_c/g$. For completeness, we will perform our analysis for all values of m, both positive and negative, but we stress that the Dirac vacuum we start from is a high excited state for $m < m_c$, while it is very closed to the true ground state in the confined phase and in particular when m is large and positive. In the language of spin systems, this would be analogue to prepare an Ising system in the ground state of the paramagnetic phase (say setting the external transverse field $h = 0$) and then suddenly quench the Hamiltonian to a different value of h, with $h < 1$ (staying inside the

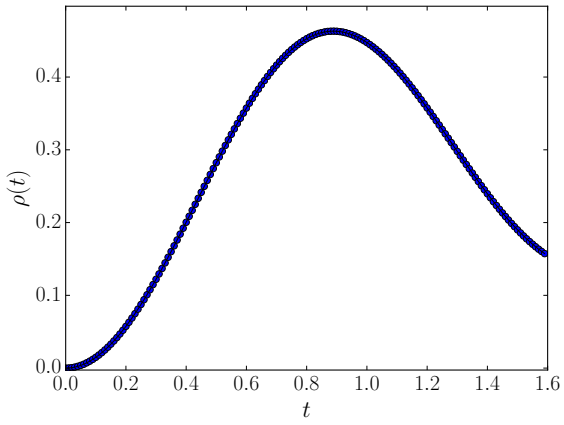

Figure 2.1: Time evolution of the Dirac sea vacuum for $N = 4$.

ferromagnetic phase) or with $h > 1$ f (quenching into the paramagnetic one), as it has been considered in [84].

Let us first consider the $\mathbb{Z}_3$ case. To test the evolution of the Dirac sea vacuum after the quench, we numerically calculate three different quantities.

1) The first quantity we consider is the *mean density of particles* evaluated on the evolved Dirac sea vacuum $|\Psi_0(t)\rangle$, with $|\Psi_0(t=0)\rangle = |0\rangle_{\text{Dirac}}$:

$$\rho(t) = \frac{1}{N}\sum_x \langle\Psi_0(t)|\frac{1}{2}\left[1-(-1)^x\right] + (-1)^x \psi_x^\dagger \psi_x |\Psi_0(t)\rangle. \tag{2.8}$$

This quantity is exactly zero on the Dirac sea vacuum and exactly 1 on the state with all mesons. Here $|\Psi_0(t)\rangle = U(t)|\Psi_0(t=0)\rangle$, with $U(t) = \exp(itH)$, and times are measured in units of $[energy^{-1}]$ having set $\hbar \equiv 1$.

To put our model to a first test, we calculate $\rho(t)$ for a chain with $N = 4$ sites, after a quench to $m = 0.5$ and $g = \sqrt{6/2\pi}$, which correspond to the parameters used in the eperimental set up of [36]. Figure 2.1 shows our result: the density starts form zero to go very close to the value $1/2$, corresponding to the formation of one meson. After that, recombination effects bring the value down again. This is in perfect agreement with the findings of [36].

More generally, we first set $g = \sqrt{6/2\pi}$ and quench to different values of m. The temporal evolution of ρ is shown in Fig. 2.2 for (a) large positive values of the mass ($m \geq 1.0$), (b) large negative values of the mass ($m \leq -1.0$), (c) small absolute values of the mass ($-1.0 < m < 1.0$). We clearly see that for very large values of the mass (both positive and negative), $\rho(t)$ oscillates periodically between zero and a rather small value, due to a small rate of pair production and recombination effects: the Dirac sea vacuum

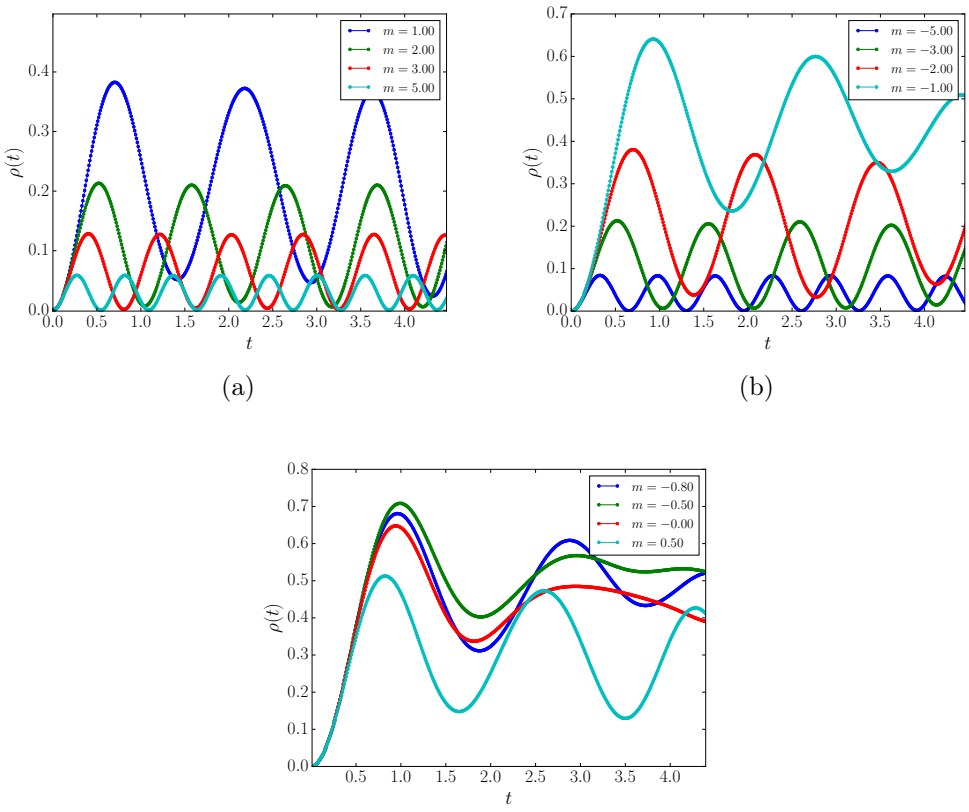

Figure 2.2: $\mathbb{Z}_3$-model. Time evolution of the Dirac sea vacuum after a quench to different values of large positive mass, at fixed $g = \sqrt{6/2\pi}$ and $N = 40$: (a) $m \geq 1.0$, (b) $m \leq -1.0$, (c) $-1.0 < m < 1.0$.

is essentially stable. On the contrary, for smaller values of $|m|$, the density increases rapidly up to values close to 1 (corresponding to the mesonic ground state), to start then oscillating because of recombination effects, but now around a non-zero large value, showing that the Dirac sea vacuum is unstable. This is particularly evident for quenches to values of the mass close to the critical one, $m_c \sim -0.33$.

Let us analyse better the curves of Fig. 2.2 as a function of m. Figure 2.3(a) shows the maximum value of $\rho(t)$ extrapolated form the first peak: it is clear that the highest pair production occurs close to the phase transition. In Fig. 2.3(b) we show instead the period T of the oscillations, for $m > m_c$. We see that the data are very well described by the continuous line, which corresponds to a best fit with respect to a function of the form: $T(m) \propto$

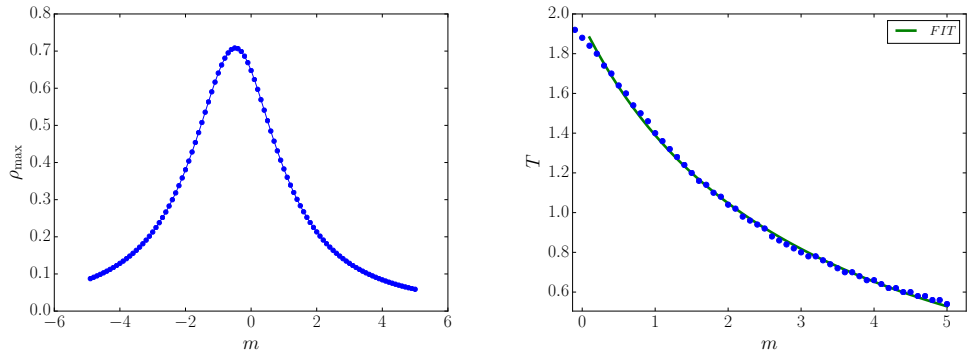

(a) (b)

Figure 2.3: Analysis of the curves of Fig. 2.2. (a) Values of the first peak as function of m. (b) Period of the oscillations, for $m > m_c$.

$1/(am + b)$, for constant a, b. This form is what is expected from a first-order approximation, sccording to which the period might be evaluated as the inverse of the energy difference between the energy of the Dirac sea ($E_{Dirac}/N = -m$) and the energy of the mesonic state ($E_{mesonic}/N = m + g^2/2$).

In the Appendix B, we give details on the finite size scaling analysis we performed. To summarize our results we show in Fig. 2.4 the contour plot of the density $\rho_\infty(t)$ extrapolated for $N \to \infty$, in the whole range of the quenched mass $m \in [-5, +5]$. We can conclude that the Dirac sea vacuum is unstable for values of the mass close to the critical value m_c, whereas pair production is strongly suppressed for large values of m.

2) The second quantity we calculated is the time evolution of half-chain entanglement entropy:

$$S_{N/2}(t) = -\mathrm{Tr_A}\left\{\rho_A(t) log_2\left[\rho_A(t)\right]\right\} \tag{2.9}$$

where the chain has been partitioned in the two subsytems A, B consisting of the first/last $N/2$ sites of the chain. The initial Dirac sea vacuum is separable and hence $S_{N/2}(t = 0) = 0$.

Fig. 2.5(a) and Fig. 2.5(b) show some examples of $S_{N/2}(t)$ for large values of m. We see that the entanglement entropy shows an oscillatory behaviour, reaching a maximum at small values (e.g. $S^{max}_{N/2} \sim 0.5$ for $m = 2.0$ or $m = -3.0$) and again $g = \sqrt{6/2\pi}$. The period of these oscillations increase as m decreases and, at the same time, the entropy reaches higher values, of the order of unity or more for small m, as it can be seen from Fig. 2.5(c). For

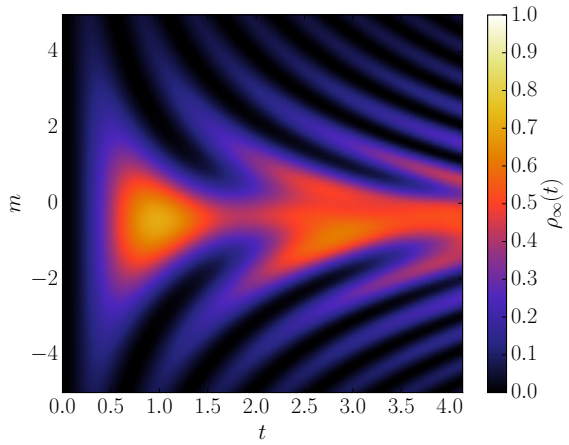

Figure 2.4: Contour plot of $\rho_\infty(t)$ in the whole range of the quenched mass $m \in [-5, +5]$.

m close to the critical value m_c (see for example the data for $m = 0.0, -0.5$), the entropy increases much faster and we see a monotonic behaviour. Thus, we can conclude that when the phenomenon of pair production is dominant, the quantum correlations of the two parts of the chain grow bigger due to the fact that the entangled particle/antiparticle pairs that are spontaneously created spread along the chain.
This effect is much studied in free fermionic [85] and/or integrable models [86], where entanglement can be shown to increase linearly with time, at least as long as one can assume a maximum speed of propagation (the Lieb-Robinson bound [87]). Not considering disorder and/or long-range interactions, this behaviour has also been confirmed in several integrable models [86]. In [84], the time evolution of the half-chain entanglement entropy has been studied for a non-integrable model, namely the Ising model with both a transverse and a longitudinal field, which admits a confined phase [83], showing that the growth of the entanglement entropy is strongly reduced for quenches within the confined (ferromagnetic) phase. This is exactly [88] what we observe in our model. The black dashed line in Fig. 2.5(c) shows the linear behaviour of the entanglement entropy in the free case. For small but non-zero values of m, we can clearly recognize a slow down of the growth the entanglement entropy, which is now well described by a logarithm growth in time: $S_{N/2}(t) \propto \log t$. When the interaction is strong and we are deep in the confined phase, the system seems not to evolve toward an equilibrium situation, at least in the time scale to which we can perform our simulations. Indeed entropy is strongly suppressed and shows revivals, similarly

to what happens in those models where the quantum scar phenomenon appears [89–91].

3) At a last indicator, we consider the time evolution of connected correlation functions

$$G_0(j - L/2)(t) = \langle n_{L/2}(t) n_j(t) \rangle - \langle n_{L/2}(t) \rangle \langle n_j(t) \rangle \tag{2.10}$$

which are shown in Fig. 2.6. For small values of m, the connected correlation functions show the typical light-cone spreading of a conformal or integrable theory, as predicted in [92]. But as we enter in the intermidiate and strong coupling region, we observe a localization effect and an oscillatory behaviour, indicating that particle/antiparticles pairs do not spread and recombine, in a recursive manner. Similar behaviours has been observed in other models [80, 84].

2.3 Pair production in an external field

In the context of particle physics, pair production is often studied in presence of an external electric field, from which the pair production rate is expected to depend. For the Shchwinger model, the value E_c of the external electric field for which one should observe a maximum in the e^+e^- production rate is given by $E_c = m^2/g \approx 1.32 \times 10^{18}\ V/m$ [93] (in natural units $c = \hbar = 1$), but this effect has never been observed experimentally since it is still out of the range of even the most powerful lasers. In $1+1$ dimensions, a formula for the production rate has been proposed in [94, 95]:

$$\dot{\rho} = \frac{eE_0}{2\pi} \exp\left(-\frac{\pi m^2}{eE_0}\right) = \frac{m^2}{2\pi} \epsilon \exp\left(-\frac{\pi}{\epsilon}\right) \tag{2.11}$$

where $\dot{\rho}$ represents the time derivative of the total density of the chain in the infinite length limit, while $\epsilon = E_0/E_c$, E_0 being the value of the external field. This formula predicts that the production rate increases linearly for large values of ϵ and it is exponentially suppressed for $\epsilon \ll 1$.

This formula can be checked in our simulations. We start by considering the $\mathbb{Z}_3$-model. We choose values of m, g for which Dirac sea vacuum resulted stable, according to previous analysis. At $t = 0$ we apply a constant uniform magnetic field E_0 along the whole chain and run the simulation to obtain $\rho(t)$ for the corresponding value of $\epsilon = E_0/E_c$, with $E_c = m^2/g$. Fig. 2.7(a) shows the results of our simulations for the case $m = 4.5$ and $g = \sqrt{6/(2\pi)}$. We observe that, for very small values of ϵ, the vacuum is stable, but for

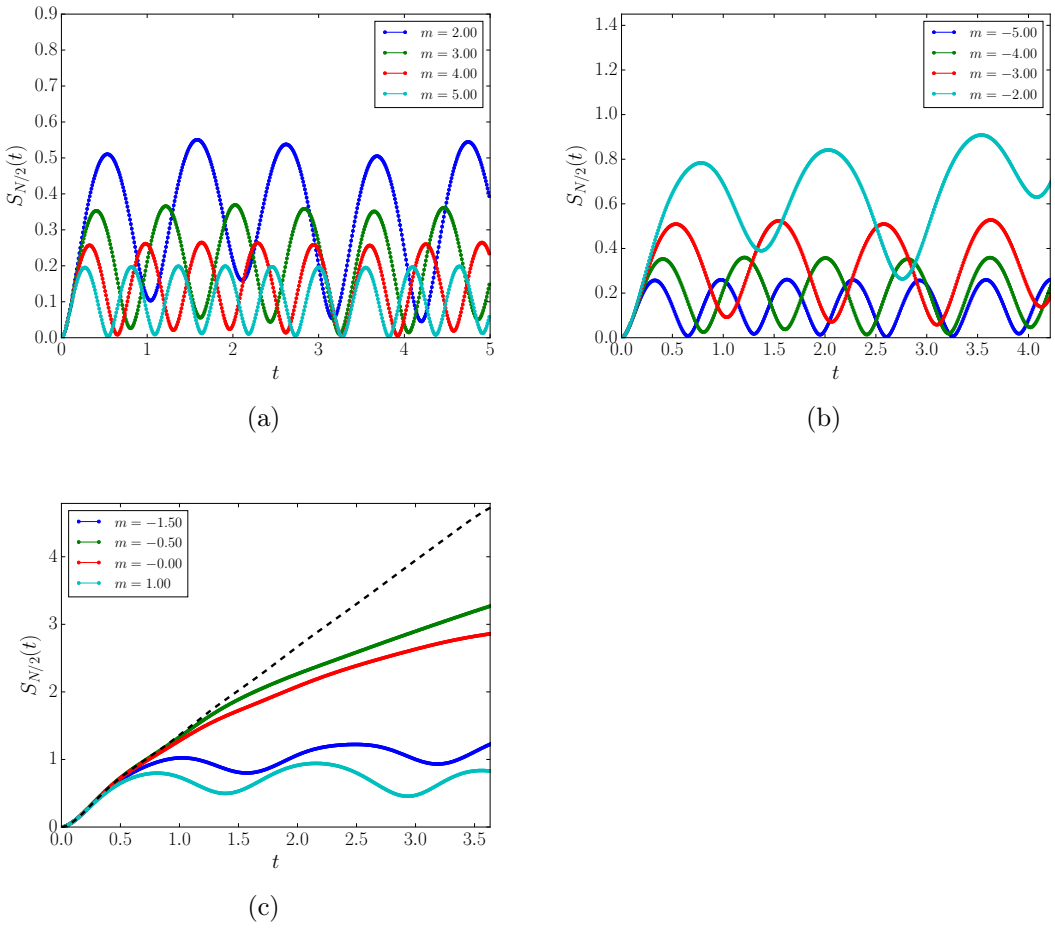

Figure 2.5: $\mathbb{Z}_3$-model. Time evolution of the half-chain entanglement $S_{N/2}(t)$ for: (a) $m \geq 2.0$; (b) $m \leq -2.0$; (c) $-2.0 < m < 2.0$. For all the three cases $g = \sqrt{6/2\pi}$. The black dashed line shows the free fermion case $m = 0, g = 0$.

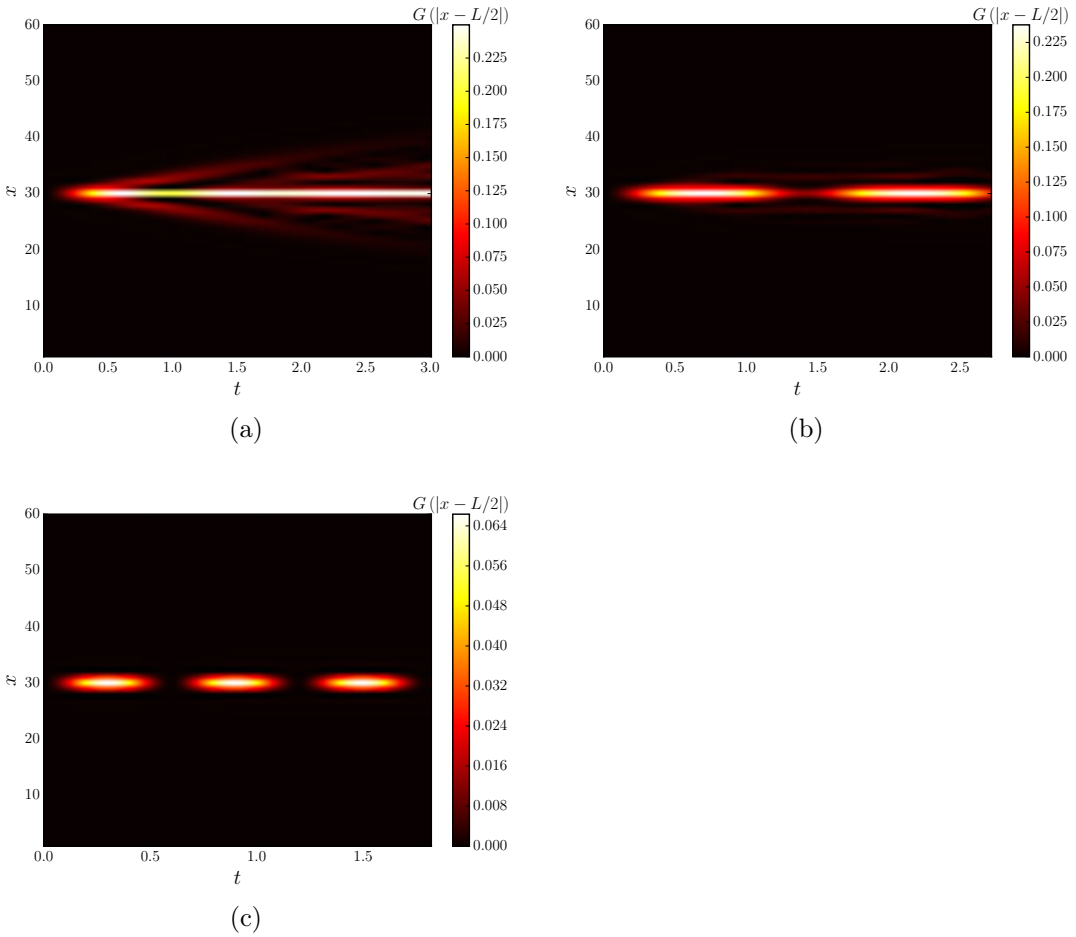

Figure 2.6: $\mathbb{Z}_3$-model. Contour plot of $G_0(j - L/2)$ for $g = \sqrt{6/2\pi}$ and (a) $m = -0.5$ (b) $m = 1.0$, (c) $m = 4.5$

.

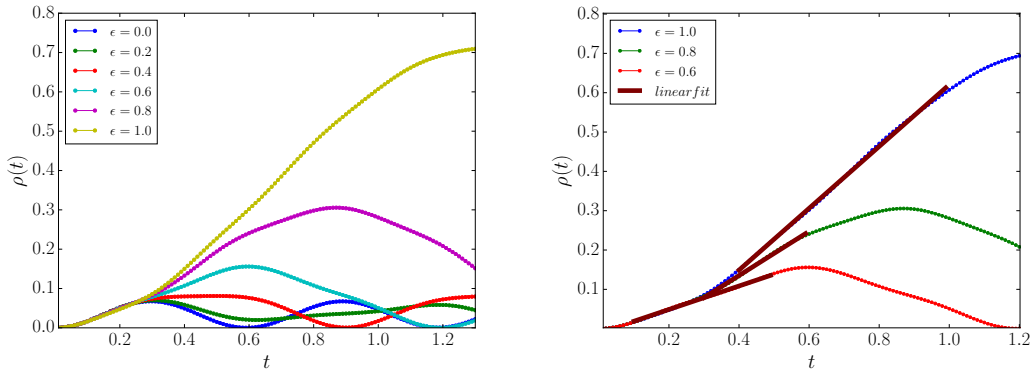

(a) (b)

Figure 2.7: $\mathbb{Z}_3$-model. (a) Particle density $\rho(t)$ as function of time for different values of $\epsilon = E_0/E_c$. We have set: $N = 50$, $m = 4.5$ and $g = \sqrt{6/(2\pi)}$. (b) Linear fit for small values of ϵ to obtain $\dot{\rho}$ and verify eq. (2.11).

some small oscillations. As we increase ϵ we start seeing a linear regime, followed by a saturation effect, as predicted by eq. (2.11). Fig. 2.7(b) shows the range in which we performed the linear fit in order to evaluate $\dot{\rho}$ and verify eq. (2.11).

Since we expect strong size effects, we have repeat the simulations for various values of N, namely $N = 50, 60, 70, 80, 90$. Also, to check the large-n limit to see if we can reasonably approximate the $U(1)$ limit with our model, we have preformed an analogous analysis for the $\mathbb{Z}_5$ and the $\mathbb{Z}_7$ models. Our results, which are summarized in the Appendix B, show that the the continuum limit is better and better approximated.

Finally, in order to get some additional insight on the phenomenon, we have calculated the time evolution of the half-chain entropy, for different values of the external magnetic field. A typical behaviour is shown in Fig. 2.8, which shows the data for $m = 4.5$ and $g = \sqrt{6/(2\pi)}$. We notice that the entropy always presents an oscillatory behaviour with not too large maximum values. More interestingly, we observe that an increase of the external field -which results in a rapid increase in particle pair production as shown in Fig. 2.7(a)- does not contribute at all to an increase of the entanglement and to its spreading. Thus, we can postulate that the mechanism that dictates the particle/antiparticle pair production is different with or without the external field: in the former case pair formation is dictated by a rearranging of the charges present in the system as an effect of the external field, while in the latter entangled quark/antiquark pairs are spontaneously created out of the

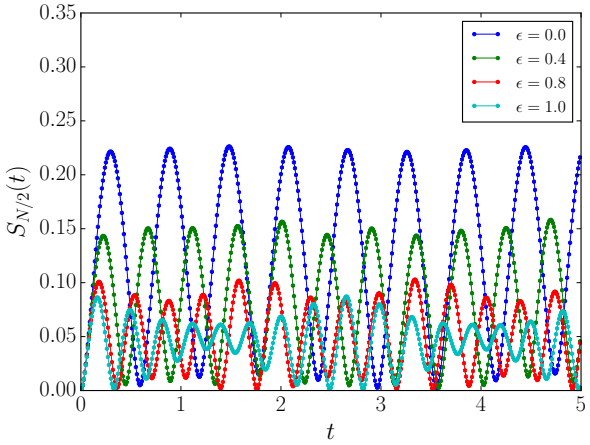

Figure 2.8: $\mathbb{Z}_3$-model. Half-chain entanglement $S_{N/2}(t)$ for different values of the external fields. We assume $m = 4.5$ and $g = \sqrt{6/(2\pi)}$

Dirac sea.

2.4 The string breaking mechanism

As recalled in the Introduction, the string breaking mechanism is a very interesting phenomena that is expected to occur in theories, such as $1+1$-QED and $3+1$-QCD, that admit confined phases, but it is also very hard to prove either analytically or numerically since its effects are mainly dynamical.
In our approach we are able to investigate it, since we can simulate the real-time dynamics of a generic initial state, which is then let to evolve with the discretized Hamiltonian (2.1). In particular we prepare our system in the string-excitation state shown in Fig. 1.4 (fourth line), where a particle/antiparticle couple at a distance l has been created over the Dirac sea vacuum thus giving rise to a non-zero string of the electric field in between. In the following we will consider the $\mathbb{Z}_3$ model and a chain of length $N = 80$. We initialize our system in a string put at the center of the chain: the particle/antiparticle pair is put at a distance equal to 20 lattice sites so that the electric field is different from zero (and equal to $+\sqrt{2\pi/3}$) only on the 19 central links of chain. The evolution of this state is followed by looking at the value of the electric field $E_{x,x+1}(t)$ on each link. Clearly, this process is also effected by the instability of the Dirac sea vacuum that we studied in the previous sections. We report the analysis of the real time dynamics of such a string for three different values of (m, g) specifically corresponding

to (a) weak interactions ($m = 0.1, g = 0.1$) , (b) intermediate interactions ($m = 0.3, g = 0.8$), strong interactions ($m = 3.0, g = 1.4$). Clearly, the total evolution is also affected by the instability of the Dirac sea vacuum that we studied in the previous sections. Thus, to improve the interpretation of our numerical results, we subtract from $E_{x,x+1}(t)$ the value of the electric field that would be obtained starting from the Dirac sea vacuum for the same values of (m, g). The corrected data are shown in Fig. 2.9, which clearly show three different situations:
a) for weak interactions, the string starts to spread and breaks into particle/antiparticle pairs (mesons) that, after a short time in which one can notice a rich process of pair production and recombination, stabilize in a configuration with two mesons localized at the edges of the string; the two mesons are deconfined, since they move away one from the other at constant speed;
b) for intermediate interactions, instead, the string does not spread; still it breaks into particle/antiparticle pairs (mesons) that, as in the previous case, quickly stabilize in a configuration where we can still distinguish two mesons localized at the edges of the string; but now the two mesons are confined, since they are kept at fixed distance one from the other;
c) for strong interactions, the string is completely stable: it does not spread and it does not break into mesons.

The simulations which are reported in Fig. 2.9 can be repeated for any couple of values (m, g). Our results are summarized in Fig. 2.10, where we show the contour plot of the large-t (namely $t = 4.0$ in our units) total value of the electric field at the center of the chain, defined as the sum of the electric field on the 12 central links, as a function of the coupling constants (m, g). The two white level curves correspond to a 10% (dotted line) and to a 50% (solid line) of the initial value, respectively. From this picture, the three regimes described above are clearly identified: (a) the lighter and central part of the diagram corresponds to the breaking of the string into two deconfined mesons; (b) the reddish part of the diagram to the breaking of the string into two confined mesons; (c) the darker part to a stable string configuration.

It is interesting to examine the string breaking phenomenon by looking also at the time evolution of the half-chain entanglement entropy, for different values of (m, g). Fig. 2.11 shows the behaviour of $S_{N/2}$ evaluated on the time evolution of the string state by first keeping $g = 0.1$ fixed and let m vary (a) within positive values, (b) within negative values and then (c) keeping $m = 0.1$ fixed and let g vary. These graphs confirm what found by looking at the real time dynamics of the electric field configuration, showing a growth of

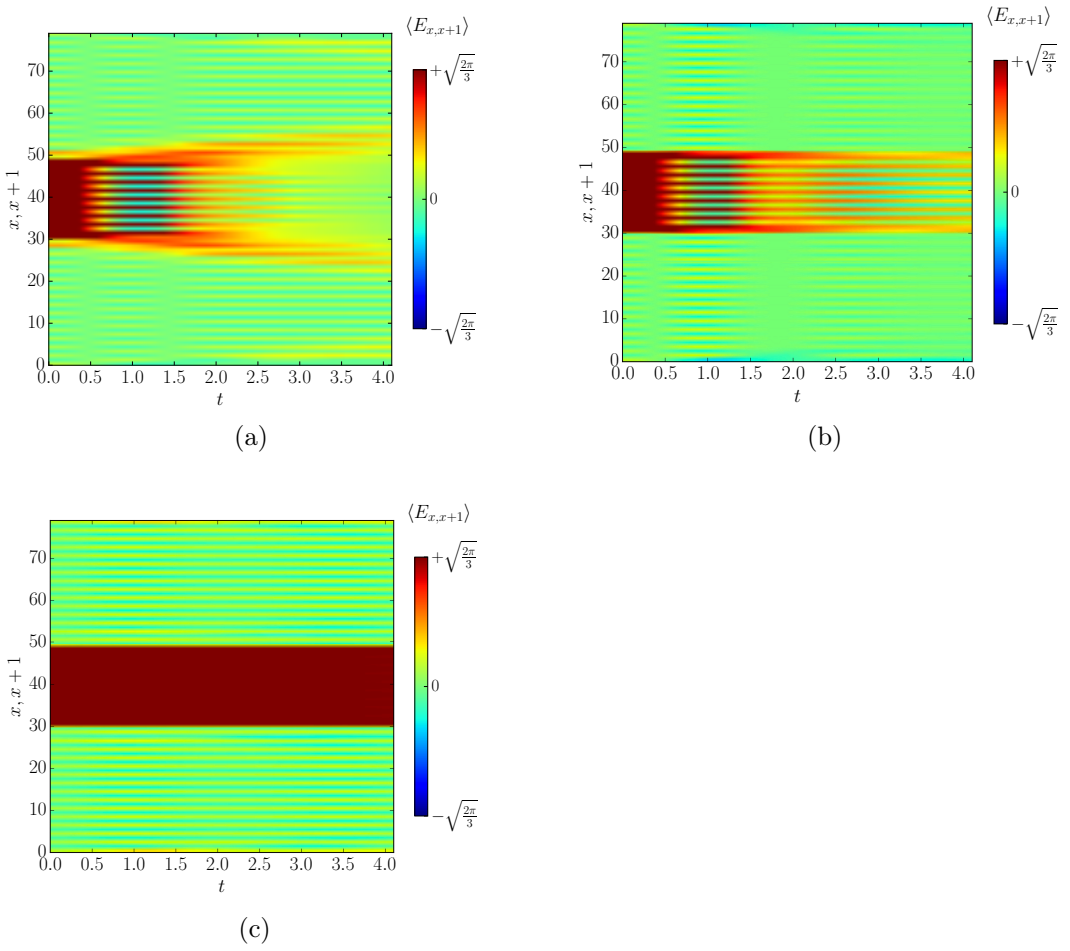

Figure 2.9: $\mathbb{Z}_3$-model. Real-time dynamic of a string: evolution of the electric field on the links, corrected with spontaneous pair production, for: (a) $m = 0.1, g = 0.1$, (b) $m = 0.3, g = 0.8$, (c) $m = 3.0, g = 1.42$.

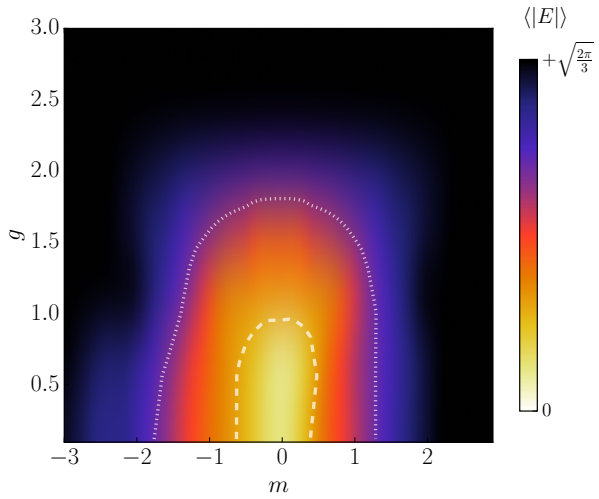

Figure 2.10: Contour plot in the $m - g$-plane of the asymptotic total value of the electric field at the center of the chain. The two white level curves correspond respectively to a 10% (dotted line) and to a 50% (solid line) of the initial value.

entanglement entropy which is linear for weak interactions (small m and/or small g), sublinear for intermediate interactions and suppressed (with small oscillations) in the strong coupling regime.

2.5 Conclusions

We have investigated out-of-equilibrium properties of $(1 + 1)$-dimensional QED, approximated via a $\mathbb{Z}_n$ Schwinger model. By means of simulations of the stability of the Dirac vacuum with respect to particle/antiparticle pair production and of the string breaking mechanism, we have studied the effect of confinement on the real time dynamics of the model.

We have found that confinement has a relevant effect on the dynamical properties of the model, resulting in oscillatory behaviours and lack of thermalization for pair production as well as in a total suppression of the breaking and spreading of string excitations, with a perfect localization of the latter.

Let us notice that such a reduction of entanglement and slow-down of dynamics have been observed in other systems. This is the case of not only of model with long-range interactions [96] but also of the Ising and Potts models with both a transverse and a longitudinal magnetic fields [84, 97]. A similar behaviour has also be seen in constrained models which exhibit quantum scar states [90, 91] or for spin-1/2 chain Hamiltonians that can be

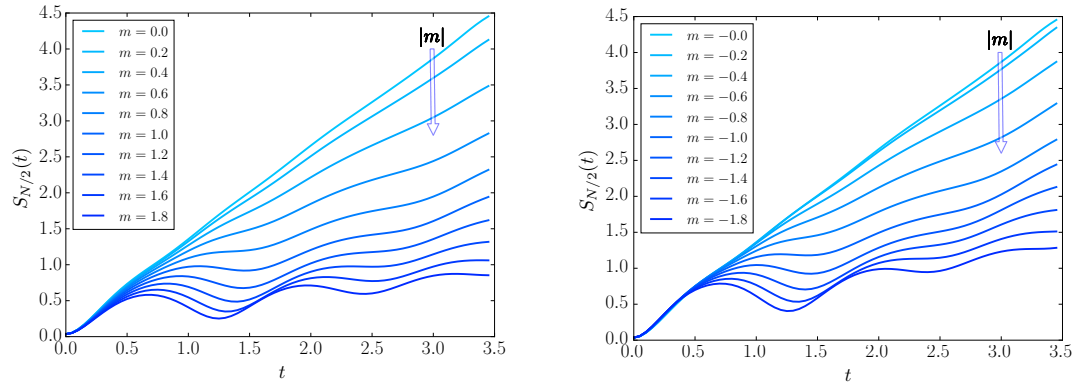

Figure 2.11: (a) $\mathbb{Z}_3$-model. Time evolution of the half-chain entropy $S_{N/2}(t)$ for: (a) $g = 0.1$ and different positive values of m, (b) $g = 0.1$ and different negative values of m, (c) $m = 0.1$ and different values of g.

derived from Abelian gauge models in the quantum link approach [80]. It is interesting to notice that, in the two latter cases, the physical states of the system under consideration are constrained to lie in a restricted subspace of the total Hilbert space, a fact that it is shared by our model where the role of Gauss law constraint is crucial. This is also at the heart of the recent idea to experimentally implement these Hamiltonian with Rydberg atom systems in the Rydberg-blockade regime [98].

Chapter 3

Symmetry-protected topological phases in lattice gauge theories: Topological QED_2

This chapter is organized as follows. In Sec. 3.1, we start by reviewing the properties of the continuum massive Schwinger model and its standard lattice discretization, and use it to introduce the alternative discretization that substitutes the staggered mass by a topological mass that leads to the *topological Schwinger model*. In Sec. 3.2, we describe the continuum limit of this model, topological QED_2, and introduce a bosonization formalism that gives a neat understanding of the interplay of symmetry-protected topological phases (SPT) and lattice gauge theories (LGT) features. In particular, we show that the underlying topology promotes the so-called vacuum θ angle, a constant parameter in the standard Schwinger model, into a dynamical quantum-mechanical operator that yields a notoriously different phase diagram. In Sec. 3.3, we test these analytical predictions using the numerical Density-Matrix Renormalization Group (DMRG) for a discrete version of this topological Abelian LGT. We discuss various signatures that give compelling evidence of a strongly-correlated SPT phase, such as the existence of many-body edge states and degeneracies of the entanglement spectrum. Moreover, we present finite-size scaling of two order parameters and block entanglement entropies, providing accurate estimates of the critical lines, and their universality classes. We finally draw our conclusions in Section 3.4.

3.1 Topological Schwinger model

In this section, we start by reviewing the continuum massive Schwinger model [68,116], describing the interaction of a massive Dirac fermion interact-

ing with the electromagnetic field in (1+1) dimensions. We first discuss the standard discretization à la Kogut-Susskind [11], where the gauge field, defined on the links of a one-dimensional chain, dresses the hopping of fermions between neighboring lattice sites, and an alternating on-site potential leads to a finite fermion mass. After reviewing some of the main features of this model, which shares key features with higher-dimensional non-Abelian LGTs, we introduce a simple modification of the lattice discretization that leads to the model of interest of this chapter: the *topological Schwinger model*. Essentially, we substitute the staggered mass by a topological mass that can stabilize SPT phases, and yields a neat minimal scenario to study strong-correlation effects brought up by the interaction with the gauge field.

We start by describing the continuum quantum field theory of a spinor field $\Psi(x) = (\psi_{\mathrm{u}}(x), \psi_{\mathrm{d}}(x))^{\mathrm{t}}$ describing the relativistic Dirac fermions of mass m, and a gauge field $A^{\mu}(x)$ describing the electromagnetic field. In a (1+1)-dimensional Minkowski spacetime with coordinates x^{μ}, $\mu \in \{0, 1\}$ (i.e. $x = (t, \mathrm{x})$), and after setting $\hbar = c = 1$, the Lagrangian density that dictates the dynamics of the fermionic and gauge fields is given by the so-called massive Schwinger model

$$\mathcal{L}_{m\mathrm{S}} = \overline{\Psi}(\mathrm{i}\gamma^{\mu}(\partial_{\mu} + \mathrm{i}gA_{\mu}) - m)\Psi - \tfrac{1}{4}F^{\mu\nu}F_{\mu\nu}, \tag{3.1}$$

where $\partial_{\mu} = \partial/\partial x^{\mu}$, $A_{\mu}(x) = \eta_{\mu\nu}A^{\nu}(x)$, and we use the repeated-indexes summation criterion with Minkowski's metric $\eta = \mathrm{diag}(1, -1)$. In the expression above, we have introduced the Dirac matrices satisfying the anti-commutation relations $\{\gamma^{\mu}, \gamma^{\nu}\} = 2\eta^{\mu\nu}$, which can be represented in terms of standard Pauli matrices in (1+1) dimensions. Here, we have also introduced $\overline{\Psi}(x) = \Psi^{\dagger}(x)\gamma^{0}$, and the (bare) coupling g of the fermion current to the gauge field with electromagnetic field tensor $F_{\mu\nu} = \partial_{\mu}A_{\nu} - \partial_{\nu}A_{\mu}$. With this notation, the fields have the classical mass (energy) dimensions $d_{\psi} = 1/2$ and $d_{A_{\mu}} = 0$, while the mass and gauge coupling have $d_m = d_g = 1$.

The Schwinger model is the simplest tractable QFT that captures some of the most significant non-perturbative effects displayed by non-Abelian gauge theories in higher dimensions. In the massless limit $m = 0$, it was solved exactly by J. Schwinger [101], who showed that the spectrum can be described by non-interacting bosons with a mass proportional to the coupling strength (i.e. fermion-antifermion pairs are trapped in such a way that single-fermion excitations do not appear in the spectrum [116]). Additionally, it yields a neat scenario where to understand the consequences of the chiral anomaly [69], and the origin of the degeneracy with respect to a background electric field leading to the so-called vacuum θ angle [60, 102]. In the massive regime $m \neq 0$, the Schwinger model can be used to understand charge shielding via

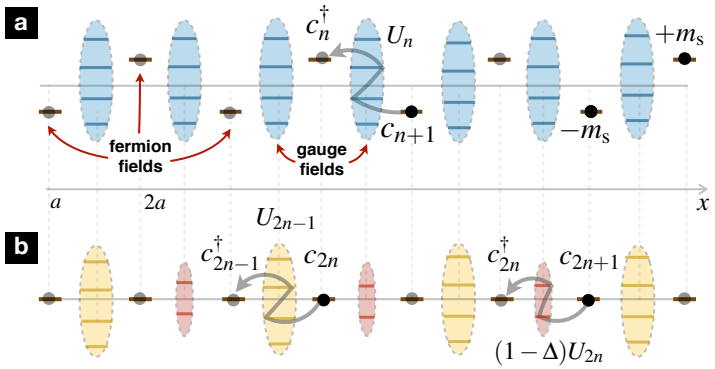

Figure 3.1: Discretizations for standard and topological QED$_2$: (a) Staggered-fermion approach to the massive Schwinger model. The relativistic Dirac field is discretized into spinless lattice fermions subjected to a staggered on-site energy $\pm m_s$, which are represented by filled/empty circles at sites of a 1D chain with alternating heights. On the other hand, the gauge field is discretized into rotor-angle operators that live on the links, which are represented by shaded ellipses with various levels representing the electric flux eigenbasis. The gauge-invariant tunneling $c_n^\dagger U_n c_{n+1}$ involves the tunneling of neighboring fermions, dressed by a local excitation of the gauge field in the electric-flux basis $U_n|\ell\rangle = |\ell+1\rangle$, which is represented by the zig-zag grey arrow joining two neighboring fermion sites, via an excitation of the link electric-flux level. (b) Dimerized-tunneling approach to the topological Schwinger model. The previous staggered mass is substituted by a gauge-invariant tunneling with alternating strengths $(1-\delta_n)c_n^\dagger U_n c_{n+1}$, where $\delta_n = 0, \Delta$ for even/odd sites. This dimerization of the tunneling matrix elements is represented by alternating big/small ellipses at the odd/even links.

the string tension between two separate probe charges (i.e. screening of the long-range Coulomb force between static charges) [116], and string-breaking phenomena as the distance between the charges is increased beyond a certain value [103]. Moreover, the degeneracy with respect to the θ angle is lifted, and one finds that for $\theta = \pi$ there is a continuous quantum phase transition between the confined phase and a symmetry-broken phase with a fermion condensate [68].

There are various numerical methods to unveil this non-perturbative phenomenology, serving as a benchmark for theoretical approaches that could be generalized to other situations of interest (e.g. quantum chromodynamics). These methods typically rely on a discretization of the fields on a lattice, and we shall focus on the Kogut-Susskind approach [11]. Here, only the spatial coordinates are discretized into the sites of a chain $\Lambda_\ell = \{\mathrm{x} : \mathrm{x}/a \in \mathbb{Z}_{N_s}\}$, where a is the lattice spacing, and N_s is the number of lattice sites. By writing $\mathrm{x} = na$ for $n \in \mathbb{Z}_{N_s}$, the matter sector of Dirac fermions can

be represented by the so-called staggered fermions defined on the lattice sites $\Psi(\mathrm{x}), \overline{\Psi}(\mathrm{x}) \to c_n, c_n^\dagger$, such that $\{c_n, c_m^\dagger\} = \delta_{n,m}/a$, which have an alternating staggered mass m_s (see Fig. 3.1**(a)**). The gauge field sector, in the temporal gauge $A_0 = 0$, can be represented by rotor-angle operators (i.e. *compact QED*) living on the links, and fulfilling $[L_n, \Theta_m] = -\mathrm{i}\delta_{n,m}$. Here, the angle operators are related to the gauge field $\Theta_n = agA_1(\mathrm{x})$ at $\mathrm{x} = (n + \frac{1}{2})a$, while the rotors correspond to angular-momentum operators related to the electric field $L_n = E(\mathrm{x})/g = F_{01}(\mathrm{x})/g$. In this gauge, and using Schwinger's prescription for gauge-invariant point-split operators [104] $\bar{\Psi}(x+\epsilon)\Psi(x) \to \bar{\Psi}(x+\epsilon)\mathrm{e}^{-\mathrm{i}g\int_x^{x+\epsilon}\mathrm{d}x^\mu A_\mu(x)}\Psi(x)$, also known as the Peierls' substitution in condensed matter, the continuous-time Hamiltonian LGT for the standard massive Schwinger model becomes

$$H_{m\mathrm{S}} = a\sum_{n=1}^{N_s}\left(\frac{-1}{2a}\left(\mathrm{i}c_n^\dagger U_n c_{n+1} + \mathrm{H.c.}\right) + m_\mathrm{s}(-1)^n c_n^\dagger c_n + \frac{g^2}{2}L_n^2\right). \tag{3.2}$$

Here, we have introduced the link operators $U_n = \mathrm{e}^{\mathrm{i}\Theta_n}$, which act as unitary ladder operators $U_n|\ell\rangle = |\ell+1\rangle$ in the basis of electric-flux eigenstates $L_n|\ell\rangle = \ell|\ell\rangle$ for $\ell \in \mathbb{Z}$. Finally, we note that the aforementioned vacuum angle can be introduced through a background electric field E_ext by substituting $L_n \to L_n + \theta/2\pi$, where $\theta = 2\pi E_\mathrm{ext}/g$. With this notation, the lattice fields have the classical mass (energy) dimensions $d_c = 1/2$ and $d_L = 0$, while the mass and gauge coupling have $d_{m_s} = d_g = 1$, and the lattice constant $d_a = -1$.

The universal properties of this LGT, which are recovered by making a long-wavelength approximation in the continuum limit $a \to 0$, lead to the Hamiltonian field theory associated to Eq. (3.1). In this gauge, one obtains $H_{m\mathrm{S}} = \int \mathrm{d}\mathrm{x}\mathcal{H}_{m\mathrm{S}}$ with

$$\mathcal{H}_{m\mathrm{S}} = \overline{\Psi}(\mathrm{x})\big(\gamma^1(-\mathrm{i}\partial_\mathrm{x} - gA_1(\mathrm{x})) + m\big)\Psi(\mathrm{x}) + \tfrac{1}{2}E^2(\mathrm{x}), \tag{3.3}$$

where the gamma matrices are $\gamma^0 = \sigma^x$, $\gamma^1 = -\mathrm{i}\sigma^y$, and the Dirac mass coincides with the staggered one $m = m_\mathrm{s}$. The corresponding components of the Dirac spinor are

$$\psi_u(\mathrm{x}) = \frac{1}{\sqrt{L_s}}\sum_{|k|<\Lambda_\mathrm{c}}\mathrm{e}^{-\mathrm{i}k\mathrm{x}}c_k, \;\; \psi_d(\mathrm{x}) = \frac{1}{\sqrt{L_s}}\sum_{|k|<\Lambda_\mathrm{c}}\mathrm{e}^{-\mathrm{i}k\mathrm{x}}c_{k+\frac{\pi}{a}}, \tag{3.4}$$

where we have introduced the length of the chain $L_s = N_s a$, the fermionic operators in the momentum representation $c_k, c_k^\dagger$, and used a cutoff $\Lambda_\mathrm{c} \ll \pi/a$ to focus on the long-wavelength properties resembling the massive Dirac

fermions. This discretized Schwinger model, with a well-defined continuum limit (3.1), has served as a testbed of various numerical approaches, including finite-lattice methods [78], exact diagonalization [105], Monte Carlo techniques [106], density-matrix renormalization group (DMRG) [76] and, more recently, a variational ansatz based on matrix-product states [43]. These numerical results, together with subsequent works [81], have served to confirm and extend the above theoretical predictions.

Let us now introduce an alternative discretization which will, at first sight, yield the same gauge field theory in the continuum limit. Focusing on the above lattice model (3.2), one notices that the staggered mass breaks explicitly the lattice translational invariance, such that the discretized model has a two-site unit cell. A different discretization that maintains this property can be obtained by dimerizing the tunneling strengths with a two-site periodicity. This discretization will be referred to as the topological Schwinger model

$$H_{t\mathrm{S}} = a\sum_{n=1}^{N_s}\left(\frac{-1}{a}\left(\mathrm{i}(1-\delta_n)c_n^\dagger U_n c_{n+1} + \mathrm{H.c.}\right) + \frac{g^2}{2}L_n^2\right), \tag{3.5}$$

where the dimerization vanishes for even sites $\delta_{2n} = 0$, while it can be finite for odd sites $\delta_{2n-1} = \Delta$ (see Fig. 3.1**(b)**). We note that the total number of sites N_s should be even to respect inversion symmetry about the center of the chain. For $0 < \Delta \ll 1$, standard procedures show that the long-wavelength properties of this lattice model coincide again with Eq. (3.1) for a different choice of gamma matrices $\gamma^0 = \sigma^y$, $\gamma^1 = \mathrm{i}\sigma^z$, and fermion mass $m = -\Delta/a$. In this case, the Dirac spinor obtained is

$$\psi_u(\mathrm{x}) = \sqrt{\frac{2}{L_s}}\sum_{|k|<\Lambda_\mathrm{c}} \mathrm{e}^{-\mathrm{i}k\mathrm{x}} a_k, \;\; \psi_d(\mathrm{x}) = \sqrt{\frac{2}{L_s}}\sum_{|k|<\Lambda_\mathrm{c}} \mathrm{e}^{-\mathrm{i}k\mathrm{x}} b_k, \tag{3.6}$$

where a_k, b_k are momentum operators obtained from the odd- and even-site fermionic operators, respectively.

As announced above, both discretizations seem to yield the same continuum limit (3.3), such that one would naively expect to recover the same physics. In the following section, we show that the continuum limit of the topological Schwinger model (3.5) must be considered more carefully, as it can also host symmetry-protected topological phases. We will see that the new discretization exchanges the trivial staggered mass for a *topological mass*, which can stabilize strongly-correlated SPT phases where the fermions interact via the gauge field.

3.2 Topological QED$_2$ via bosonization

3.2.1 Symmetry-protected topological (SPT) phases in the non-interacting limit

In this subsection, we start by discussing the properties of the dimerized LGT (3.5) in the non-interacting limit $g = 0$. This task is straightforward, as the matter sector corresponds exactly with the so-called Su-Schrieffer-Heeger (SSH) model of polyacetylene in the adiabatic limit for the lattice vibrations [107, 108]. We now review these properties, placing a special emphasis to the connection to one-dimensional topological insulators, a paradigmatic example of an SPT phase.

For vanishing coupling $g = 0$, our model (3.5) reduces to $H_{t\mathrm{S}} = H_{\mathrm{SSH}} + a\sum_n E(\mathrm{x})^2/2$, such that the matter sector decouples from the gauge-field sector and can be described by

$$H_{\mathrm{SSH}} = -\mathrm{i}\sum_{n=1}^{N_s/2}(1-\Delta)a_n^\dagger b_n + b_n^\dagger a_{n+1} + \mathrm{H.c.}, \tag{3.7}$$

where we have rewritten the even (odd) fermionic operators c_{2n} (c_{2n-1}) using a two-site unit cell notation b_n (a_n). By performing a Fourier transform for periodic boundary conditions, one obtains $H_{\mathrm{SSH}} = \sum_{k\in\mathrm{BZ}} \Psi_k^\dagger h(k)\Psi_k$, where $h(k) = \boldsymbol{d}(k)\cdot\boldsymbol{\sigma}$ is the single-particle Hamiltonian, and $\Psi_k = (a_k, b_k)^{\mathrm{t}}$ is defined within the first Brillouin zone $\mathrm{BZ} = [-\pi/a, \pi/a)$. In this expression, $\boldsymbol{d}(k) = (-\sin ka, (1-\Delta-\cos ka), 0)/a$, and $\boldsymbol{\sigma}$ is the vector of all three Pauli matrices $\boldsymbol{\sigma} = (\sigma^x, \sigma^y, \sigma^z)$. Note that the dimerization leads to a momentum-dependent mass $m_t(k) = (1-\Delta-\cos ka)/a$, a so-called *topological mass* that substitutes the previous staggered mass m_{s}, and plays a crucial role in the appearance of the SPT phase.

As announced in the previous section, a naïve long-wavelength approximation yields $H_{\mathrm{SSH}} = \int \mathrm{dx}\mathcal{H}_{m\mathrm{D}}$, where

$$\mathcal{H}_{m\mathrm{D}} = \overline{\Psi}(\mathrm{x})(-\mathrm{i}\gamma^1\partial_{\mathrm{x}} + m)\Psi(\mathrm{x}) \tag{3.8}$$

is the Hamiltonian density for a massive Dirac field with $\gamma^0 = \sigma^y$, $\gamma^1 = \mathrm{i}\sigma^z$, and mass $m = -\Delta/a$ for dimerizations $\Delta \ll 1$.

Here, we have introduced the effective Dirac spinor $\Psi(\mathrm{x}) = (\psi_u(\mathrm{x}), \psi_d(\mathrm{x}))^{\mathrm{t}}$ with components defined in Eq. (3.6) for a small region around the origin of the Brillouin zone $|k| < \Lambda_{\mathrm{c}}$. Therefore, this long-wavelength approximation focuses on local aspects of the bands, and one might be loosing relevant information about global topological features that would require the knowledge of

the complete band structure. Indeed, one finds that the Berry connection for the lowest-energy band $\mathcal{A}_-(k) = \langle -\epsilon_k | \mathrm{i}\partial_k | -\epsilon_k \rangle$ of the full SSH model (3.7) is

$$\mathcal{A}_-(k) = \frac{1 - (1-\Delta)\cos ka}{2\big(1 + (1-\Delta)^2 - 2(1-\Delta)\cos ka\big)}. \tag{3.9}$$

The ground-state of the SSH model at half filling $|\mathrm{gs}\rangle = \otimes_{k\in \mathrm{BZ}} |-\epsilon_k\rangle$ displays a polarization proportional to a non-trivial topological invariant [109]: the so-called *Zak's phase* [110]. This invariant is obtained by integrating the Berry connection over all the occupied momenta

$$\varphi_{\mathrm{Zak}} = \int_{\mathrm{BZ}} \mathrm{d}k \mathcal{A}_-(k) = \pi\big(\theta(\Delta) - \theta(2-\Delta)\big), \tag{3.10}$$

where we have introduced Heaviside's step function $\theta(x) = 1$ for $x > 0$, and zero otherwise. Therefore, this Zak's phase can be associated to a *gauge-invariant topological Wilson loop* $W = \mathrm{e}^{\mathrm{i}\varphi_{\mathrm{Zak}}}$, which becomes non-trivial $W = -1$ when the dimerization lies in $\Delta \in (0, 2)$. This is precisely the region where the SSH model hosts an SPT phase, a topological insulator in the BDI symmetry class: the ground-state is characterized by a non-vanishing topological invariant respecting the symmetries of the underlying Hamiltonian. These correspond to time-reversal T $\sigma^z h(-k)^* \sigma^z = h(k)$, particle-hole C $h(-k)^* = -h(k)$, and sub-lattice S $\sigma^z h(k) \sigma^z = -h(k)$ symmetry, such that $\mathsf{T}^2 = \mathsf{C}^2 = +1$ [111].

As announced above, in order to capture the correct topological features, one cannot naively restrict to long-wavelengths $|k| < \Lambda_{\mathrm{c}}$ (3.8), since the information about the topological mass $m_{\mathrm{t}}(k)$ at the borders of the Brillouin zone $|k - \pi/a| < \Lambda_{\mathrm{c}}$ is also important. In the following section, we use the bulk-boundary correspondence for such SPT phase to derive the correct long-wavelength approximation. The goal of our work is to explore the fate of this SPT phase as the coupling with the gauge field is switched on $g > 0$, such that interactions in the matter sector are mediated by the gauge field, and the above simple description of the topological phase is no longer valid. Starting from the aforementioned correct long-wavelength approximation, superseding Eq. (3.3), we will show how strong correlations in the SPT phase can be brought by the coupling to the gauge field.

3.2.2 Continuum limit and topological QED$_2$

In this subsection, we focus on the regime $0 < \Delta \ll 1$, and derive an alternative long-wavelength approximation to Eq. (3.3) that is valid for the topological Schwinger model (3.5). We build on the bulk-edge correspondence, which states that the non-vanishing bulk topological invariant of the

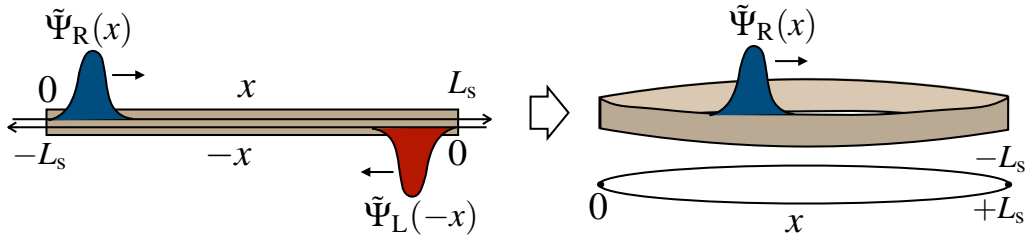

Figure 3.2: Chiral modes for Dirichlet boundary conditions: For a finite open chain, the right- and left-moving modes satisfying $\tilde{\Psi}_\eta(0) = \tilde{\Psi}_\eta(L_{\rm s}) = 0$, must fulfill $\tilde{\Psi}_{\rm R}(x) = -\tilde{\Psi}_{\rm L}(x)$, such that one may study modes of a fixed chirality living in an annulus, i.e. enlarged chain with periodic boundary conditions $\tilde{\Psi}_{\rm R}(L_{\rm s}) = \tilde{\Psi}_{\rm R}(-L_{\rm s})$.

previous section (3.10) is related to the presence of robust zero-energy modes localized to the boundaries of the sample, the so-called *topological edge states*. Our goal now is to revisit the continuum limit in a way that these edge states appear naturally.

Instead of considering periodic boundary conditions as in the previous subsections, we impose Dirichlet boundary conditions for an open finite chain. In the continuum limit, where $a \to 0$ and $N_s \to \infty$ with a fixed length $L_s = N_s a$, we can express the fermionic lattice operators as fields $c_n \to \Psi(\mathrm{x}) = \sqrt{2/L_s}\sum_k \sin(k\mathrm{x})c_k$, where $k = \frac{\pi}{L_s} j$ and $j \in \mathbb{N}$. Such fields fulfill directly the boundary conditions $\Psi(0) = \Psi(L_s) = 0$.

In order to unveil the low-energy excitations that resemble Dirac fermions, the standard approach in one-dimensional models is to break the field operator into right- and left-moving components $\Psi(\mathrm{x}) = \mathrm{e}^{\mathrm{i}k_{\rm F}\mathrm{x}}\tilde{\Psi}_{\rm R}(\mathrm{x}) + \mathrm{e}^{-\mathrm{i}k_{\rm F}\mathrm{x}}\tilde{\Psi}_{\rm L}(\mathrm{x})$, where $\{\tilde{\Psi}_\eta(\mathrm{x})\}_{\eta=\mathrm{R,L}}$ are slowly-varying envelopes that allow for a gradient expansion [112]. For an open chain, however, these right- and left-moving fields are not independent, but must instead fulfill $\tilde{\Psi}_{\rm L}(-\mathrm{x}) = -\tilde{\Psi}_{\rm R}(\mathrm{x})$ by imposing the Dirichlet boundary conditions [113] (see Fig. 3.2). Accordingly, the left-moving component can be obtained from the right-moving one, and one can focus on the right movers in a doubled chain with periodic conditions $\tilde{\Psi}_{\rm R}(-L_s) = \tilde{\Psi}_{\rm R}(+L_s)$.

In the present case, we are interested in the universal properties of Eq. (3.5) for $0 < \Delta \ll 1$, which are obtained by making a long-wavelength approximation around $k_{\rm F} = \pi/2a$ (i.e. wave-vector where the dispersion relation for open boundary conditions crosses the zero of energies). We can then restrict to momenta around the origin of the Brillouin zone $|k - \pi/2a| < \Lambda_{\rm c} \ll 1/a$, and perform a gradient expansion of the fermionic fields that yields a matter

sector governed by

$$H_{\mathrm{SSH}} = \int_0^{L_s} \mathrm{dx} \sum_{\eta=\mathrm{L,R}} s_\eta \left(\tilde{\Psi}^\dagger_\eta(\mathrm{x}) \mathrm{i}\partial_\mathrm{x} \tilde{\Psi}_\eta(\mathrm{x}) + \mathrm{i}m \tilde{\Psi}^\dagger_\eta(\mathrm{x}) \tilde{\Psi}_{\bar{\eta}}(\mathrm{x}) \right), \tag{3.11}$$

where we have introduced $s_\eta = (1 - 2\delta_{\eta,\mathrm{R}})$, $\bar{\eta} = \mathrm{L}, \mathrm{R}$ for $\eta = \mathrm{R}, \mathrm{L}$, and we recall that $m = -\Delta/a$. Here, the right- and left-moving fermions can be related to the original spinor components as follows $\tilde{\Psi}_\mathrm{R} = (\tilde{\Psi}_\mathrm{u} - \tilde{\Psi}_\mathrm{d})/\sqrt{2}$, $\tilde{\Psi}_\mathrm{L} = (\tilde{\Psi}_\mathrm{u} + \tilde{\Psi}_\mathrm{d})/\sqrt{2}$.

We can now use the condition $\tilde{\Psi}_\mathrm{L}(-\mathrm{x}) = -\tilde{\Psi}_\mathrm{R}(\mathrm{x})$ to get rid of the left-moving fields, and obtain the following continuum field theory for the right movers $H_{\mathrm{SSH}} = \int_{-L_s}^{+L_s} \mathrm{dx} \mathcal{H}_{t\mathrm{D}}$, where

$$\mathcal{H}_{t\mathrm{D}} = -\tilde{\Psi}^\dagger_R(\mathrm{x}) \mathrm{i}\partial_\mathrm{x} \tilde{\Psi}_R(\mathrm{x}) + \mathrm{i}m\,\mathrm{sgn}(\mathrm{x}) \tilde{\Psi}^\dagger_R(\mathrm{x}) \tilde{\Psi}_R(-\mathrm{x}). \tag{3.12}$$

Therefore, the naive continuum limit with massive Dirac fermions (3.8), must be replaced by this effective Hamiltonian field theory where the Dirac fermions display a *non-local mass* that changes sign at $x = 0$. This can be interpreted as a non-local version of the Jackiw-Rebbi quantum field theory, where fermionic zero-modes are localized within a kink excitation of a scalar field, which effectively changes the sign of the local mass term [114]. In fact, this continuum field theory (3.12) can be exactly diagonalized, and leads to two types of solutions: *(i)* bulk energy levels with $\epsilon(k) = \pm\sqrt{m^2 + k^2}$, where we recall that momentum is quantized $k = \pi j/L_s$ with $j \in \mathbb{N}$, such that the solutions fulfill the Dirichlet boundary conditions. Accordingly, these plane-wave solutions are delocalized within the bulk of the chain, and have a relativistic dispersion relation: they correspond to the previous massive Dirac field in the naive continuum limit (3.8) . Additionally, in the thermodynamic limit, we find *(ii)* a zero-energy mode localized at $\mathrm{x} = 0$ with wave-function $\tilde{\chi}_0(\mathrm{x}) \approx C\mathrm{e}^{-|\mathrm{x}|/\xi}$, where $\xi = a/\Delta \ll L_s \to \infty$ and $C = \sqrt{\Delta a}$. Therefore, provided that $\Delta > 0$ (otherwise the solution is not normalizable), we find a zero-mode exponentially localized to $\mathrm{x} = 0$. This coincides precisely with the topological edge state localized at the left boundary at $\mathrm{x} = 0$, while the remaining edge state at $\mathrm{x} = L_s$ can be recovered by means of inversion symmetry.

After going back to the physical un-doubled chain, and introducing the fast-oscillating terms components to these envelopes, the zero-energy solutions $\epsilon_\mathrm{L} = \epsilon_\mathrm{R} = 0$ can be expressed as

$$\chi_\mathrm{L}(\mathrm{x}) = C\mathrm{e}^{-\frac{\mathrm{x}}{\xi}} \sin(k_\mathrm{F}\mathrm{x}), \;\; \chi_\mathrm{R}(\mathrm{x}) = C\mathrm{e}^{-\frac{(L_s-\mathrm{x})}{\xi}} \sin(k_\mathrm{F}(L_s - \mathrm{x})), \tag{3.13}$$

which, in addition to the exponential decay from the boundaries, also show an oscillating character $\sin(\pi j/2)$ $(\sin(\pi(N-j)/2))$ such that the left-most

(right-most) edge state only populates the even (odd) sites. As a consistency check, we note that this exponential decay and alternating behavior has been also found for the SSH model using completely different approaches (see e.g. [115]).

With these results, the naive continuum limit for the SSH model in Eq. (3.8) gets superseded by $H_{\rm SSH} = \int_0^{L_s} {\rm dx}\mathcal{H}_{t\rm D}$, where

$$\mathcal{H}_{t\rm D} = \overline{\Psi}({\rm x})(-{\rm i}\gamma^1\partial_{\rm x} + \Delta/a)\Psi({\rm x}) + \sum_{\eta={\rm L,R}} \epsilon_\eta |\chi_\eta({\rm x})|^2 \hat{\eta}^\dagger\hat{\eta}, \tag{3.14}$$

which is valid for for $0 < \Delta \ll 1$. Here, in addition to the featureless bulk Dirac fermions of mass Δ/a, we have also included the exponentially-localized topological edge states created and annihilated by $\hat{\eta}^\dagger$ and $\hat{\eta}$. This forms the matter sector of the topological Schwinger model (3.5), which in the Coulomb gauge $A_1 = 0$ finds the following expression $H_{t\rm S} = \int {\rm dx}\mathcal{H}_{t\rm S}$, where

$$\mathcal{H}_{t\rm S} = \mathcal{H}_{t\rm D} - gA_0({\rm x})\overline{\Psi}({\rm x})\gamma^0\Psi({\rm x}) + \tfrac{1}{4}F^{\mu\nu}({\rm x})F_{\mu\nu}({\rm x}). \tag{3.15}$$

The gauge field theory in Eqs. (3.14)-(3.15) can be interpreted as a new type of topological QED in a (1+1)-dimensional space-time with boundaries. It describes how both the bulk relativistic fermions, and the fermionic zero-modes, interact with the gauge field preserving the $U(1)$ local symmetry characteristic of QED: *topological QED*$_2$. Although the edge modes seem to be decoupled from the gauge and Dirac fields, we discuss in the following section how a careful account of Gauss' law gives rise to such a coupling, and can indeed be used as a starting point to understand correlation effects in the SPT phase.

3.2.3 Bosonization and boundary Gauss' law

The reason underlying the change of gauge in the last subsection, moving from the temporal gauge of Eq. (3.3) to the Coulomb gauge of Eq. (3.15), is that the latter allows for a neat application of the machinery of bosonization [60, 68, 116]. In the context of the standard Schwinger model (3.1), this technique gives a clear understanding of various phenomena. In particular, it unveils the origin of the bosonic excitations of the massless Schwinger model, which are described by a Klein-Gordon field theory of mass $\mu = g/\sqrt{\pi}$. Additionally, the bosonized lattice gauge theory gives a neat account of the role of the vacuum θ angle [60]. We also mention that bosonization can be used to understand charge shielding in the massive Schwinger model [116], and it proved to be of the utmost importance to predict the existence of an

Ising-type second-order quantum phase transition between a charge-shielded phase and a symmetry-broken fermion condensate for $\theta = \pi$ [68]. We now apply this machinery to the topological QED$_2$ (3.15), and use it to predict quantitative results about the underlying phase diagram, which will include in addition to these two phases of matter, the SPT phase discussed above.

Following Coleman's work [68], the bulk part of topological QED$_2$ (3.15) can be simplified into $\mathcal{H}_{t\mathrm{S}} = \mathcal{H}_{t\mathrm{D}} + \frac{1}{2}E^2(\mathrm{x})$, where the typical electric energy appears directly in the Hamiltonian density. Although the matter and gauge-field sectors seem to be decoupled, we recall that the Gauss' law associated to the local $U(1)$ still needs to be imposed, and this will result in an effective matter-field coupling.

Following the bosonization of the massive Schwinger model (3.1), we start with the well-known relations between the bilinear operators formed by Dirac spinors $\Psi(\mathrm{x}), \overline{\Psi}(\mathrm{x})$, and the bosonic operators of a real scalar field $\phi(\mathrm{x}), \Pi(\mathrm{x})$ (i.e. bosonization dictionary), which in a (1+1) dimensions read

$$\begin{aligned} -\mathrm{i} : \overline{\Psi}(\mathrm{x})\gamma^1\partial_{\mathrm{x}}\Psi(\mathrm{x}) :_{\Delta} \; &\longrightarrow \; : \tfrac{1}{2}\Pi^2(\mathrm{x}) + \tfrac{1}{2}(\partial_{\mathrm{x}}\phi(\mathrm{x}))^2 :_{\mu}, \\ : \overline{\Psi}(\mathrm{x})\Psi(\mathrm{x}) :_{\Delta} \; &\longrightarrow \; - c\mu : \cos\left(2\sqrt{\pi}\phi(\mathrm{x})\right) :_{\mu}, \\ : \Psi^{\dagger}(\mathrm{x})\Psi(\mathrm{x}) :_{\Delta} \; &\longrightarrow \; - \partial_{\mathrm{x}}\phi/\sqrt{\pi}. \end{aligned} \tag{3.16}$$

Here, we have introduced $c = \mathrm{e}^{\gamma}/2\pi$ with Euler's constant $\gamma \approx 0.5774$, and $:(\;):_m$ denotes normal ordering of the Fermi or Bose fields with respect to the fermion mass m, corresponding to Δ/a in the present case, and the bosonic mass $\mu = g/\sqrt{\pi}$, respectively. The first expression yields the bosonization identity between a massless Dirac fermion and a massless scalar field, whereas the second one relates the fermion mass to a cosine-type non-linearity of the scalar field, which is a relevant perturbation of the resulting *sine-Gordon* quantum field theory. Finally, the last expression can be used in conjunction with Gauss' law to bosonize also the gauge-field contribution to the Hamiltonian. For the bulk Dirac fermions, this parallels Coleman's bosonization of the massive Schwinger model $\partial_{\mathrm{x}}E_{\mathrm{bulk}}(\mathrm{x}) = g : \Psi^{\dagger}(\mathrm{x})\Psi(\mathrm{x}) :_{\Delta}$, which directly leads to

$$E_{\mathrm{bulk}}(\mathrm{x}) = \frac{g}{\sqrt{\pi}}\left(\phi(\mathrm{x}) + \frac{\theta}{2\sqrt{\pi}}\right), \tag{3.17}$$

where one sees how the vacuum angle $\theta = 2\pi E_{\mathrm{ext}}/g$ originates from a constant field after the integration of Gauss' law.

The novel ingredient that is required for the bosonization of topological QED$_2$ (3.15) is to consider the modification on Gauss' law due to the existing boundaries. In the SPT phase, these boundaries may actually contain charges due to the population of the topological edge states (3.13). Focusing on the regime $0 < \Delta \ll 1$, where the edge-state localization length is very small

$\xi \ll L_s$, one can thus consider that the boundary charge only penetrates into a small region close to the edges. Considering the boundary conditions for the electromagnetic field across this region, which imply that the normal component of the electric field must be discontinuous, we find that

$$E_{\text{edge}}(\mathrm{x}) = \frac{g}{2}\left(\text{sign}(x)\hat{\mathrm{L}}^{\dagger}\hat{\mathrm{L}} + \text{sign}(x-L_s)\hat{\mathrm{R}}^{\dagger}\hat{\mathrm{R}}\right). \tag{3.18}$$

Essentially, the points that contain a charge contribute with a constant electric field of $+g/2$ to its right and $-g/2$ to its left, as is known already for 1D classical electrodynamics [117].

Substituting the bosonized version of $E(\mathrm{x}) = E_{\text{bulk}}(\mathrm{x}) + E_{\text{edge}}(\mathrm{x})$ into our model (3.15), together with the remaining bosonization identities (3.16), we find

$$\begin{aligned}\mathcal{H}_{t\mathrm{S}} = &\sum_{\eta} \epsilon_{\eta}|\chi_{\eta}(\mathrm{x})|^2\hat{\eta}^{\dagger}\hat{\eta} + \tfrac{1}{2}\Pi^2(\mathrm{x}) + \tfrac{1}{2}(\partial_{\mathrm{x}}\phi(\mathrm{x}))^2 \\ &- c\mu\frac{\Delta}{a}\cos\left(2\sqrt{\pi}\phi(\mathrm{x})\right) + \frac{g^2}{2\pi}\left(\phi(\mathrm{x}) + \frac{1}{2\sqrt{\pi}}\hat{\theta}\right)^2,\end{aligned} \tag{3.19}$$

where normal ordering with respect to the mass μ is assumed. Here, the vacuum angle has turned into a dynamical operator that depends, not only on the constant external field via $\theta = 2\pi E_{\text{ext}}/g$, but also on the population of the edge states

$$\hat{\theta} = \theta + \pi\left(\text{sign}(x)\hat{\mathrm{L}}^{\dagger}\hat{\mathrm{L}} - \text{sign}(x-L_s)\hat{\mathrm{R}}^{\dagger}\hat{\mathrm{R}}\right). \tag{3.20}$$

Equations (3.19) and (3.20) are the main result of this subsection, encapsulating several novel features of topological QED_2 in a succinct manner, which we shall try to unveil in the following subsection. However, before turning into that discussion, let us note that an interesting avenue for future work would be to consider that the topological zero-modes states are not bound to fixed boundaries, but instead localized to topological defects [118]. In this situation, these zero modes can be mobile as occurs for the Jackiw-Rebbi model [114], and the effective vacuum angle will display interesting dynamical effects on the gauge field that deserve further attention.

3.2.4 Phase diagram of topological QED_2

In this subsection, we analyze the consequences of our bosonization results on the properties of the topological Schwinger model, paying special attention to $\theta = \pi$. Let us comment, however, that even in the absence of an external

electric field $\theta = 0$, the new *vacuum-angle operator* (3.20) can indeed display values of $\langle\hat{\theta}\rangle_{\rm gs} = \pi$ when the half-filled ground-state lies in the SPT phase. The appearance of an effective vacuum angle in a topological phase recalls the situation found for 3D time-reversal topological insulators, where the bulk topological invariant can be shown to play the role of an effective vacuum angle. Such a vacuum angle modifies the response of the material to external electromagnetic fields, and leads to the so-called axion electrodynamics [119].

In the present case of topological QED_2, we have explicitly shown that the vacuum angle is not simply a c-number, or an adiabatic classical field [119], but that it becomes instead a quantum-mechanical operator with its own dynamics depending on the density of the topological edge states (3.20). Moreover, our theory incorporates the interplay of this operator with the 1D electromagnetic field, which is not an external field, but rather obeys its own dynamics. As we show now, the combination of these ingredients can lead to exotic situations in topological QED_2 where non-perturbative effects typical of higher-dimensional non-Abelian theories, such as charge shielding and confinement, interplay with the topological features characteristic of SPT phases.

Let us now focus on discussing the phase diagram of topological QED_2 for $\theta = \pi$ and start by identifying the possible phases for limiting regions of (Δ, ga). First of all, we already know from Eq. (3.10) that there is an SPT phase corresponding to the BDI topological insulator for $g = 0$, and $\Delta \in (0, 2)$. In fact, all the phases should be symmetric about $\Delta = 1$, such that one can focus on $\Delta \leq 1$ and then extend to the whole parameter range. The point $\Delta_{\rm c} = 0 = g_{\rm c}$ is a critical point that delimits the SPT region, and corresponds to a massless Dirac fermion that shall interact with the gauge field as soon as the coupling is switched on $g > 0$. As a consequence of the lattice implementation, whereby chiral symmetry is explicitly broken, the mass of the Dirac fermion will be renormalized due to the interactions. Accordingly, the critical point will flow with the coupling g from the limiting value $\Delta_{\rm c} = 0$ to finite values $\Delta_{\rm c}(g) \neq 0$, determining a critical line separating the SPT phase from another non-topological phase.

To derive a quantitative prediction for this critical line, we focus on the bosonized Hamiltonian (3.19). Expanding the term that contains the vacuum-angle operator, one sees that the edge-state densities get coupled to the bosonic scalar field via Yukawa-type couplings $\hat{\eta}^\dagger\hat{\eta}\phi(\mathrm{x})$. The resulting Hamiltonian is an analogue of a quantum impurity model [120], where the edge states play the role of the impurities, and the scalar field represents the current-carrying excitations of the bulk band. Due to the Yukawa-type couplings, the edge states will hybridize with the bulk excitations whenever the bulk band has a finite density of states at their energy $\epsilon_{\rm R} = \epsilon_{\rm L} = 0$.

Accordingly, when the renormalized mass of the scalar particles vanishes $\mu = g/\sqrt{\pi} \to \mu(g, \Delta) = 0$, the edge states will cease to be well-defined localized zero modes, resulting in a topological quantum phase transition. The solution of $\mu(g, \Delta) = 0$ will thus determine the critical line $\Delta_{\mathrm{c},1}(g)$, and the region with the ground-state in the SPT phase $\Delta \in (\Delta_{\mathrm{c},1}(g), 2 - \Delta_{\mathrm{c},1}(g))$.

By shifting the scalar field $\phi(\mathrm{x}) \to \phi(\mathrm{x}) - \langle\hat{\theta}\rangle_{\mathrm{gs}}/2\sqrt{\pi}$, one finds an effective potential

$$V(\phi) = \frac{g^2}{2\pi}\phi^2(\mathrm{x}) - c\mu\frac{\Delta}{a}\cos\left(2\sqrt{\pi}\phi(\mathrm{x}) - \langle\hat{\theta}\rangle_{\mathrm{gs}}\right), \tag{3.21}$$

Approaching the critical line from the SPT phase, the interplay of the external field and the edge states leads to a vacuum-angle operator fulfilling $\langle\hat{\theta}\rangle_{\mathrm{gs}} = 0 \ (\mathrm{mod} 2\pi)$, which has no effect on the effective potential. In the limit of small dimerization $|\Delta| \ll ga$, the sine-Gordon theory reduces to a massive Klein-Gordon field theory with leading-order mass

$$\mu(g, \Delta) = \frac{g}{\sqrt{\pi}}\left(1 + \frac{2\sqrt{\pi}\Delta}{ga}\mathrm{e}^{\gamma}\right)^{\frac{1}{2}}. \tag{3.22}$$

According to this expression, the non-interacting critical point $\Delta_{\mathrm{c}} = 0$ should flow to negative values of the dimerization according to the following straight line

$$\Delta_{\mathrm{c},1}(g) = -\frac{ga}{2\sqrt{\pi}}\mathrm{e}^{-\gamma}. \tag{3.23}$$

To identify the nature of the phase for dimerizations below the critical line $\Delta < \Delta_{\mathrm{c},1}(g)$, note that the topological contribution to the vacuum angle is absent since the edge zero modes have merged into the bulk bands. Therefore, $\langle\hat{\theta}\rangle_{\mathrm{gs}} = \pi$, and the sign of the non-linearity in the effective potential is reversed $V(\phi) = g^2\phi^2(\mathrm{x})/2\pi + c\mu\Delta\cos\left(2\sqrt{\pi}\phi(\mathrm{x})\right)/a$. Here, the discussion parallels the treatment of the standard massive Schwinger model [68], and we find that for dimerizations close to the critical line $\Delta \lesssim \Delta_{\mathrm{c},1}(g)$, the quadratic term dominates yielding a ground-state with $\langle\phi\rangle_{\mathrm{s}} = 0$. This phase displays *fermion trapping* (sometimes referred to as quark trapping or confinement), as the spectrum does not display the original charged fermions, but is entirely composed of massive bosonic excitations described by the scalar field (sometimes referred to as mesons). These bosonic excitations can be understood as bound fermion-antifermion pairs that cannot be widely separated, and we will refer to this phase as the *confined phase* (C).

It is interesting to revisit the SPT phase at $\Delta > \Delta_{\mathrm{c},1}(g)$ from this perspective. In this case, one finds that the spectrum contains states with the original charged fermions (3.19), and not only the bosonic bulk excitations interpreted as mesons. However, note that these excitations are not described

by the fundamental Dirac fermions of the theory, but correspond instead to the topological zero modes localized to the boundaries of the chain. From this perspective, starting from a half-filled ground-state, one may create a fermion and hole at the boundaries of the chain, which are closer in spirit a pair of heavy probe charges separated by a large distance L. This property is typically referred to as *charge shielding*, as the probe charges are not subjected to the long-range Coulomb force, and is a different manifestation of the quark trapping in the bulk [116]. It is intriguing that these analogue probe charges are self-assembled in the SPT phase due to the energetics and that, moreover, they do not need to be heavy static particles since the topological features of the SPT phase guarantees that they will be zero-energy modes contributing to the vacuum angle.

Finally, well-below the critical line $\Delta \ll \Delta_{c,1}(g)$, the non-linearity of the potential dominates, yielding a ground-state with $\langle\phi\rangle_s \neq 0$ that spontaneously breaks a discrete $\mathbb{Z}_2$ symmetry $\phi(x) \to -\phi(x)$. Accordingly, there should be another critical line $\Delta_{c,2}(g)$, such that the ground-state corresponds to the above confined phase for $\Delta_{c,2}(g) < \Delta < \Delta_{c,1}(g)$, while it lies in the symmetry-broken phase for $\Delta < \Delta_{c,2}(g)$. According to the bosonization dictionary, this symmetry-broken phase displays $\langle E(x)\rangle \neq 0$, but also $\langle\overline{\Psi}(x)i\gamma^5\Psi(x)\rangle \neq 0$, which is typically referred to as a *fermion condensate* (FC). This phase also has a two-fold degeneracy, but it is caused by the spontaneously broken $\mathbb{Z}_2$ symmetry, and not by the zero-energy edge modes of the SPT phase. Indeed, since these zero modes disappeared already in the SPT-C transition, the C-FC phase transition is completely analogous to the phase transition in the massive Schwinger model for $\theta = \pi$. Using the results of this well-studied model [76], we conjecture that the second critical line of the topological QED_2 corresponds to

$$\Delta_{c,2}(g) = -\frac{1}{3}ga. \tag{3.24}$$

Gathering all this information, and considering the symmetry about $\Delta = 1$, we can draw the qualitative phase diagram of topological QED_2 represented in Fig. 3.3. From the weak coupling predictions, the width of the region encompassing the non-interacting SPT phase increases as interactions are switched on (indeed, one can find interaction-induced topological phase transitions along the semi-transparent arrow of this figure). However, this behavior cannot be maintained indefinitely, since the phase should correspond to the confined phase C at very strong couplings. Therefore, we conjecture that the critical line $\Delta_{c,1}(g)$ will eventually bend, and the SPT phase will be contained in a finite lobe in parameter space. It would be very interesting to understand if these predictions of the critical lines can be analytically

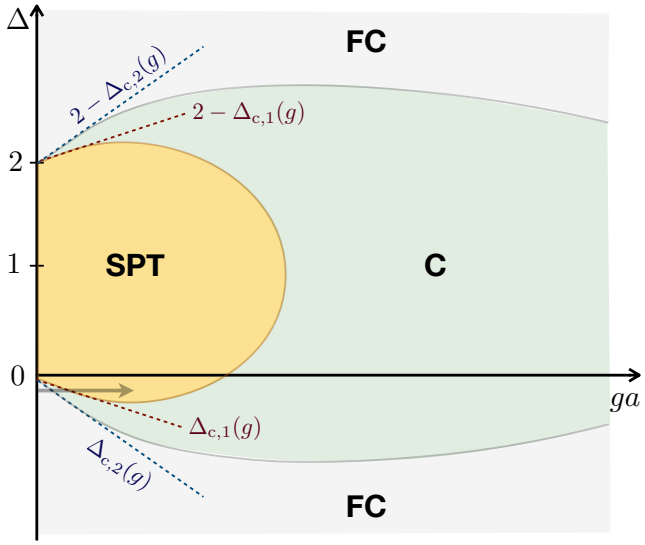

Figure 3.3: Phase diagram of topological QED_2: The bosonized model (3.19) allows us to predict three distinct phases: a symmetry-protected topological (SPT) phase, corresponding to a correlated BDI topological insulator, separated from a confined phase (C) through a continuous quantum phase transition. This confined phase is itself separated from a symmetry-broken fermion condensate (FC) by another continuous phase transition.

recovered by a perturbative Kadanoff-Wilson renormalization group for the bosonized massive sine-Gordon model [121] and, more interestingly, if they can be extended to larger gauge couplings g in a systematic fashion that allows to predict their curvature. We leave this for future, and focus below on a different numerical approach also based on the renormalization group.

3.3 Topological QED_2 via Density-Matrix Renormalization Group

3.3.1 $\mathbb{Z}_N$ topological Schwinger model on the lattice

The goal of this section is to test numerically the above bosonization predictions, exploring additional properties that can complement our understanding of the topological Schwinger model. In order to do so, we will use the same discretization presented in Sec. 1.2. Thus, we will analyze numerically the model with a truncated Abelian gauge group to $\mathbb{Z}_N$, and extrapolate our results to the $U(1)$ case of interest by taking the large-N limit in a controlled

manner.

Let us start by reviewing the Hamiltonian approach to lattice gauge theories for the discrete Abelian gauge group $\mathbb{Z}_N$ (presented in Sec. 1.2), which gives access to the properties of compact QED in the large-N limit. For the massive Schwinger model (3.1), this offers an alternative [29] to the Kogut-Susskind approach (3.2) based on the Hamiltonian

$$H_{m\mathrm{S}}^{\mathbb{Z}_N} = a\sum_{n=1}^{N_s}\Big(\frac{-1}{2a}\left(\mathrm{i}c_n^\dagger \tilde{U}_n c_{n+1} + \mathrm{H.c.}\right) + m_{\mathrm{s}}(-1)^n c_n^\dagger c_n + a(\tilde{V}_n + \tilde{V}_n^\dagger - 2)\Big), \tag{3.25}$$

where we have introduced two types of unitary link operators $\tilde{U}_n, \tilde{V}_n$ that obey the $\mathbb{Z}_N$ algebra. Accordingly, instead of using the rotor-angle operators of the Kogut-Susskind approach (3.2), one uses link operators fulfilling $\tilde{U}_n^N = \tilde{V}_n^N = \mathbb{I}$, and $\tilde{V}_n^\dagger \tilde{U}_n \tilde{V}_n = \mathrm{e}^{\mathrm{i}2\pi/N}\tilde{U}_n$. In analogy to the Kogut-Susskind approach, using the electric-flux eigenbasis $\tilde{V}_n|v\rangle = v|v\rangle$ with $v \in \mathbb{Z}_N$, the remaining link operators act as ladder operators that raise the electric flux by one quantum $\tilde{U}_n|v\rangle = |v+1\rangle$. The main difference is that, in contrast to the Kogut-Susskind approach, the ladder operators have a cyclic constraint $\tilde{U}_n|N\rangle = |1\rangle$.

We note that these link operators can be defined in terms of the vector potential and the electric field $\tilde{U}_n = \exp\{\mathrm{i}agA_n\}$, $\tilde{V}_n = \exp\{\mathrm{i}\frac{2\pi}{N}\frac{E_n}{g}\}$. In this way, the $\mathbb{Z}_N$ algebra $[\tilde{U}_n, \tilde{V}_n] = \mathrm{e}^{\mathrm{i}2\pi/N}$ can be satisfied by imposing the usual canonical commutation relations $[E_n, A_m] = \mathrm{i}\delta_{n,m}/a$, which have the correct continuum limit $[E(x), A(y)] = \mathrm{i}\delta(x-y)$. Note also that the gauge-group condition $\tilde{U}_n^N = \tilde{V}_n^N = \mathbb{I}$ requires that the electric-flux eigenvalues of $\tilde{L}_n = E_n/g$ should span $\sigma(\tilde{L}_n) = \{-\frac{1}{2}(N-1), \cdots, \frac{1}{2}(N-1)\}$. This yields $\sigma(\tilde{L}_n) \to \mathbb{Z}$ in the large-N limit, which corresponds to the spectrum of the rotor operator L_n of the Kogut-Susskind approach. In the same manner, the eigenvalues of the vector potential should lie in $\sigma(agA_n) = \{-\pi(N-1)/N, \cdots, \pi(N-1)/N\} \to [-\pi, \pi]$, corresponding to the basis of the angle operator Θ_n in the Kogut-Susskind approach (3.2), and leading to compact QED_2. We remark that, as emphasized in [29], the electric-energy term in Eq. (3.25) can be substituted by an arbitrary function $(V_n + V_n^\dagger - 2) \to f(V_n) = f^\dagger(V_n)$, and we will focus on $f(V_n) = \frac{1}{2}g^2\tilde{L}_n^2$. In this way the Hamiltonian is totally equivalent to the model studied in Chapter 1.

In the following, we use this $\mathbb{Z}_N$ approach to investigate numerically the phase diagram of topological QED_2 by using the density-matrix renormalization group (DMRG) algorithm. In particular, we use it to explore the

properties of the lattice Hamiltonian

$$H_{\mathrm{tS}}^{\mathbb{Z}_N} = a\sum_{n=1}^{N_s}\left(\frac{-1}{a}\left(\mathrm{i}(1-\delta_n)c_n^\dagger \tilde{U}_n c_{n+1} + \mathrm{H.c.}\right) + \frac{g^2}{2}\tilde{L}_n^2\right), \tag{3.26}$$

which is the discrete $\mathbb{Z}_N$ version of the topological Schwinger model with parameters introduced in Eq. (3.5). In order to take into account Gauss's law

$$G_n = c_n^\dagger c_n + \frac{1}{2a}[(-1)^n - 1] - \frac{1}{a}(\tilde{L}_n - \tilde{L}_{n-1}). \tag{3.27}$$

we follow the same construction presented in Sec. 1.4.1 for our numerical implementation in the DMRG-algorithm. This is a very important constraint that allows us to construct directly the physical Hilbert space of the $\mathbb{Z}_N$ model.

3.3.2 Phase diagram of the $\mathbb{Z}_3$ topological Schwinger model on the lattice

SPT phase: order parameters, entanglement spectrum, and edge states

The simplest non-trivial case studied in our work correspond to $N = 3$, and yields the $\mathbb{Z}_3$ model (3.26) with three electric-flux levels on each link.

Let us start by introducing the relevant observables to unveil the phase diagram of the model (3.26) numerically. As an informative case, we will start by focusing on $\Delta = 0.5$ while varying the coupling constant g, after setting $a = 1$. In order to understand the ground-state properties of our model, we will study the behavior of the usual *electric-field order parameter*, which can be defined as

$$\Sigma = \frac{1}{N_s}\sum_{n=1}^{N_s}\langle \mathrm{gs}|E_n|\mathrm{gs}\rangle, \tag{3.28}$$

and of the *staggered density*, which can be written as

$$\rho_{\mathrm{s}} = \frac{1}{2} + \frac{1}{N_s}\sum_{n=1}^{N_s}\langle \mathrm{gs}|(-1)^n c_n^\dagger c_n|\mathrm{gs}\rangle. \tag{3.29}$$

We obtain an approximation to the ground-state $|\mathrm{gs}\rangle$ using our DMRG algorithm for open boundary conditions, where we keep $m = 1000$ states in the iterative diagonalization and coarse graining of a lattice with $N_s = 80$ sites.

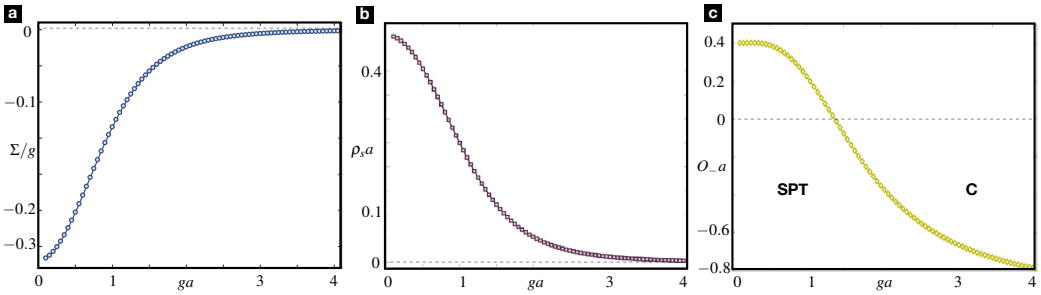

Figure 3.4: Observables for the $\mathbb{Z}_3$ topological Schwinger model: (a) Electric field order parameter (3.28) as a function of the gauge coupling constant g, for a dimerization of $\Delta = \frac{1}{2}$ a lattice of $N_s = 80$ sites. (b) Same as (a), but for the staggered density (3.29). (c) Same as (a), but for the topological correlator (3.30).

In Figs. 3.4**(a)** and 3.4**(b)**, we represent the above observables for the DMRG ground-state. As follows from these figures, at small g, the ground-state consists of a superposition of the anti-meson state (with negative electric field between couples) and the Dirac vacuum (see Fig. 1.4). As one increases the coupling, the ground state becomes the standard Dirac sea without electric or matter/antimatter excitations ($\Sigma \approx 0$, $\rho_s \approx 0$). This behavior points towards a possible quantum phase transition between both ground-states, which will be proved rigorously in the following sections by making a finite-size scaling analysis of the electric-field order parameter. However, these observables shed no light on the existence of the SPT phase discussed previously.

To investigate the topological properties of our model and, in particular, to verify numerically the existence of the SPT phase, we now discuss an alternative observable recently introduced in the context of the SSH model [122]. By using the maximally-localized solutions of the fully-dimerized SSH model, one can define a correlator that can be used to identify the topological phase of the SSH model, i.e. *topological correlator*, namely

$$O_-^{(j)} = \frac{3}{2}\langle \mathrm{gs}|c_j^\dagger c_{j+1} + c_{j+1}^\dagger c_j|\mathrm{gs}\rangle + \rho_{j,j+1} - \frac{1}{2}(\rho_j + \rho_{j+1}), \tag{3.30}$$

where $\rho_j = \langle \mathrm{gs}|c_j^\dagger c_j|\mathrm{gs}\rangle$ are fermion densities, $\rho_{j,j+1} = a\langle \mathrm{gs}|c_j^\dagger c_j c_{j+1}^\dagger c_{j+1}|\mathrm{gs}\rangle$ represents the density-density correlation, and the site index j must be odd. By summing over all odd sites of our chain, one obtains $O_- = \frac{2}{N}\sum_{n=1}^{N_s/2} O_-^{(2n-1)}$.

We now show that this topological correlator can identify the underlying SPT phase of the topological Schwinger model. We now present the behavior of O_- for $\Delta = 0.5$, by varying the gauge coupling g (see Fig. 3.4**(c)**). This figure shows a clear sign reversal of the correlator, a behavior that is qualitatively analogous to the transition from the topological phase ($O_- > 0$) to the

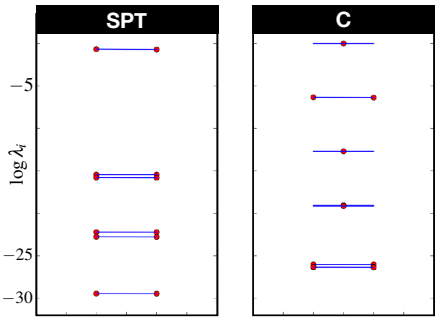

Figure 3.5: Entanglement spectrum for the $\mathbb{Z}_3$ topological Schwinger model: We show the first eigenvalues of the reduced density matrix for parameters within the (left) the symmetry-protected topological (SPT) phase ($\Delta = 0.5$, $g = 0.2$), showing an accurate double degeneracy, and (right) the confined (C) phase ($\Delta = 0.5$, $g = 5.0$).

trivial one ($O_- < 0$) in the non-interacting SSH model [122]. Accordingly, the region where the ground state is dominated by anti-mesons of Figs. 3.4 (i.e. small g), coincides with an SPT phase, as predicted by our analytical arguments of the topological Schwinger model in the previous sections (see Fig. 3.3). As we will show in further subsections below, this topological correlator can be used in combination to the electric-field order parameter to perform a careful finite-size scaling, and provide a detailed estimate of the different regions of the phase diagram.

In order to have an alternative confirmation of the topological nature of this SPT phase, we now study the *entanglement spectrum* [123]. If we consider the reduced density matrix of a partition A of our system, which yields a reduced density matrix $\tilde{\rho}_A = \mathrm{Tr}_B|\mathrm{gs}\rangle\langle\mathrm{gs}|$, where B is the complement of A; the entanglement spectrum is defined as the set of the eigenvalues of $\tilde{\rho}_A$ (in logarithmic scale). As pointed out in [124, 125], the entanglement spectrum leads to a powerful tool to analyze topological phases, since there must be an exact degeneracy of the eigenvalues for SPT phases. As shown in the left panel of Fig. 3.5, for a small gauge couplings g, we find doublets in this spectrum, thus confirming that our ground-state corresponds to an SPT phase. On the contrary, this degeneracy is absent in the right panel for a larger g, which should correspond to the non-topological confined phase (C) of Fig. 3.3.

As discussed in the previous section, the SPT phase can also be characterized by the presence of edge states. In fact, the two-fold degeneracy of the entanglement spectrum is also related to the presence of zero-energy edge modes [125], and the left panel of Fig. 3.5 can be considered as an indirect

confirmation of the prediction of Sec 3.2.2. In order to have a more direct numerical evidence, it is possible to extract the wave functions of the zero-energy edge modes taking by using DMRG ground-states with a different number of particles.

Let us start by considering the SPT phase in the non-interacting limit $g = 0$, where two zero-energy edge modes are present. Since the Hamiltonian commutes with the number operator, the Hilbert space can be divided into sectors with a fixed number of particles. Neglecting small finite-size corrections to their energies, which will eventually disappear in the thermodynamic limit, there will be four degenerate states in the ground-state manifold: $|\mathrm{gs}_{N_\mathrm{s}-1}\rangle$ in the sector with $N_\mathrm{s}-1$ particles, $|\Phi_\mathrm{L}\rangle$, $|\Phi_\mathrm{R}\rangle$ in the sector with N_s particles with the leftmost or rightmost edge modes populated, and $|\Phi_\mathrm{L},\Phi_\mathrm{R}\rangle$ in the sector with N_s+1 particles hosting both populated edge modes. Let now $\Phi_\mathrm{L}^\dagger$ represent the operator that excites the leftmost zero-energy mode, i.e. $\Phi_\mathrm{L}^\dagger = \sum_n \alpha^n c_n^\dagger$ for some $\alpha < 1$, and analogously for the rightmost zero-energy mode $\Phi_\mathrm{R}^\dagger$. Accordingly, we can obtain the ground-state with N_s particles as $|\Phi_\mathrm{L}\rangle = \Phi_\mathrm{L}^\dagger|\mathrm{gs}_{N_\mathrm{s}-1}\rangle$ (or equivalently $|\Phi_\mathrm{R}\rangle = \Phi_\mathrm{R}^\dagger|\mathrm{gs}_{N_\mathrm{s}-1}\rangle$), and the ground state with $N_\mathrm{s}+1$ particles as $|\Phi_\mathrm{L},\Phi_\mathrm{R}\rangle = \Phi_\mathrm{L}^\dagger\Phi_\mathrm{R}^\dagger|\mathrm{gs}_{N_\mathrm{s}-1}\rangle$. Using the DMRG algorithm, we can numerically target the lowest energy state in sectors with a generic number of particles, and we can thus calculate the following expectation value

$$B_n = \langle\Phi_\mathrm{L},\Phi_\mathrm{R}|c_n^\dagger c_n|\Phi_\mathrm{L},\Phi_\mathrm{R}\rangle. \tag{3.31}$$

Note that in the non-interacting limit, by applying Wick's theorem, this observable becomes

$$B_n = |\langle\mathrm{gs}_{\mathrm{N_s}-1}|c_n|\Phi_\mathrm{L}\rangle|^2 + |\langle\mathrm{gs}_{\mathrm{N_s}-1}|c_n|\Phi_\mathrm{R}\rangle|^2 + \langle\mathrm{gs}_{N_\mathrm{s}-1}|c_n^\dagger c_n|\mathrm{gs}_{N_\mathrm{s}-1}\rangle. \tag{3.32}$$

Interestingly, given the above expression of the edge operators, the first two terms of the above expression contain the probabilities associated to the edge-state wave-functions. These wave-functions can thus be obtained by calculating numerically

$$\psi_n^2 = B_n - \langle\mathrm{gs}_{N-1}|c_n^\dagger c_n|\mathrm{gs}_{N-1}\rangle. \tag{3.33}$$

Recalling that the operators Φ_L (Φ_R) has support only on even (odd) sites (3.13), it is possible to reconstruct the amplitude of the left-most (right-most) edge mode by plotting the quantity ψ_n^2 as a function of even (odd) n.

We expect that this behavior of the observable (3.31) should hold in the interacting regime, giving us a method to study the *many-body zero-energy edge modes* of the topological Schwinger model. In order to test

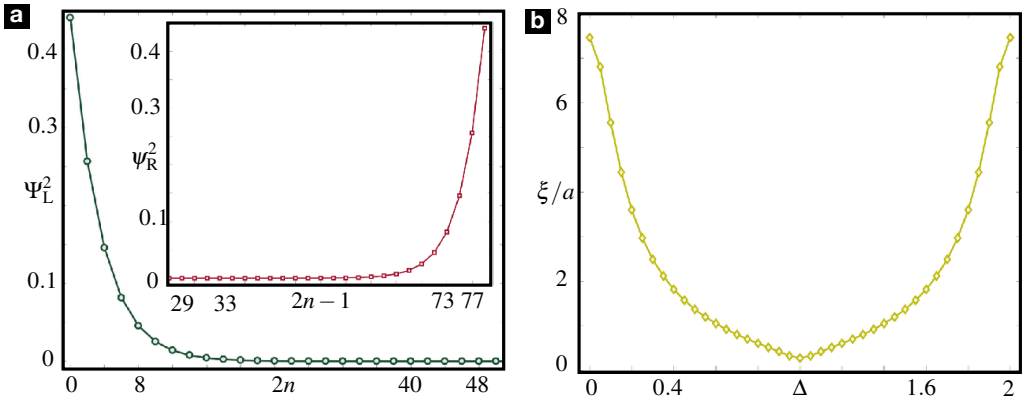

Figure 3.6: Many-body edge states for the $\mathbb{Z}_3$ topological Schwinger model: (a) (main panel) Probability of the wave function of the left-most edge mode for different values of Δ in the SPT phase ($ga = 0.2$), extracted from Eq. (3.33) evaluated at even sites. (inset) Same for the right-most edge state, extracted from Eq. (3.33) evaluated at odd sites. (b) Localization length ξ for the zero-energy edge modes (3.13) as a function of Δ in the SPT phase.

this conjecture, we explore different values of Δ in the SPT phase for a gauge coupling $ga = 0.2$, and obtain the plots in Fig. 3.6**(a)**, where the exponential decay from the boundary of the edge modes becomes readily visible, in agreement with Eq. (3.13). We can fit this behavior with an exponential function in order to extract the localization length ξ as a function of Δ. As shown in Fig. 3.6**(b)** for different system sizes, this quantity is very small deep into the topological phase, and grows as we approach the critical points $\Delta_c \approx 0$ and $\Delta_c \approx 2$.

All these numerical results give compelling evidence for the existence of SPT phases in the topological Schwinger model. Moreover, they also point to the existence of quantum phase transitions to other possible phases with different properties in the matter and gauge-field sectors. In the following section, we build on this evidence, and introduce additional numerical finite-size scaling studies that allow us to recover the full phase diagram of the model, testing the predictions of Fig. 3.3.

Critical lines: scaling analysis, entanglement entropy, and central charges

In order to determine properly the phase diagram of our $\mathbb{Z}_3$ model, we start by performing a finite-size scaling of the SPT order parameter O_-. In the SSH model, the quantum phase transition has critical exponents $\beta = 1/8$ and $\nu = 1$. Therefore, we can start to explore the critical behavior of the

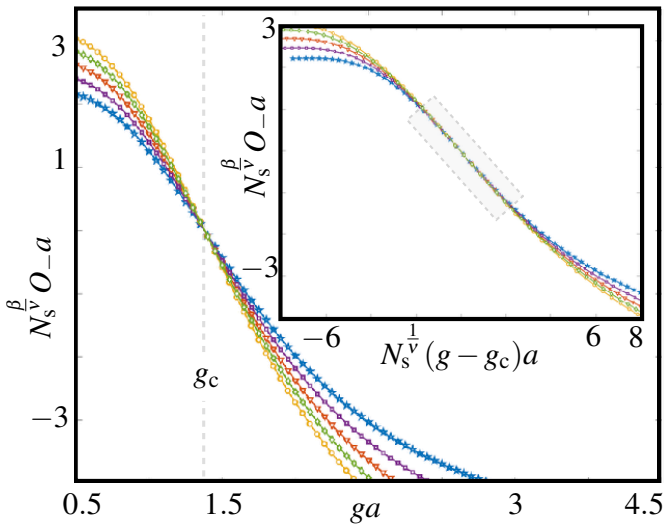

Figure 3.7: Finite-size scaling for the topological correlator of the $\mathbb{Z}_3$ topological Schwinger model: (main panel): Scaling quantity $N_s^{\beta/\nu} O_- a$ for the topological correlator (3.30), calculated for $\Delta = 0.5$ as a function of the gauge coupling for various system sizes $N_s \in \{24, 28, 32, 36, 40\}$ (top to bottom). The crossing point of all curves yields a value of the critical point separating the SPT and C phases of $g_c a \approx 1.384$. (inset) Universal scaling of the topological correlator within the Ising universality class $\nu = 1$ and $\beta = 1/8$, i.e. data collapse of the curves $N_s^{\beta/\nu} O_- a$ as function of $N_s^{1/\nu}(g - g_c)a$ displayed in the shaded region.

topological Schwinger model for finite gauge couplings by assuming these values in the scaling relation

$$N_s^{\frac{\beta}{\nu}} O_- = \lambda \left(N_s^{\frac{1}{\nu}} (g - g_c) \right). \tag{3.34}$$

in which $\lambda(x)$ is a universal function. Therefore, by fixing $\Delta = 0.5$ and plotting the quantity $N_s^{\beta/\nu} O_-$ as a function of g for different values of N_s, we obtain the behavior of Fig. 3.7.

We note that for $g = g_c$, the value $\lambda(0)$ becomes independent of the system size. Therefore, one expects to find a crossing of the curves for different lengths precisely at the critical point. This is exactly the behavior observed in the main panel of Fig. 3.7, which allows us to predict a critical point at $g_c \approx 1.384/a$. To check the initial hypothesis concerning the values of the critical exponents $\beta = 1/8$ and $\nu = 1$, we analyze the quantity $N_s^{\beta/\nu} O_-$ as a function of the argument $N_s^{1/\nu}(g - g_c)$. In this case, for different system sizes, we should observe a universal behavior when $g \approx g_c$ (i.e. collapse of the different curves into a single one). This is exactly what is observed in the inset

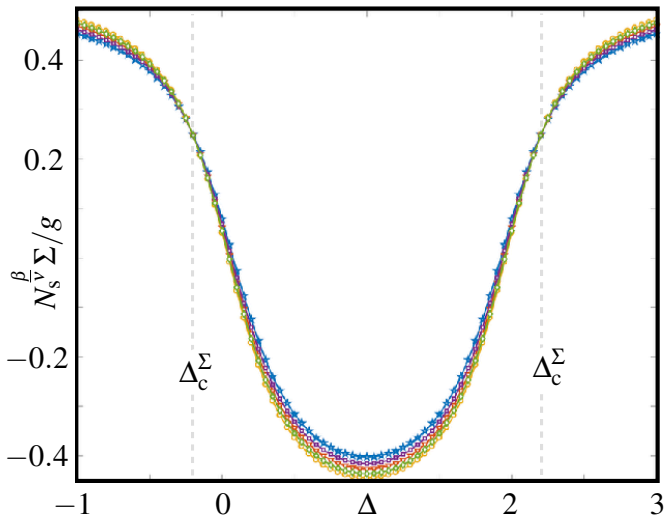

Figure 3.8: Finite-size scaling for the electric order parameter of the $\mathbb{Z}_3$ topological Schwinger model: Scaling quantity $N_s^{\beta/\nu}\Sigma/g$ for the electric-field order parameter (3.30), calculated for $ga = 0.6$ as a function of the dimerization for various system sizes $N_s \in \{24, 28, 32, 36, 40\}$ (top to bottom). The two crossing points of all curves yield the values of the critical dimerizations of $\Delta_c^{\Sigma} \approx -0.215$ and $\Delta_c^{\Sigma} \approx 2.216$, showing the symmetry with respect to $\Delta = 1$.

of Fig. 3.7, confirming in this way the initial hypothesis about the universality class of the SPT-C phase transition. In the same spirit, we can now fix a particular value of g, and calculate the topological correlator by varying the dimerization parameter Δ (vertical lines in the plane $ga - \Delta$). In contrast to the previous case, we now extract two critical points $\Delta_c^{O-} \approx -0.162$ and $\Delta_c^{O-} \approx 2.160$ for $ga = 0.6$. As expected from our discussion of Sec. 3.2.4, these points delimit the area of the SPT phase, and are expected to be symmetrical with respect to $\Delta = 1$.

Let us remark that, according to our analytical calculations for the phase diagram of Fig. 3.3, we expect a quantum phase transition from the fermion condensate (FC) to the confined phase (C) as a function of Δ in addition to the transition SPT-C detected by the parameter O_-. As conjectured in Sec. 3.2.4, this transition should be analogous to the phase transition of the standard massive Schwinger model. As we showed in Sec. 1.4.2, such a transition can be numerically detected by the electric field order parameter Σ (3.28). Thus, by studying the behavior of Σ for $ga = 0.6$, we obtain the plot of Fig. 3.8, which shows that the ground state is dominated by mesons for $\Delta \ll 0$ and $\Delta \gg 2$ (positive electric flux), and by anti-mesons for $\Delta \approx [0, 2]$ (negative electric flux, SPT phase). Following the scheme of the previous

ga	Δ_c^{Σ}	Δ_c^{Σ}	$\Delta_c^{O_-}$	$\Delta_c^{O_-}$
0.01	0.008	1.995	0.009	1.994
0.05	−0.024	2.030	−0.022	2.028
0.10	−0.064	2.072	−0.062	2.069
0.20	−0.121	2.119	−0.120	2.118
0.60	−0.215	2.216	−0.162	2.160
1.00	−0.257	2.259	−0.051	2.052
3.00	−0.210	2.211	//	//

Table 3.1: Critical values of Δ (related to the two transitions FC-C and SPT-C) obtained for different values of g. The numerical error is equal to 10^{-3}.

transition SPT-C, we can perform a finite-size scaling analysis with

$$N_{\mathrm{s}}^{\frac{\beta}{\nu}}\Sigma = \lambda\left(N_{\mathrm{s}}^{\frac{1}{\nu}}(\Delta - \Delta_{\mathrm{c}})\right), \tag{3.35}$$

where we use the universality class of the massive Schwinger model, which is the 2D Ising class $\beta = 1/8$, $\nu = 1$ [68, 76, 78]. Accordingly, we obtain the plot in Fig. 3.8, which allows us to detect two critical points $\Delta_{\mathrm{c}}^{\Sigma} \approx -0.215$ and $\Delta_{\mathrm{c}}^{\Sigma} \approx 2.216$, again symmetrical with respect to the value $\Delta = 1$.

We can repeat this procedure, using both O_- and Σ, to determine the critical points related to the two transitions SPT-C and FC-C for different values of g. The resulting values are shown Table 3.1. As can be observed in the last line of this table, when the gauge coupling g is sufficiently large, we still observe the FC-C transition, while the SPT-C transition is absent. This means that the SPT phase disappears for large g, as conjectured in Sec. 3.2.4.

Another necessary ingredient for the universality class of the SPT-C transition comes from the scaling of the *entanglement entropy*. In analogy with the entanglement spectrum, the entanglement entropy $S(\tilde{\rho}_A) = -\mathrm{Tr}\left[\tilde{\rho}_A \log_2\left(\tilde{\rho}_A\right)\right]$ is defined for reduced density matrix of a partition A of our system $\tilde{\rho}_A = \mathrm{Tr}_B|\mathrm{gs}\rangle\langle\mathrm{gs}|$, where B is the complement of A. According to conformal field theory (CFT) [73, 126], considering a subsystem A of size l within the chain with $L_{\mathrm{c}} = N_{\mathrm{s}}/2$ couples of sites, we expect to observe a logarithmic scaling of the block entanglement entropy if the system is at a quantum critical point

$$S_{L_{\mathrm{c}}}(l) = \frac{c}{6}\log_2\left[\frac{2L_{\mathrm{c}}}{\pi}\sin\left(\frac{\pi l}{L_{\mathrm{c}}}\right)\right] + s_0, \tag{3.36}$$

where s_0 is a non-universal constant. As shown in Fig. 3.9**(a)**, we observe such a scaling for $ga = 0.6$ and $\Delta_c^{O-} = -0.162$, from which it is possible

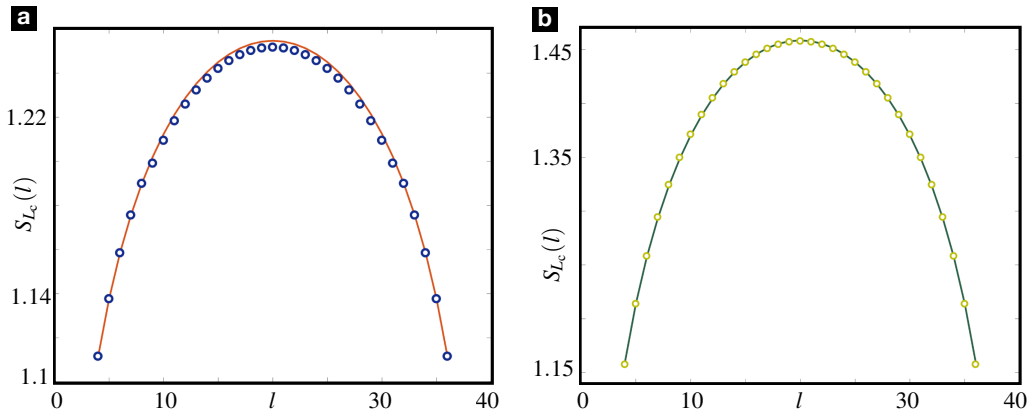

Figure 3.9: Block entanglement entropy of the $\mathbb{Z}_3$ topological Schwinger model: (a) Scaling of the entanglement entropy of a subsystem of size l on the critical point $\Delta_c^{O^-} = -0.162$ and $ga = 0.6$. Through a logarithmic fit (3.36), it is possible to extract the central charge $c = 0.506$. (b) Same as (a), but for $g = \Delta = 0$.

to extract the central charge through a logarithmic fit. We obtain the value $c = 0.506$, in agreement with the central charge of 2D Ising universality class $c = \frac{1}{2}$. Interestingly, by switching off the gauge coupling $g = 0$, we obtain the entanglement entropy of Fig. 3.9**(b)** $\Delta_c^{O^-} = 0$, which yields $c = 1.059$ through the logarithmic fit. This result is in agreement with the expectation for the critical point of the non-interacting SSH model, which can be described by the CFT of a massless Dirac fermion with $c = 1$. Accordingly, the $c = 1$ CFT of the non-interacting SSH model splits into a couple of CFTs with $c = \frac{1}{2}$, each of which controls the criticality of the SPT-C and C-FC quantum phase transitions.

Putting together all these numerical results, we obtain the phase diagram of the $\mathbb{Z}_3$ topological Schwinger model shown in Fig. 3.10**(a)**, which is in qualitative agreement with the analytic predictions for topological QED_2 described in Sec. 3.2, and encapsulated in the phase diagram of Fig. 3.3. Such an agreement is quite remarkable given the fact that $\mathbb{Z}_3$ is still far from the $U(1)$ gauge group used to derive our predictions of topological QED_2. However, there are other situations where such small discrete Abelian gauge groups have turned out to be relevant even for non-Abelian Yang-Mills gauge theories [127]. In the following section, we will show that the resemblance with the $U(1)$ predictions is not only qualitative, but also quantitative as the large-N limit is considered.

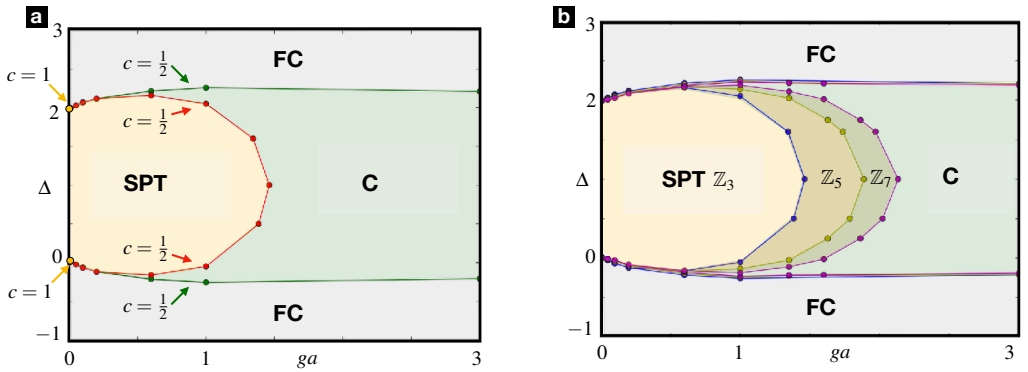

Figure 3.10: Numerical phase diagram for $\mathbb{Z}_N$ topological Schwinger models: (a) Phase diagram of the $\mathbb{Z}_3$ topological Schwinger model, including the symmetry-protected topological (SPT) phase, the confined (C) phase, and the fermion condensate (FC). We also depict the $c = 1$ central charge of the CFT for the non-interacting critical point (orange circle), and its splitting into two $c = \frac{1}{2}$ central charges of the CFTs describing the long-wavelength behaviour in the SPT-C and C-FC quantum phase transitions. (b) Phase diagrams of different $\mathbb{Z}_N$ models: the extension of the SPT phase grows as N is increased.

3.3.3 Large-N phase diagram and topological QED$_2$

In order to access properly the large-N limit of the $\mathbb{Z}_N$ topological Schwinger model (3.26), we use the DMRG algorithm to analyze the $\mathbb{Z}_5$ and $\mathbb{Z}_7$ topological Schwinger models. We observe analogous phase transitions that lie in the same universality class as the ones described for the $\mathbb{Z}_3$ case, albeit taking place at different critical points. Repeating the same procedure carried out for the $\mathbb{Z}_3$ case, we determine the critical points of the $\mathbb{Z}_5$ model and the $\mathbb{Z}_7$ model, resulting in the phase diagrams of Fig. 3.10**(b)**. Here, one can observe that the extension of the SPT phase grows with N while, simultaneously, the spacing between the critical lines becomes smaller.

We can quantify this effect by studying the scaling with N of the critical points g_c fixing $\Delta = 1$. By fitting the critical points with an exponential function $g_c(N)a = Ae^{-B/N} + C$, as shown in Fig. 3.11, we obtain the fitting parameters $A \approx 2.323$, $B \approx 3.177$, $C \approx 0.656$. In this way, we can extract a finite critical value in the $N \to \infty$ limit $g_c(\infty)a = A + C \approx 2.979$, which shows that the SPT phase survives to considerably strong gauge inetractions. Similarly, we can fit the critical points $\Delta_c^{O^-}$ fixing $ga = 0.2$ as a function of N, considering the lower of the two symmetrical critical lines. In this case, we obtain the extrapolation $\Delta_c(\infty) \approx -0.033$. In light of this result, we can conclude that the SPT phase has a finite region of stability in the presence of gauge couplings $g > 0$, which is in accordance to the analytical results

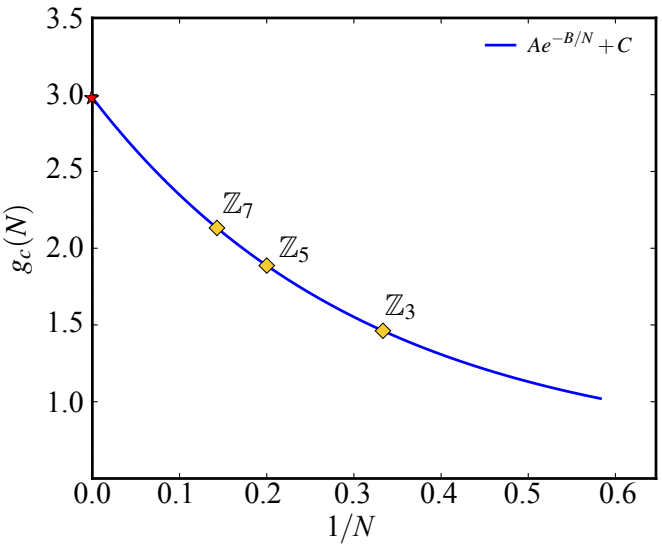

Figure 3.11: Critical points $g_c(N)$ separating the SPT from the confined phases for different values of N: the solid line represents the function $Ae^{(-B/N)}+C$ that fits the points and gives a finite value of $g_c(\infty)a \approx 2.979$ (marked with a red star) in the limit $N \to \infty$ indicating the stability of the SPT phase.

obtain for the $U(1)$ topological Schwinger model. In this sense, our numerical results manifest the expectation that the $\mathbb{Z}_N$ theory yields the $U(1)$ LGT in the limit $N \to \infty$, in which the electric field can assume any continuous value ($\mathbb{Z}_n \to U(1)$).

In order to take one step further in this comparison, and provide a quantitative benchmark of the analytic $U(1)$ results of the previous section, we now analyze the slope of the two critical lines (SPT-C and FC-C) for small g. This will allow us to test the predictions for $\Delta_{c,1}(g)$ and $\Delta_{c,2}(g)$ of Sec. 3.2.4 based on bosonization (see Eqs. (3.23) and (3.24)). For each $\mathbb{Z}_N$ model, we have calculated the critical points Δ_c^{Σ} and $\Delta_c^{O^-}$ for $ga = 0.01, 0.05, 0.10, 0.20$, and performed a linear fit to extract the different slopes $m(N)$. We obtain the values in Table 3.2, which can be fitted to a function of N with an exponential behavior of the form $m(N) = \zeta e^{-(\tau/N)} + \kappa$. This allows us to obtain an extrapolation of the slopes of the two critical lines (SPT-C and FC-C) in the limit $N \to \infty$

$$\begin{aligned} m_1(\infty) &= \zeta_1 + \kappa_1 = -0.1625 \\ m_2(\infty) &= \zeta_2 + \kappa_2 = -0.3034. \end{aligned} \tag{3.37}$$

These values are in remarkable agreement with the expected ones derived in Sec. 3.2.4 for the $U(1)$ limit (respectively $-e^{-\gamma}/(2\sqrt{\pi}) \approx -0.1584$ and $-1/3$).

	Z_3	Z_5	Z_7
Δ_c^{Σ}	-0.67475248	-0.54405941	-0.48118812
Δ_c^{O-}	-0.66831683	-0.54158416	-0.46237624

Table 3.2: Different slopes for small g of the two critical lines.

This numerical results thus point to the general validity of the proposed topological QED_2 as the continuum model describing the role of SPT phases in lattice gauge theories.

3.4 Conclusions

In this Chapter, we have explored the interplay of global and local symmetries, topology, and many-body effects in symmetry-protected topological phases of matter that arise naturally in lattice gauge theories. In particular, we have introduced an alternative discretization of the massive Schwinger model that can host a correlated SPT ground-state, where the many-body effects arise due to the interactions mediated by the gauge bosons. Using bosonization, we have shown that the underlying topology of the SPT phase can modify the vacuum θ angle, and thus lead to a richer phase diagram in comparison to the standard Schwinger model. These bosonization predictions have been carefully benchmarked by numerical DMRG, which has allowed us to calculate relevant fingerprints of the correlated SPT phase, such as the entanglement spectrum and many-body edge states. Moreover, we have presented a thorough finite-size scaling analysis of the electric-field order parameter and a topological correlator, which yield concrete predictions of the phase diagram that are in agreement with the bosonization results.

Our work opens an interesting route to study topological phases of matter in gauge theories, either using some of the theoretical tools hereby developed, or via cold-atom experiments. Hopefully, these results will stimulate further work in this subject, exploring interesting questions such as the interplay of topological features with non-perturbative effects in LGTs, such as screening, confinement, and string-breaking.

Appendices

Chapter A

Additional information on the phase transition

We give here additional details on the phase transition, as well as numerical figures, for different $\mathbb{Z}_n$-models.
Let us start with $n = 3$. For $t = 0$, the transition is sharp for every system size, as can be seen in Fig. A.1. As explained at the end of Sec. 1.4.2, the system undergoes here a first order phase transition between the Dirac sea and the mesonic state shown in Figs. 1.5(a) and 1.5(b). Our numerical findings for $m_c(t)$ as a function of t are summarized in Table A.1.
Our numerical findings for $m_c(t)$ for the $\mathbb{Z}_5$ and $\mathbb{Z}_7$-models are given in Tables A.2 and A.3, respectively. Those for the $\mathbb{Z}_2$, $\mathbb{Z}_4$, $\mathbb{Z}_6$ and $\mathbb{Z}_8$-models are reported in Tables A.4, A.5, A.6, and A.7, respectively.
All the values given in the Tables are plotted in Fig. 1.15, to yield the fit in Eq. (1.44).

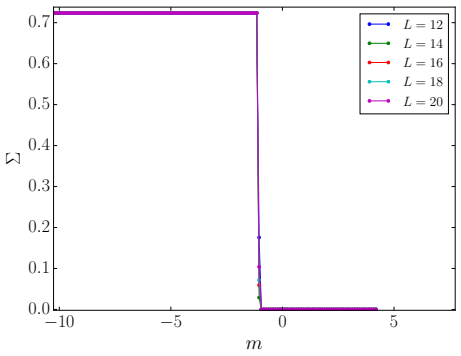

Figure A.1: $\mathbb{Z}_3$-model. Σ as function of m at $t = 0$, for different system size L.

t	0.000	0.523	1.047	1.571	2.094	6.283	10.472	20.944	41.888	62.832	104.720
m_c	-1.047	-1.340	-1.571	-1.770	-1.948	-2.927	-3.596	-4.767	-6.329	-7.449	-9.115

Table A.1: $\mathbb{Z}_3$-model. Critical values $m_c(t)$ for different values of t. The error is always 0.025.

t	0.000	1.257	2.513	3.769	5.026	15.080	25.133	50.265	100.531	150.796
m_c	-0.628	-1.181	-1.483	-1.734	-1.935	-3.171	-3.941	-5.298	-7.077	-8.309

Table A.2: $\mathbb{Z}_5$-model. Critical values $m_c(t)$ for different values of t.The error is always 0.025.

t	0.000	8.078	24.235	40.392	80.784	161.568
m_c	-0.448	-1.971	-3.110	-3.797	-5.299	-6.883

Table A.3: $\mathbb{Z}_7$-model. Critical values $m_c(t)$ for different values of t. The error is always 0.025.

t	0.000	0.196	0.392	0.589	0.785	2.356	3.927	7.854	15.708	23.562	39.269
m_c	0.000	0.012	0.013	0.014	0.016	0.035	0.062	0.122	0.239	0.361	0.601

Table A.4: $\mathbb{Z}_2$-model. Critical values $m_c(t)$ for different values of t. The error is always 0.025.

t	0.000	0.884	1.767	2.651	3.534	10.603	17.671	35.342	70.685	106.029
m_c	0.000	0.491	0.795	1.039	1.233	2.403	3.244	4.887	7.439	9.581

Table A.5: $\mathbb{Z}_4$-model. Critical values $m_c(t)$ for different values of t. The error is always 0.025..

t	0.000	1.636	4.909	6.545	19.635	32.725	65.449	130.889
m_c	0.000	0.635	1.355	1.577	2.925	3.959	6.093	9.614

Table A.6: $\mathbb{Z}_6$-model. Critical values $m_c(t)$ for different values of t. The error is always 0.025.

t	0.000	9.621	28.863	48.106	96.211
m_c	0.000	1.809	3.309	4.541	7.062

Table A.7: $\mathbb{Z}_8$-model. Critical values $m_c(t)$ for different values of t. The error is always 0.025.

Chapter B

Finite size scaling and large-n limit

The question about how our lattice $\mathbb{Z}_n$ model converges to the $U(1)$ continuum model was theoretically studied in [29] and then thoroughly checked via numerical simulations in Sec. 1.6. There we noticed that indeed one recovers the Schwinger model for QED in $1+1$ dimensions, obtaining a good approximation already for lattice sizes of order of about 50 sites and for $n = 3$. In this appendix we give some additional details on the numerics and on the finite-size and large-n analysis we have performed for the time-dependent simulations.

Numerical precision. All simulations for the real-time dynamics have been performed with a time-dependent DMRG (t-DMRG) code, which is a well-established method for studying dynamical properties of quantum systems in one dimension [99]. The time-evolution is based on a Runge-Kutta 4th order scheme, with a time step of $\delta = 0.01$. We implemented the initial state for the time-evolution by calculating the ground-state of two different Hamiltonians: i) for the pair production analysis, we obtained the vacuum state (see Fig. 1.4) by using the Hamiltonian (2.1), setting $t = 0$ and large values of m and g, i.e. $m = 5$, $g = 3$; ii) for the string breaking mechanism, we added to the aforementioned Hamiltonian localized electric field terms $E_{x,x+1}$ on each link in which we want to create the initial string. In our simulations, we used a variable number of DMRG-states, up to 1200, in order to keep the truncation error below 10^{-6} at each time step.

Spontaneous pair production. To study finite size effects in simulating the spontaneous pair production, we have repeated our simulations for different chain sizes ($N = 16, 20, 24, 28, 32, 36, 40$), in order to extract the infinite size limit of $\rho(t)$. For example, Fig. B.1(a) shows the behaviour of $\rho(t)$ close to

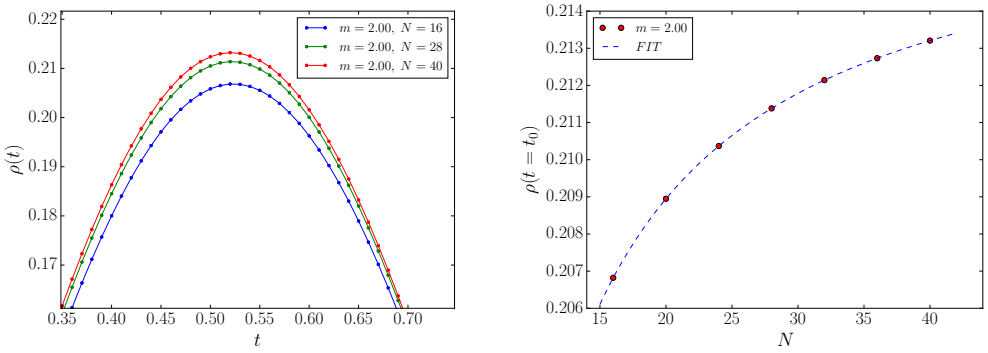

(a)

(b)

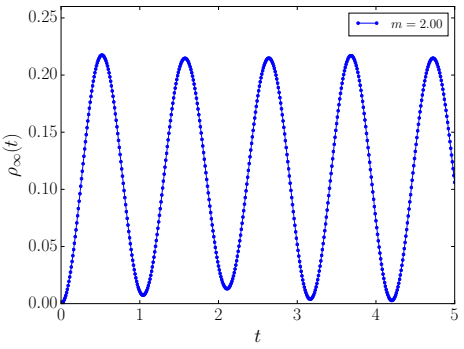

(c)

Figure B.1: $\mathbb{Z}_3$-model. Finite size analysis of the particle density, for $m = 2.0$: (a) behaviour of $\rho(t)$ close to its first maximum; (b) scaling with the chain size N of $\rho(t_0 = 0.52)$; (c) time evolution of $\rho_\infty(t)$.

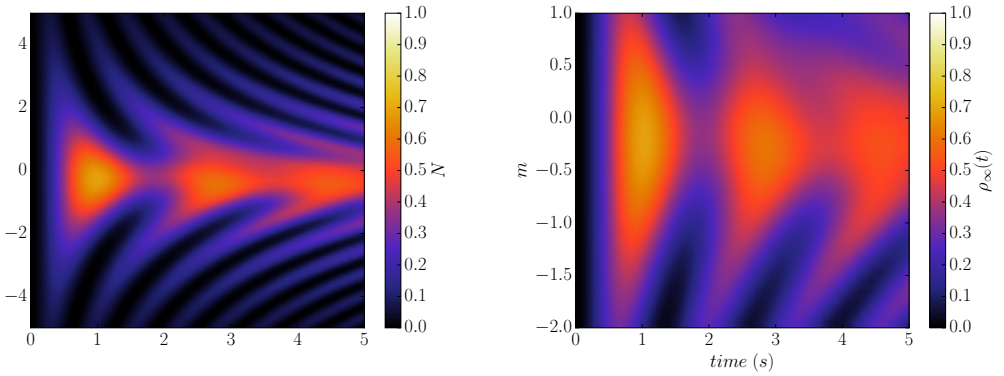

(a) (b)

Figure B.2: Contour plot of $\rho_\infty(t)$ for (a) $\mathbb{Z}_5$-model and $m \in [-5.0, +5.0]$, (b) $\mathbb{Z}_7$-model and $m \in [-2.0, +1.0]$. Notice that in the latter case we have reduced the range of the mass since numerical simulations are computationally cumbersome.

its first maximum, for $m = 2.0$ and different chain sizes. We find that, at all instants of time t_0, we can estrapolate its infinite size limit $\rho_\infty(t_0)$ according to the following fit:

$$\rho(t = t_0) = \rho_\infty(t_0) - \frac{\beta(t_0)}{N}. \tag{B.1}$$

An example, for $m = 2.0$ and $t_0 = 0.52$ is shown in Fig. B.1(b), for which we get $\rho_\infty(t_0) = 0.2175 \pm 0.0001$ and $\beta(t_0) = 0.1703 \pm 0.0001$. The time evolution of $\rho_\infty(t)$ is given in Fig. B.1(c).

Also, we have repeated the same simulations in the case of $\mathbb{Z}_5$ and $\mathbb{Z}_7$. In Fig. B.2(a) and Fig. B.2(b) we show the contour of $\rho_\infty(t)$ in the whole range of the quenched mass $m \in [-5, +5]$, similarly to what we have done in Fig. 2.4 for the $\mathbb{Z}_3$-model. We see a very similar behaviour.

Pair production in an external field. To evaluate finite-size effects in the pair production rate with external field, we have repeated the simulations for $N = 50, 60, 70, 80, 90$ while, to check the large-n limit to see if we can reasonably approximate the $U(1)$ limit, we have performed simulations also for the $\mathbb{Z}_5$ and the $\mathbb{Z}_7$ models. The results are shown and compared with Schwinger formula in Fig. B.3(a) and Fig. B.3(b). Even if we pushed the simulations to the maximum capability of our computers, it is evident that our numerics still suffer from strong finte-size and finite-n corrections. However, the data follow a pattern that is qualitatively in agreement with the predictions of the continuum $U(1)$-model and shows the correct scaling. Thus we can conclude

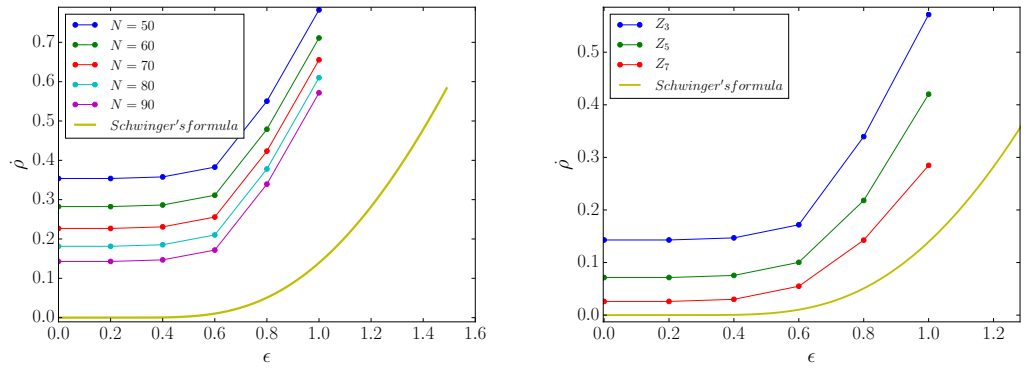

(a) (b)

Figure B.3: (a) Numerical results for $\dot{\rho}$ in the $\mathbb{Z}_3$ model as function of ϵ, for different chain sizes N; the continuous result of Eq. (2.11) is reported for comparison. (b) Numerical results for $\dot{\rho}$ as function of ϵ for different chain sizes $\mathbb{Z}_n$ models (fixed $N = 90$) and comparison with the continuous result of Eq. (2.11).

that indeed we are describing the physics of the Schwinger model.

Acknowledgements

A conclusione di questo ciclo di Dottorato desidero ringraziare calorosamente tutti coloro che mi hanno accompagnato e sostenuto, durante questi anni, con i loro consigli, gli innumerevoli insegnamenti ed il loro affetto.
In primis, ringrazio la mia relatrice, Prof.ssa Elisa Ercolessi, per avermi dato la possibilità di conoscere ed approfondire molteplici tematiche di ricerca, attraverso le innumerevoli discussioni ed il continuo supporto lungo questi anni. In molte occasioni è stata una guida ed un punto di riferimento per me.
Un caloroso ringraziamento al Prof. Fabio Ortolani per i suoi preziosissimi insegnamenti e la sua disponibilità, ed al Prof. Cristian Degli Esposti Boschi per le stimolanti discussioni durante i nostri incontri.
Un ringraziamento particolare al Prof. Marcello Dalmonte per avermi fatto sentire a casa durante il mio periodo presso l'ICTP di Trieste, per l'aiuto fondamentale offertomi, sia dal punto di vista scientifico che personale, e per le opportunità di crescita professionale.
Ringrazio il Prof. Saverio Pascazio, il Prof. Paolo Facchi, il Dr. Francesco Pepe del gruppo teorico dell'Università di Bari per la lunga collaborazione di questi anni: i nostri incontri sono stati fondamentali per i risultati di questa tesi.
Un sincero grazie al Prof. Alejandro Bermudez dell'Università Complutense di Madrid, al Prof. Markus Muller della RWTH Aachen University ed al Prof. Prem Kumar dell'Università di Swansea per la preziosa e fruttuosa collaborazione.
Non posso dimenticare tutti i miei colleghi ed amici, che mi hanno accompagnato durante questo percorso: Davide Vodola, Piero Naldesi, Thomas Botzung, tutto il gruppo di Trieste (Federica Surace, Pierre Fromholz, Adriano Angelone, Giuliano Giudici, Xhek Turkeshi, Thiago Mendes Santos, Eduardo Gonzalez Lazo), con cui ho condiviso discussioni, idee, uffici, serate e momenti indimenticabili.
Un grazie sincero alla mia famiglia per la disponibilità e il supporto immancabile.
Un grazie a tutti gli amici mattinatesi e garganici di sempre, emigrati e non, e a tutte le nuove conoscenze di questi favolosi anni bolognesi.

Giuseppe Magnifico

Bibliography

[1] E. Y. Loh, Jr., J. E. Gubernatis, R. T. Scalettar, S. R. White, D. J. Scalapino, and R. L. Sugar, Phys. Rev. B **41**, 9301 (1990).

[2] R. P. Feynman, International Journal of Theoretical Physics, 21, 6/7, (1982).

[3] I. M. Georgescu, S. Ashhab, and Franco Nori, Rev. Mod. Phys. **86** (2014).

[4] C. Gross1, and I. Bloch, Science **357**, 6355 (2017).

[5] R. Blatt and C. F. Roos, Nat. Phys. **8**, 277 (2012).

[6] A. A. Houck, H. E. Türeci, and Jens Koch, Nature Physics **8**, 292?299 (2012).

[7] M. J. Hartmann, J. Opt. **18**, 104005 (2016).

[8] H. J. Rothe, *Lattice gauge theories* (World Scientific, Singapore, 1992).

[9] I. Montvay and G. Münster, *Quantum Fields on a Lattice* (Cambridge University Press, Cambridge, 1994).

[10] K. Wilson, Phys. Rev. D **10**, 2445 (1974).

[11] J. B. Kogut and L. Susskind, Phys. Rev. D **11**, 395 (1975).

[12] S. Aoki et al., arXiv:1310.8555 (2013).

[13] L. Susskind, Phys. Rev. D **16**, 3031 (1977).

[14] I. Bloch, J. Dalibard, and W. Zwerger, Rev. Mod. Phys. **80**, 885 (2008).

[15] M. Lewenstein, A. Sanpera and V. Ahufinger, *Ultracold Atoms in Optical Lattices: Simulating Quantum Many-Body Systems* (Oxford University Press, New York, 2012).

[16] J. I. Cirac and P. Zoller, Nat. Phys. **8**, 264 (2012).

[17] I. Bloch, J. Dalibard, and S. Nascimbène, Nat. Phys **8**, 267 (2012).

[18] E. Kapit and E. Mueller, Phys. Rev. A **83**, 033625 (2011).

[19] E. Zohar, J. I. Cirac, and B. Reznik, Phys. Rev. Lett. **109**, 125302 (2012).

[20] L. Tagliacozzo, A. Celi, P. Orland, and M. Lewenstein, Nat. Commun. **4**, 2615 (2013).

[21] K. Kasamatsu, I. Ichinose, and T. Matsui, Phys. Rev. Lett. **111**, 115303 (2013).

[22] D. Banerjee, M. Bögli, M. Dalmonte, E. Rico, P. Stebler, U. J. Wiese, and P. Zoller, Phys. Rev. Lett. **110**, 125303 (2013).

[23] L. Tagliacozzo, A. Celi, A. Zamora, and M. Lewenstein, Ann. Phys. (Amsterdam) **330**, 160 (2013).

[24] E. Zohar, J. I. Cirac, and B. Reznik, Phys. Rev. A **88**, 023617 (2013).

[25] K. Stannigel, P. Hauke, D. Marcos, M. Hafezi, S. Diehl, M. Dalmonte, and P. Zoller, Phys. Rev. Lett. **112**, 120406 (2014).

[26] E. Zohar, J. I. Cirac, and B. Reznik, Rep. Prog. Phys. **79**, 014401 (2016).

[27] P. Hauke, D. Marcos, M. Dalmonte, and P. Zoller, Phys. Rev. X **3**, 041018 (2013).

[28] S. Kühn, J. I. Cirac, and M.C. Bañuls, Phys. Rev. A **90**, 042305 (2014).

[29] S. Notarnicola, E. Ercolessi, P. Facchi, G. Marmo, S. Pascazio and F. V. Pepe, J. Phys. A: Math. Theor. **48**, 30FT01 (2015).

[30] V. Kasper, F. Hebenstreit, F. Jendrzejewski, M K Oberthaler, and J. Berges, New J. Phys. **19** (2017), 023030.

[31] A. Celi, P. Massignan, J. Ruseckas, N. Goldman, I. B. Spielman, G. Juzeliūnas, and M. Lewenstein, Phys. Rev. Lett. **112**, 043001 (2014).

[32] G. Pagano, M. Mancini, G. Cappellini, P. Lombardi, F. Schäfer, H. Hu, X.-J. Liu, J. Catani, C. Sias, M. Inguscio, and L. Fallani, Nat. Phys. **10**, 198 (2014).

[33] F. Scazza, C. Hofrichter, M. Höfer, P. C. De Groot, I. Bloch, and S. Fölling, Nat. Phys **10**, 779 (2014).

[34] M. Mancini, G. Pagano, G. Cappellini, L. Livi, M. Rider, J. Catani, C. Sias, P. Zoller, M. Inguscio, M. Dalmonte, L. Fallani, Science **349**, 1510 (2015).

[35] L. F. Livi, G. Cappellini, M. Diem, L. Franchi, C. Clivati, M. Frittelli, F. Levi, D. Calonico, J. Catani, M. Inguscio, L. Fallani, Phys. Rev. Lett. **117**, 220401 (2016).

[36] E.A. Martinez, C.A. Muschik, P. Schindler, D. Nigg, A. Erhard, M. Heyl, P. Hauke, M. Dalmonte, T. Monz, P. Zoller, and R. Blatt, Nature **534**, 516 (2016).

[37] U. Schollwöck, Rev. Mod. Phys. **77**, 259 (2005).

[38] R. Orus, Annals of Physics **349**, 117 (2014).

[39] D. Banerjee, M. Dalmonte, M. Müller, E. Rico, P. Stebler, U. J. Wiese, and P. Zoller, Phys. Rev. Lett. **109**, 175302 (2012).

[40] M.C. Bañuls, K. Cichy, K. Jansen, J.I. Cirac, JHEP **11**, 158 (2013).

[41] E. Rico, T. Pichler, M. Dalmonte, P. Zoller, and S. Montangero, Phys. Rev. Lett. **112**, 201601 (2014).

[42] T. Pichler, M. Dalmonte, E. Rico, P. Zoller, and S. Montangero, Phys. Rev. X **6**, 011023 (2016).

[43] B. Buyens, J. Haegeman, F. Hebenstreit, F. Verstraete and K. Van Acoleyen, Phys. Rev. D **96**, 114501 (2017).

[44] B. Buyens, J. Haegeman, H. Verschelde, F. Verstraete, K. Van Acoleyen, Phys. Rev. X **6**, 041040 (2016).

[45] B. Buyens, S. Montangero, J. Haegeman, F. Verstraete and K. Van Acoleyen, Phys. Rev. D **95**, 094509 (2017).

[46] F. A. Wilczek, Rev. Mod. Phys. **77**, 857 (2005).

[47] R. Nandkishore and D. A. Huse, Annu. Rev. Condens. Matter Phys. **6**, 15 (2015).

[48] L. Landau, Zh. Eksp. Theor. Fiz. **7**, 19 (1937), Phys. Z. Sowjetunion **11**, 26 (1937).

[49] P. W. Anderson, Science **177**, 393 (1972).

[50] F. D. M. Haldane, Phys. Rev. Lett. **61,** 2015 (1988)

[51] C. L. Kane and E. J. Mele, Phys. Rev. Lett. **95,** 146802 (2005).

[52] K. V. Klitzing, G. Dorda, and M. Pepper, Phys. Rev. Lett. **45,** 494 (1980).

[53] D. J. Thouless, M. Kohmoto, M. P. Nightingale, and M. den Nijs, Phys. Rev. Lett. **49,** 405 (1982).

[54] M. Z. Hasan and C. L. Kane, Rev. Mod. Phys. **82,** 3045 (2010).

[55] X.-L. Qi and S.-C. Zhang, Rev. Mod. Phys. **83,** 1057 (2011).

[56] A. Bansil A, H. Lin, and T. Das, Rev. Mod. Phys. **88,** 021004 (2016).

[57] D. C. Tsui, H. L. Stormer, and A. C. Gossard, Phys. Rev. Lett. **48,** 1559 (1982).

[58] R. B. Laughlin, Phys. Rev. Lett. **50,** 1395 (1983).

[59] M. Hohenadler, and F. F. Assaad, J. Phys.: Condens. Matter **25,** 143201 (2013); S.A. Parameswaran, R. Roy, and S.L. Sondhi, Compt. Rend. Phys. **14,** 816 (2013).

[60] J. Kogut and L. Susskind, Phys. Rev. D **11,** 3594 (1975).

[61] A. O. Gogolin, A. A. Nersesyan, A. M. Tsvelik, *Bosonization and Strongly Correlated Systems*, Cambridge University Press (2004).

[62] D. Horn, Phys. Lett. **100B**, 149 (1981).

[63] P. Orland and D. Rohrlich, Nucl. Phys. **B338**, 647 (1990).

[64] S. Chandrasekharan and U. J. Wiese, Nucl. Phys. **B492**, 455 (1997).

[65] U. J. Wiese, Ann. Phys. (Berlin) **525**, 777 (2013).

[66] K. Melnikov and M. Weinstein, Phys. Rev. D **62**, 094504 (2000).

[67] H. Weyl *The theory of groups and quantum mechanics* (Courier Dover Publications, 1950).

[68] S. Coleman, Ann. Phys. **101**, 239 (1976).

[69] N. S. Manton, Ann. Phys. **159**, 220 (1985).

[70] C. Kiefer and A. Wipf, Ann. Phys. **236**, 241 (1994).

[71] C. D. E. Boschi and F. Ortolani, Eur. Phys. J. B **41**, 503 (2004).

[72] J. Cardy, *Scaling and Renormalization in Statistical Physics* (Cambridge University Press, Cambridge, England, 1996).

[73] P. Calabrese and J. Cardy, J. Stat. Mech. **0406**, 002 (2004).

[74] M. Henkel, *Conformal Invariance and Critical Phenomena* (Springer, New York, 1999).

[75] Y. Shimizu and Y. Kuramashi, Phys. Rev. D **90**, 014508 (2014); Y. Shimizu and Y. Kuramashi, Phys. Rev. D **90**, 074503 (2014).

[76] T. M. R. Byrnes, P. Sriganesh, R. J. Bursill, and C. J. Hamer, Phys. Rev. D **66**, 013002 (2002); Nucl. Physics B Proceedings Supplements **109**, 202 (2002).

[77] I. Sachs, A. Wipf, Helv. Phys. Acta **65**, 652 (1992).

[78] C. J. Hamer, J. Kogut, D. P. Crewther and M. M. Mazzolini, Nucl. Phys. B **208**, 413 (1982).

[79] L. Amico, A. Osterloh, and F. Cataliotti, Phys. Rev. Lett. **95**, 063201 (2005).

[80] F. M. Surace, P. P. Mazza, G. Giudici, A. Lerose, A. Gambassi, and Marcello Dalmonte, arXiv:1902.09551.

[81] M. Dalmonte and S. Montangero, Contemporary Physics 57 388 (2016).

[82] E. Zohar and J.I. Cirac, Phys. Rev. D **99**, 114511 (2019).

[83] B. M. McCoy and T. T. Wu, Phys. Rev. D **18**, 1259 (1978).

[84] M. Kormos, M. Collura, G. Takacs, and P. Calabrese, Nature Physics **13** 246-249, (2017).

[85] P. Calabrese and J. L. Cardy, J. Stat. Mech. **0504** P04010 (2005).

[86] A. Laeuchli and C. Kollath, J. Stat. Mech. P05018 (2008); H. Kim and D. A. Huse, Phys. Rev. Lett. **111**, 127205 (2013); S. R. Manmana, S. Wessel, R. M. Noack, and A. Muramatsu, Phys. Rev. B **79**, 155104 (2009); P. Barmettler, D. Poletti, M. Cheneau, and C. Kollath, Phys. Rev. A **85**, 053625 (2012); G. Carleo, F. Becca, L. Sanchez-Palencia, S. Sorella, and M. Fabrizio, Phys. Rev. A **89**, 031602 (2014); L. Bonnes, F. H. L. Essler, and A. M. Lauchli, Phys. Rev. Lett. **113**, 187203 (2014); R. Geiger, T. Langen, I. E. Mazets, and J. Schmiedmayer, New J. Phys **16**, 053034 (2014).

[87] E. H. Lieb and D. W. Robinson, Commun. Math. Phys. (1972) 28: 251.

[88] Compare for example our Fig. 2.5(c) with Fig. 6 of Ref. [84].

[89] H. Bernien, S. Schwartz, A. Keesling, H. Levine, A. Omran, H. Pichler, S. Choi, A. S. Zibrov, M. Endres, M. Greiner, V. Vuletić, M. D. Lukin, Nature **551**, 579-584 (2017).

[90] C. J. Turner, A. A. Michailidis, D. A. Abanin, M. Serbyn, and Z. Papić, Nature Physics, **14**, 745-749 (2018); Phys. Rev. B **98**, 155134 (2018).

[91] V. Khemani, C. R. Laumann, and A. Chandran, Phys. Rev. B **99**, 161101 (2019).

[92] P. Calabrese and J. Cardy, Phys. Rev. Lett. **96**, 136801 (2006); J. Stat. Mech. **0706** (2007) P06008.

[93] J. Schwinger, Phys. Rev. **82**, 664 (1951).

[94] F. Hebenstreit, R. Alkofer, and H. Gies, Phys. Rev. D **82**, 105026 (2010).

[95] F. Hebenstreit, J. Berges, and D. Gelfand, Phys. Rev. D **87**, 105006 (2013).

[96] F. Liu, R. Lundgren, P. Titum, G. Pagano, J. Zhang, C. Monroe, and A. V. Gorshkov, Phys. Rev. Lett. **122**, 150601 (2019).

[97] O. Pomponio, L. Pristyák, and G. Takács, J. Stat. Mech. (2019) 013104.

[98] S. Notarnicola, M. Collura, and S. Montangero, arXiv:1907.12579 (2019).

[99] U. Schollwöck and S. R. White, AIP Conf. Proc. **816**, 155 (2006).

[100] S. Coleman, R. Jackiw, and L. Susskind, Ann. Phys. **93,** 267 (1975).

[101] J. Schwinger, Phys. Rev. **128,** 2425 (1962).

[102] J. Lowenstein and A. Swieca, Ann. Phys. **68,** 172 (1971).

[103] H. J. Rothe, K. D. Rothe, and J. A. Swieca, Phys. Rev. D **19,** 3020 (1979).

[104] J. Schwinger, Phys. Rev. Lett. **3,** 296 (1959).

[105] P. Sriganesh, C. J. Hamer, and R. J. Bursill, Phys. Rev. D **62,** 034508 (2000).

[106] A. J. Schiller and J. Ranft, Nuc. Phys. B, 225, 204 (1983).

[107] W. P. Su, J. R. Schrieffer, and A. J. Heeger, Phys. Rev. Lett. **42**, 1698 (1979).

[108] A. J. Heeger, S. Kivelson, J. R. Schrieffer, andW. P. Su, Rev. Mod. Phys. **60,** 781 (1988).

[109] D. Xiao, M.-C. Chang, and Q. Niu, Rev. Mod. Phys. **82,** 1959 (2010).

[110] J. Zak, Phys. Rev. Lett. **62,** 2747 (1989).

[111] A. P. Schnyder, S. Ryu, A. Furusaki, and A. W. W. Ludwig, Phys. Rev. B **78**, 95125 (2008); A. Kitaev, AIP Conference Proceedings 1134 22 (2009).

[112] I. Affleck, Les Houches Proceedings, in *Fields, strings and critical phenomena*, eds. E Brezin and J. Zinn-Justin, (North-Holland, Amsterdam, 1988).

[113] M. Fabrizio and A. O. Gogolin, Phys. Rev. B **51,** 17827 (1995).

[114] R. Jackiw and C. Rebbi, Phys. Rev. D **13,** 3398 (1976).

[115] J. K. Asboth, L. Oroszlany, and A. Palyi, *A Short Course on Topological Insulators: Band-structure topology and edge states in one and two dimensions* (Springer, 2016).

[116] S. Coleman, R. Jackiw, and L. Susskind, Ann. Phys. **93,** 267 (1975).

[117] T. Byrnes, *Density matrix renormalization group: A new approach to lattice gauge theory*, (PhD thesis, University of New South Wales).

[118] Jeffrey C. Y. Teo and C. L. Kane, Phys. Rev. B **82,** 115120 (2010).

[119] X.-L. Qi, T. L. Hughes, and S.-C. Zhang, Phys. Rev. B **78,** 195424 (2008); X.-L. Qi, R. Li, J. Zang, and S.-C. Zhang, Science **323,** 1184 (2009).

[120] M. Vojta, Phil. Mag. **86,** 1807 (2006).

[121] I. Ichinose and H. Mukaida, Int. J. Mod. Phys. A **9,** 1043 (1994).

[122] W. Yu, Y. Li, P. Sacramento, H. Lin, Phys. Rev. B **94,** 245123 (2016).

[123] H. Li and F. D. M. Haldane, Phys. Rev. Lett. **101,** 010504 (2015).

[124] F. Pollmann, A. M. Turner, E. Berg, M. Oshikawa, Phys. Rev. B **81,** 064439 (2009).

[125] L. Fidkowski, Phys. Rev. Lett. **104,** 130502 (2010).

[126] G. Vidal, J. Latorre, E. Rico, and A. Kitaev, Phys. Rev. Lett. **90,** 227902 (2003);

[127] G. 't Hooft, Nucl. Phys. B **138,** 1 (1978).